# THE DEFECT EVOLUTION IN SHOCK LOADED TANTALUM SINGLE CRYSTALS


**BO PANG**

A thesis submitted to The University of Birmingham

for the degree of

**Doctor of Philosophy**

School of Metallurgy and Materials

College of Engineering and Physical Science

The University of Birmingham

September 2015

# PREFACE

The work described in this thesis was carried out by the author in the School of Metallurgy and Materials, the University of Birmingham from Sep. 2011 to Sep. 2015, under the supervision of Dr. Yu-Lung Chiu and Prof. Ian Jones.

The present work is original and no part of this work has been submitted for a degree at any other university. Wherever others' work has been drawn or cited, it is acknowledged in the text and a list of references is included at the end of this thesis.

Part of the present work has been published as follows:

B. Pang, I. P. Jones, Y. L. Chiu, J. C. F. Millett, G. Whiteman and N. Bourne. Orientation Dependence of Shock Induced Dislocations in Tantalum Single Crystals. *Journal of Physics: Conference Series,* 522(1): 012129-012133, 2014.

B. Pang, I. P. Jones, J. C. F. Millett, G. Whiteman, N. Bourne and Y. L. Chiu. Radial Stress Release Wave Induced Twinning in a Tantalum Single Crystal. *Metallurgical and Materials Transactions A.* 46(10): 4522-4526, 2015.

# Acknowledgements

Firstly I am grateful to my supervisors, Dr. Yu-Lung Chiu and Prof. Ian Jones for their guidance and support through out the PhD. Moreover I would like to thank Prof. Michael Loretto, Dr Ming Chu, Dr Rengen Ding and Dr Winson Kuo for their advice on EM and encouragement. I would like to thank Paul Stanley and Theresa Morris for their assistance with the microscopes, without them this would not have been possible.

Next I would like to thank my fellow students in the EM group, they have made this a far more enjoyable few years. Especially Daniel Higgins for many fruitful discussions and listening to me ramble. As well Gareth Douglas for being the only one bored enough to discuss Bloch waves and Minshi Wang for suffering my company for 4 years! Thiago Soares Pereira and Tina Su for sharing good times and Jing Wu obviously! Yu Lu, Rayan Ameen, Xin Yu Lu, Zhaoran Liu, Xinxin Zhao, Ruilin Zeng, Jinsen Tian, Subash Rai and anyone else who I have forgotten. Thank you as well to my flatmate Suyang Yu for looking after me when I was too busy writing to eat!

Lastly and most importantly thank you to my parents, their constant love and patience have made my life so easy in the past 25 years.

# Abstract

The defect structure of single crystal tantalum with orientation 001, 011 and 111 after a 6 GPa shock loading with lateral and back release waves were characterised using scanning electron microscopy (SEM) and transmission electron microscopy. The SEM images were filtered using ImageJ script to determine the type and fraction of deformation twins. A methodology of imaging dislocations in the tantalum single crystals using electron channelling contrast was made with the assistance of the dislocation contrast profile simulation based on the dynamical theory of electron diffraction. The dislocation density distribution was measured using electron channelling contrast imaging (ECCI) technique.

The nucleation and growth of the deformation twins are discussed with the aid of finite element simulation of the wave propagation in the material. The defect evolution and response of the single crystals are found to be highly dependent on the loading orientation of the shock wave. The effects of the lateral release wave and back release waves on the deformation mechanisms are also discussed.

# Contents

# List of figures

# List of tables

# Chapter 1

# Introduction

In order to improve the property and simulate the behaviour of a material in a high rate deformation environment, there is a need to understand the deformation mechanisms of the material under high rate shock loading-unloading. Especially for tantalum, which is not only an important model material as a high stacking fault energy body centred cubic metal, but also has a wide range of applications related to high strain rate deformation. The application of tantalum requires a full understanding of its properties under high strain rate/shock loaded deformation, including compression, release and oblique waves. The deformation behaviour of tantalum under one dimensional shock loading has been extensively studied over the past few decades. The tested materials were generally shock loaded by a plane wave and unloaded in the same direction with a planar release wave. The experimental data is usually taken from the shock front to investigate the material behaviour at high pressure, with less attention paid to the effect of the release waves. However,

there are several studies in recent years showing that release waves are also an important factor in examining the material behaviour in dynamic loading condition; in some cases the plastic strain on release is even larger than for the shock wave [1]. In a real shock loading condition, like foreign object damage on aircraft, the loading cannot always be one dimensional. Therefore, we should consider the release waves and their interaction as an important contributor in studying the dynamic behaviour of tantalum.

In this study, tantalum single crystals were subjected to a $6\,GPa$ plate impact experiment using a single stage gas gun. The specimens were fixed into the chamber using epoxy, letting the release waves enter the specimen freely. By investigating the post shock microstructure using electron microscopy, a better understanding of the properties of tantalum under complex loading conditions is achieved.

# Chapter 2

# Literature review

## 2.1 Tantalum

### 2.1.1 Tantalum applications

Tantalum (Ta) is a common refractory metal with a body-centred cubic crystalline structure and atomic number 73 [2]. As a heavy metal with high strength and excellent ductility, tantalum is an ideal material for use in shaped charges and explosively forged projectiles (EFPs)[2] [3]. This application requires a good knowledge of tantalum deformation behaviour at high strain rate/shock loading, especially the hardening mechanisms and defect generation in high pressure shock compression and release.

### 2.1.2 Plastic deformation of tantalum

The quasi-static mechanical properties of tantalum are well-documented. The yield stress of Ta is very sensitive to temperature, lattice impurities and strain rate. The initial stress for plastic flow of Ta increases significantly at low temperature and high strain rate [4]. Slip of Ta is in crystal directions $\langle 111 \rangle$. The dislocations prefer to slip on the $\{110\}$ planes, but they often slip on any plane with the highest resolved shear stress, and deviate to the nearest $\{110\}$ plane [5]. Cross slip onto secondary $\{112\}$ planes produces wavy slip lines [5]. This cross-slip controlled phenomenon is less significant at low temperature, where Ta slips on well defined $\{110\}$ crystalline planes [6] [7] [4]. Three stage hardening behaviour has been found in Ta under quasi-static deformation [4]. A summary of the dislocation microstructure evaluation under quasi-static deformation is shown in Figure 2.1. In Stage I, dislocations are tangled together on the slip planes and surrounded by dislocation free areas. The dislocations are predominantly highly jogged screws. This is because the edge segments of the dislocations are much more mobile than the screw parts [8]. In Stage II the dislocation tangles increase in density and form walls on the slip plane. The walls become more tangled and turn into elongated dislocation cells in stage III. The cell sizes reduce with a rise in strain.

At low temperature and high strain rate, the hardening of tantalum is dominated by high initial flow stress [4]. In the strain rate range $10^{-5} - 10^{0} s^{-}1$, the effect of increasing strain rate on the stress-strain curve is entirely equivalent to decreasing the temperature [4]. Twinning is found in tantalum deformed at low temperature, where a high stress is required for dislocation slip. The stress for twinning can be

strongly altered by the stress applied to the twin plane normal, and is dependent on the orientation of the shear stress due to the asymmetry of the {112} twinning plane[7].

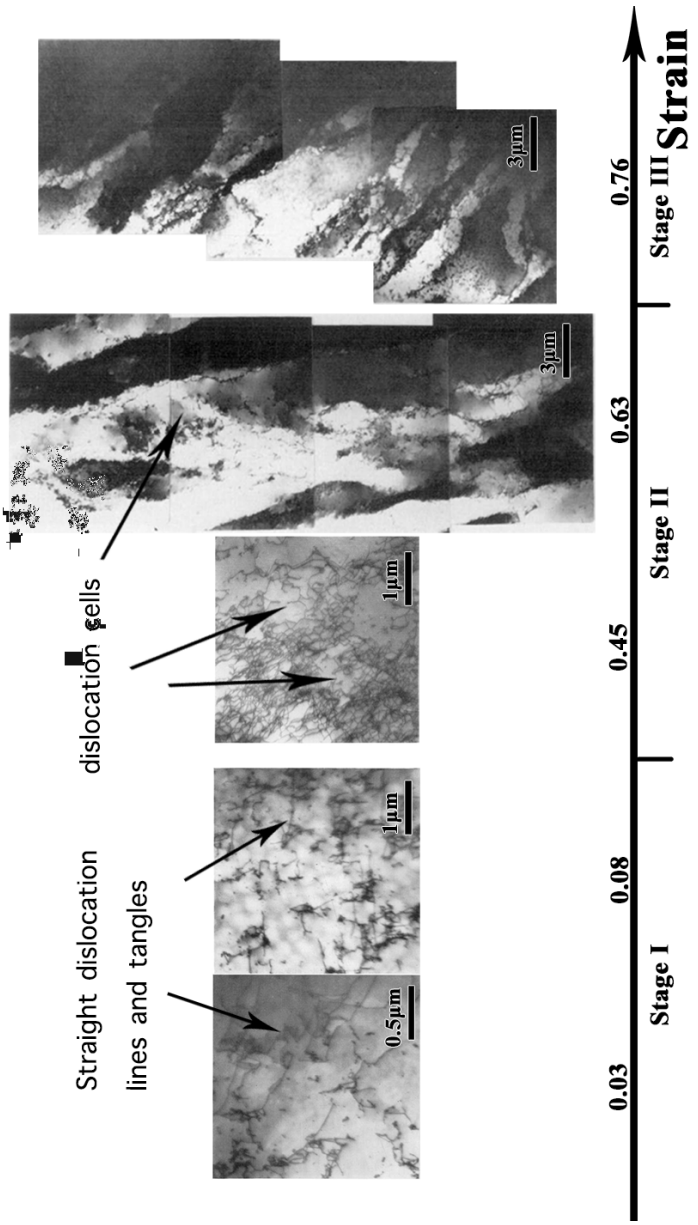


Figure 2.1: TEM micrograph of dislocation structure evolution as a function of strain in quasi-static deformation [8].

## 2.2 Shock compression of materials

### 2.2.1 Historical overview

The theory of shock waves dates from the 1870s, when Rankine and Hugoniot gave a description of the states of a material (on the base of fluid mechanics theory) on both sides of a shock wave, in one dimensional flow in fluids/solids [9]. A shock wave, in short, is a type of disturbance propagating in the material, with a discontinuous change of state (pressure, temperature, density, etc.) at the shock wave front [10]. It occurs when the material is impacted by a high speed projectile, or detonation waves from explosives. In the early years of the theory development, the shock waves in solids did not attract much attention, until World War II. It was realised that the development of nuclear weapons required a knowledge of the state of solids in shock compression [10]. Therefore the early work in this field was mostly confined to the measurement of the compressibility of metals resulting from contact detonation waves [11]. The first modern paper on shock compression in solids was written by Walsh and Christian, who presented an expression for the equations of state of aluminium, copper and zinc using Hugoniot data [12]. The Hugoniot of a material is the locus of pressure, volume or energy attained by a single high pressure shock compression. The detailed theory of the Hugoniot of materials will be given in section 2.2.2. After Walsh and Christian's work, many techniques for material examination in shock loading were developed, such as explosives, laser and guns for producing the shock, and electromagnetic/optical gauges for determining the state of materials in shock [10]. Among the various shock wave generating methods, gas

guns are a useful tool for studying the material behaviour under simple conditions. The principle of the gun operation is based on suddenly releasing compressed gas behind a projectile to accelerate it through the gun barrel. The shock wave generated by the projectile can be finely adjusted to be a perfect plane wave with the assistance of a tilting system. The pressure of the shock wave produced by a gas gun can be up to a few tens of GPa, where the Hugoniot elastic limit (HEL), spallation and strain rate effects on the material can easily be studied. In this thesis, the discussion of shock loading experiments will be confined to the gas gun.

A popular system for detecting the state of a material is HetV (velocity interferometer system for any reflector). The light reflected from the specimen is processed by lenses and forms a set of fringes, which can be analysed to determine the state of the material [10].

The most important requirement in studying shock waves nowadays is to examine the shock response of a material and to investigate the material deformation mechanisms under shock loading [13]. It is becoming key for the selection and improvement of materials used in many fields, like the aerospace industry, satellite protection and high rate machining. For example, after a plate impact investigation, an aerospace alloy: $\gamma$ based titanium aluminide, with a duplex microstructure and smaller grain size is shown to be stronger than a coarser grain, fully lamellar microstructure at a shock pressure of around 10GPa [14]. This indicates that TiAl with finer grains is more suitable for use at high pressure. The plastic deformation of material under shock loading is mostly undertaken by dislocations and twinning. Studies of material dislocations and deformation twinning in shocked condensed material not only

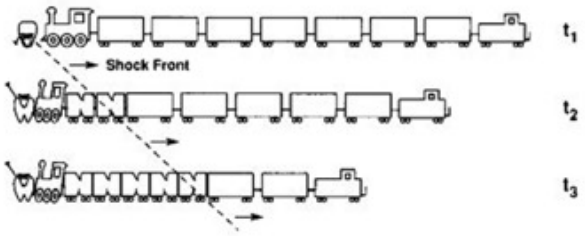


Figure 2.2: A simple train model of a shock wave [10]

give a good explanation of the material behaviour, but also give guidance to material improvement. For instance, deformation twinning was the dominant substructure observed within the [001] grains of copper bicrystals after 10 GPa shock, but not in [011] grains, which shows the orientation sensitivity of the deformation mechanism [15]. When metals with an FCC structure are used in shock loading situations, the texture can thus be adjusted to give better properties. A review of the deformation mechanisms under shock loading will be presented in section 2.3.

### 2.2.2 Equation of state

A wave is a type of disturbance propagating through a material. A wave is graphically illustrated in Figure 2.2, where a bull is impacted by a moving train. The density of the carriages would increase successively from the impact interface to the right side. The interface between the compressed and the uncompressed material is a wave. A wave in a solid can be produced anywhere in our daily life. For instance, when a door is being knocked, a elastic wave is produced at the knocked point and propagates into the door. It then penetrates the air, transferring to a sound wave that can be heard. When the stress of the wave is higher than the yield point of

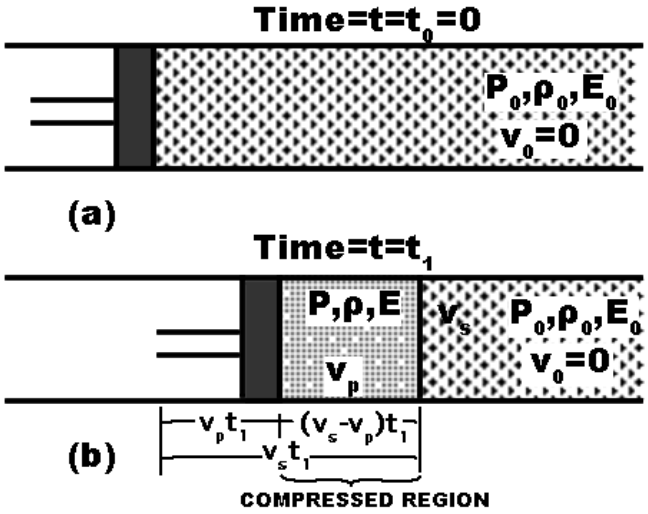


Figure 2.3: A parametrised model of shock compression [16]. In (a) at time $t_0$ the piston (with velocity $v_p$) starts to impact the material which have an original state (pressure $P_0$, density $rho_0$, energy $E_0$ and velocity $v_0$). In (b) at time $t_1$ the the piston moves forward for a distance of $v_p t_1$ and the shock wave (with velocity $v_s$) moves to $v_s t_1$. The shock compressed material have a state of pressure $P$, density $rho$, energy $E$ and velocity $v_p$.

the material, the material will plastically deform. This wave is then a plastic wave. When the material is subjected to rapid impulsive loading where the time of the load application is too short for the material body to respond inertially, a shock wave is produced. The material state undergoes a discontinuous change at the shock wave front. In daily life, a shock wave can be generated by an object moving at high speed, like a bullet, or an aircraft strike by a flying bird.

The shock wave phenomenon is shown parameterised in Figure 2.3. A piston is pushed into a compressible material in a tube and a shock wave front generates from the interface. The compressed material has an initial state of pressure $P_0$,

density $\rho_0$, velocity $v_0$ and kinetic energy $E_0$. The compressed region has a stable state $P$, $\rho$, $E$ and velocity $v_p$ and it keeps expanding with the shock wave velocity $v_s$ towards the right. The relationship between these parameters can be described by four equations as shown below (as Equation 2.1) [16].

$$\begin{aligned} \rho_0 v_s &= \rho(v_s - v_p) \\ P - P_0 &= \rho v_s v_p \\ E - E_0 &= 1/2(P + P_0)(1/\rho_0 - 1/\rho) \\ v_s &= C_0 + S_1 v_p \end{aligned} \tag{2.1}$$

where the equations represent the conservation of mass, momentum, energy and the relationship between wave velocity and particle velocity, respectively. The last equation, with constants $C_0$ and $S_1$, is the characteristic equation of the material for the shock compression state. Obviously from the last equation there is a linear relationship between $v_s$ and $v_p$ (the speed of the shocked part of the material). $C_0$ and $S_1$ are material constants, also known as the Hugoniot parameters of the material. $C_0$ is the speed of sound in the material and $S_0$ is experimentally measured in the shock impact. They describe the compressibility of the material under shock loading. Determining them used to be the most important part of research on the shock compression of solids [17].

There are five unknown parameters in the shock wave equation of state: $P$, $E$, $\rho$, $v_s$ and $v_p$. If the shock constants of the material are known, we only need to know one to determine the others, and therefore get to know the whole state of

the material under shock. It is also easy to find the relationship between any two parameters. There are thus many useful graphs for describing the state of a material under shock loading, such as those connecting $P - V$, $P - v_p$ or $P - x$, etc.

### 2.2.3 Jump conditions and Hugoniot elastic limit

The relationship between the pressure and the volume of the material can be solved via the equation of state, as shown in equation 2.2 [16]:

$$P = \frac{C_0^2(V_0 - V_1)}{[V_0 - S(V_0 - V_1)]^2} \tag{2.2}$$

The $P - V$ relationship can easily be transferred to the stress-strain curve of a material in shock loading since it represents the volume of a material under uniaxial pressure. A theoretical stress-strain curve of a material in shock compression from equation 2.2 is shown in Figure 2.4 (labelled as the Hugoniot). This curve assumes that the material behaves linearly under the stress, without any yield phenomenon or work hardening. The actual stress-strain curve is the stress-strain Hugoniot shifted upward, due to the elastic deformation of the material (shown as $OA$ in figure 2.4). At the start of loading, the material will firstly be elastically deformed, and then yield plastically. The yield point is called the Hugoniot elastic limit (HEL). The theoretical value of the HEL is [16]:

$$Y_{HEL} = \frac{1 - \upsilon}{1 - 2\upsilon} Y \tag{2.3}$$

where $\upsilon$ is the Poisson's ratio of the material and $Y$ is the yield strength. This

relation is obtained by considering the elastic relation between the longitudinal stress ($\sigma_x$) and the longitudinal stress ($\sigma_y$ and $\sigma_z$) under one-dimensional strain, where Hooke's law can be applied as:

$$\begin{aligned} \upsilon_x &= \frac{1}{E}[\sigma_x - v(\sigma_y + \sigma_z)] \\ \upsilon_y &= \frac{1}{E}[\sigma_y - v(\sigma_x + \sigma_z)] \\ \upsilon_z &= \frac{1}{E}[\sigma_x - v(\sigma_x + \sigma_y)] \\ \sigma_y &= \sigma_z \end{aligned} \tag{2.4}$$

Therefore $\sigma_y = \sigma_z = \frac{v}{1-v}\sigma_x$. Applying von-Mises yield criteria $\sigma_x - \sigma_y = Y$. The Hugoniot elastic limit $Y_{HEL} = \sigma_x$ result in equation 2.3.

However, the actual $HEL$ of a material is usually very different from the theoretical value. A precondition of the equation is the Von Mises yield criterion. The initial stress for dislocation movement not only depends on the shear stress, but also varies with temperature, normal stress, etc. In shock loading, because of the discontinuity at the wave front, the state of the material will jump from the zero point to the HEL, and then jump from the HEL to a point corresponding to the pressure of the shock wave, shown as the Rayleigh line in Figure 2.4. This is because the speed of wave with certain pressure on the curve is proportional to the slope of the curve, when a wave with pressure $A - B$ propagate through the material, the wave $B$ travels faster than wave $A$ and will catch up with wave $A$, creating a discontinuity $'$jump$'$ from pressure $A$ to $B$ [16]. When the shock wave pressure is high enough,

the slope of the Rayleigh line is higher than the elastic constant and the material will jump directly from the zero point to the shock wave pressure, where a strong shock wave is generated.

### 2.2.4 The wave interactions

According to the equation of state, the relationship between the material pressure $P$ and the particle velocity $v_p$ can be written as [16]:

$$P = \rho_0(C_0 v_p + S v_p^2) \tag{2.5}$$

Since $\rho_0$, $C_0$ and $S$ are constant, there is a squared relationship between the pressure and the particle velocity. Figure 2.5 is an example of the $P - v_p$ relationship for several materials, where the pressures on materials are plotted against the particle velocities. It can be seen that when the material is not being loaded, the particle velocity and the pressure are both zero; and when the material is accelerated to a certain particle velocity by the shock wave, the pressure increases parabolically. This $P - v_p$ diagram can also be used to present the wave-wave and wave-surface interaction. A wave-free surface interaction is shown in Figure 2.6. When a shock wave reaches a free surface, the boundary condition requires that the pressure in the material returns to zero. A rarefaction wave is reflected back into the material, releasing the pressure and accelerating the material. The state of the compressed material follows profile 1, with the shock peak pressure at $A$ on the profile. The state of the coincidence point of the shock wave and the free surface is at the point $A$. By solving the equation of state it can be determined that the material at the free surface

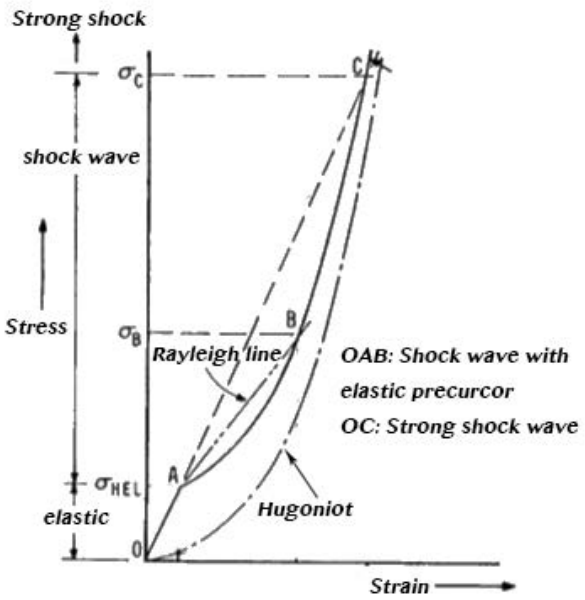


Figure 2.4: Regions of elastic, shock and strong shock wave propagation [10]. The Hugoniot curve is the theoretical state of the material in the shock loading from the equation of state. The 0-A-B-C curve is the state of the material in the shock loading with a yield strength. The point A is the yield point with pressure $\sigma_{HEL}$. The pressure between $\sigma_{HEL}$ and $\sigma_C$ creates a shock wave with a elastic precursor, since OA have higher slope than AB (B is a state of material between A,C), the elastic wave moves faster than AB. A pressure over $\sigma_C$ can create a strong shock wave without elastic precursor because the velocity of the shock wave is faster than the elastic wave. Please see text for the definition of the Rayleigh line.

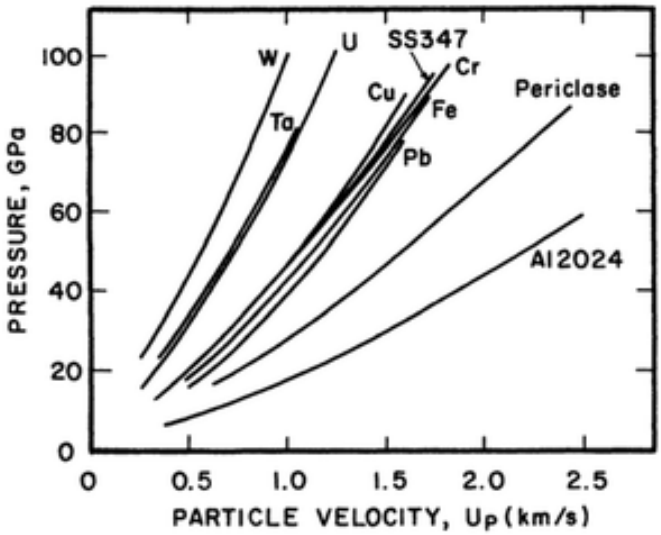


Figure 2.5: Calculated $P - v_p$ curve for several materials [10]. It shows the characteristic relationship between the shock loading pressure and the particle velocity ($U_p$ is $v_p$ in this thesis) of different materials.

will follow profile 2, with a final particle velocity $2v_p$, and zero pressure at point B. The free surface velocity is often measured in a shock compression experiment and is used to determine the particle velocity of the material under loading.

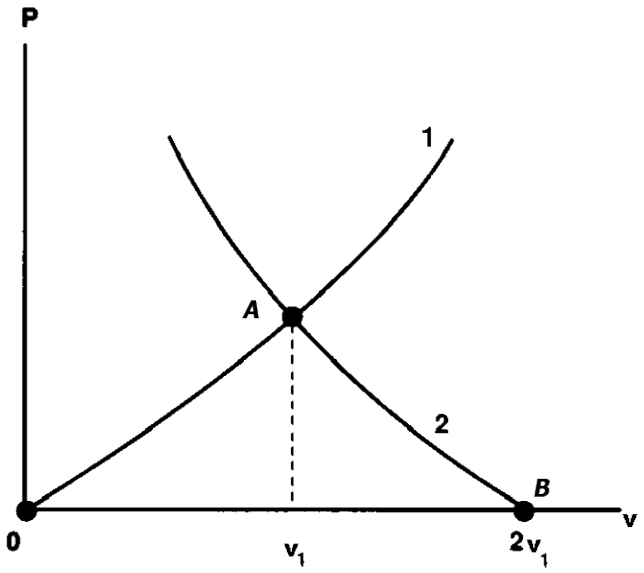


Figure 2.6: $P - v_p$ diagrams for shock reflection from a free surface [10]. The curve 1 represents the material being shock loaded from pressure 0, velocity 0 to state A. The curve 2 represents the material being released from A to state B with pressure 0 and velocity $2v_1$

### 2.2.5 Shock wave propagation in an impact experiment

The plate impact experiment is a very important technique for testing a material's dynamic properties in shock wave loading. In this experiment, a flat shock wave is generated at the entrance surface of the specimen, producing a uniaxial strain. Only the principal strain along the wave propagating direction is non-zero. The response of the material (free surface velocity) can be measured to calculate the theoretical characteristic parameters in equation 2.1. To achieve this one-dimensional wave

structure, lateral strain of the material needs to be prevented, otherwise the material would accelerate laterally outwards as the plate is compressed and induce a radial stress release wave which would propagate radially inward and progressively destroy the uniaxial strain in the specimen.

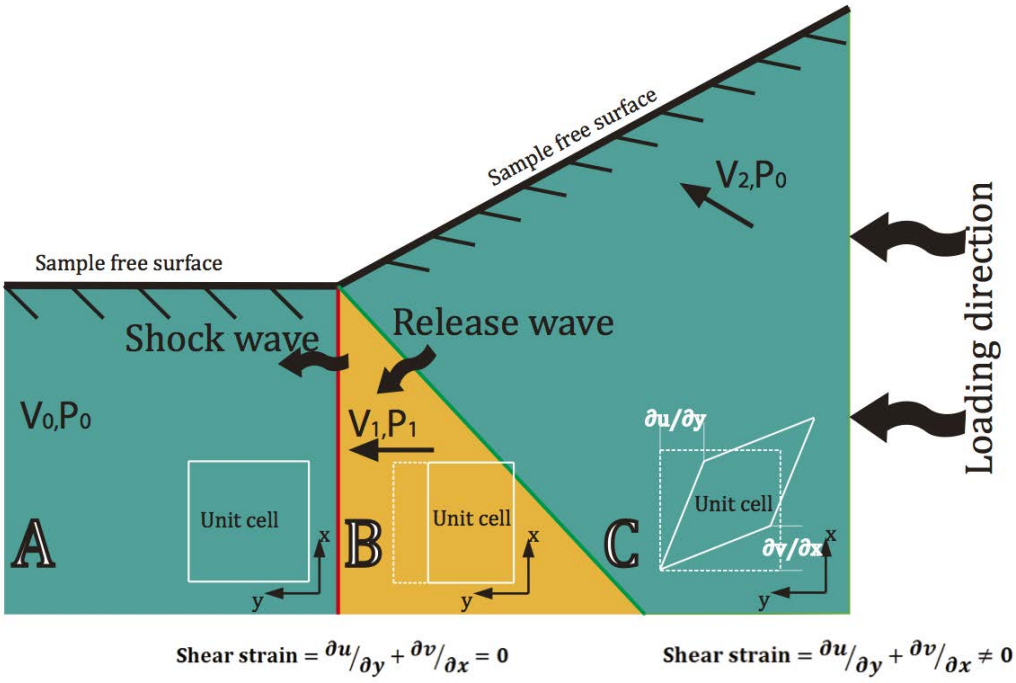


Figure 2.7: Sketch showing the wave movement at the edge of the specimen. A planar shock wave is travelling right to left. The region on the left side is the undeformed material, with no strain; the yellow part is one-dimensionally compressed material, with the particle velocity towards the left side, and with longitudinal strain but no shear strain; the region on the right hand side is unloaded by the release wave, with particle velocity to upper left, and with shear strain. The extent of the release has been exaggerated to make the diagram clearer.

A significant effect can be caused by the convergent radial release wave. Experimental results by Stevens in 1972 [1] show that the radial release wave induced by a $12kbar$ impact in an aluminium single crystal can produce plastic flow. The nature

of the lateral release wave is a mixture of the unloading and a shear stress wave. The unloading part will release the stress/pressure in the shocked region of the material body. The shear stress in the lateral release wave is caused by the wave obliquity. A schematic diagram of the release wave structure is shown in Figure 2.7. The material is being loaded by a shock wave moving towards the left of the figure. The region $A$ on the left side is virgin material with velocity $v_0$ and pressure $P_0$. After the shock front passes, region B experiences one-dimensional strain along the $y$ axis, with a strain $\frac{1}{2}(\partial u/\partial y + \partial v/\partial x) = 0$, where $u$ and $v$ are the displacements in the $x$ and $y$ directions. If the material is restored to environmental pressure with a back release wave, the compressed region will keep moving along the $y$ axis, without any shear strain in the $x$ and $y$ directions. However, if there is no constraint in the lateral direction to keep the material from extending, the pressure of the shocked material will push the material up (region $C$ in Figure 2.7), and having a velocity along the $x$ axis, a release wave is formed. The vector of the release wave velocity will be the combination of the shock wave velocity and the release wave velocity moving to the sample centre. The region $C$ has ambient pressure $P_0$ and particle velocity $v_2$. $v_2$ has a component in the $x$ direction because the material is moving up. Thus the material in region $C$ is being distorted along the $x$ axis. This results in a non-zero shear strain along the $x$ and $y$ axes $\frac{1}{2}(\partial u/\partial y + \partial v/\partial x)$ [18], which is very high that could be comparable with the strain induced by the longitudinal pressure [19]. This high shear strain (rate) is experienced by the whole sample, but varies with location and wave velocity. The misalignment of the release wave velocity and the particle velocity of the material is called wave obliquity [20]. In a conventional plate impact

experiment, the lateral release wave is usually avoided by using a momentum trap, to confine the material from lateral extension, as shown in Figure 2.8.

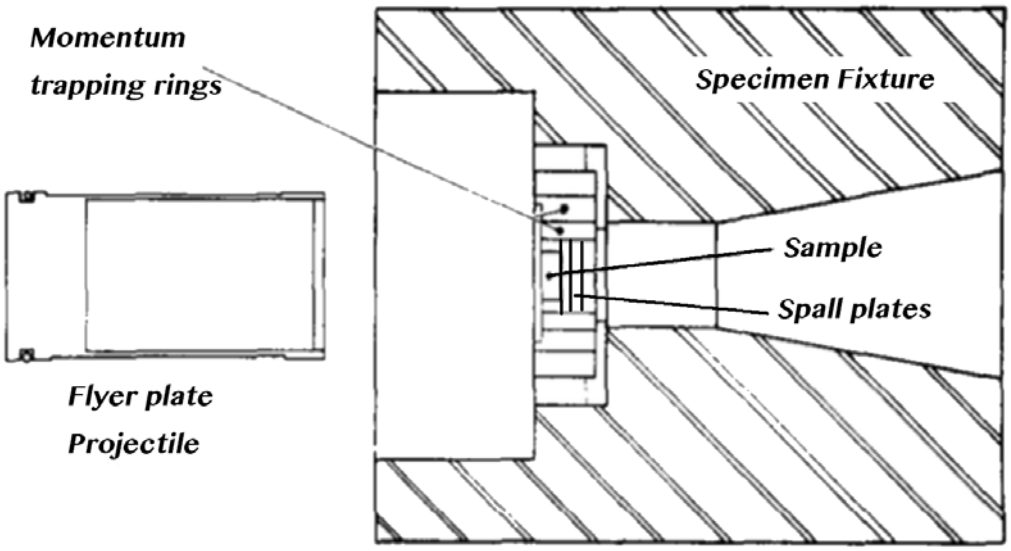


Figure 2.8: Schematic drawing of a shock recovery fixture [21]. The flyer plate projectile moves from the left and impact the sample plates to generate a shock wave.

Another disturbance to the one-dimensional shock recovery experiment is the release wave from the back surface of the specimen. Unlike the long tube being impacted in Figure 2.2, the specimen used in a shock recovery test is usually a small disc, with typically a diameter of a few centimetres and $1-2$ centimetres thickness. When the shock wave front meets with the free surface of the specimen, the interaction will produce a release wave. This can easily be deduced from the shock equation of state 2.1 and can be depicted by the $P-v_p$ diagram in Figure 2.6.

This shows that when the material is released to environmental pressure, the particle velocity would be doubled to $2v_p$. In the pressure-distance diagram in Figure 2.9, at $t_0$ the shock front and release wave from the projectile back surface are propagating to the right side. The material between these two waves is compressed by the shock front, with particle velocity $v_p$ and pressure $P$. The shock front meets the free surface at time $t_1$. It is reflected and moves backwards to the other release wave. When they meet and interact, the zone between the two waves has a $'$negative$'$ pressure, i.e. tension. When the tension exceeds the material strength, the material splits apart, or $'$spalls$'$. This usually manifests itself in a shocked specimen as voids.

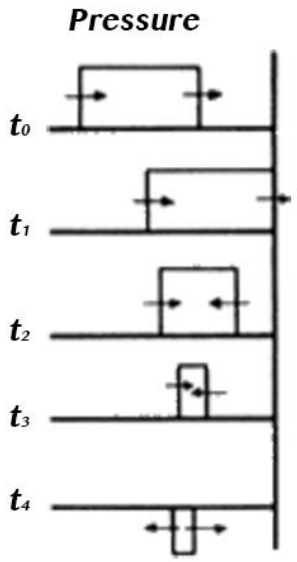


Figure 2.9: Reflection of a shock wave at a free surface [16]. At $t_0$ the shock wave front and release wave move towards a free surface. The shock wave front is bounced back by the free surface between $t_1$ and $t_2$. The release waves meet between $t_3$ and $t_4$ and produce a area with negative pressure (tension).

In a shock experiment for determining the Hugoniot of the material, a fixture assembly is normally used to avoid the disturbance from a radial release wave and the spalling. A sketch of the setup is shown in Figure 2.8. The radial release wave can be stopped by momentum traps and the back release wave can be avoided by using a set of spall plates.

The major requirement in the field of shock loading studies is to determine the material's response and deformation mechanisms in the one-dimensional shock condition, where the material is only loaded by a plane shock wave and released by

a plane release wave in the same direction. However, material behaviour under more complex loading conditions receives less attention. The deformation mechanisms in an oblique wave (especially a radial release wave) are still not very clear.

The projectile impact experiment can be fully described by an $x-t$ diagram. Figure 2.10 shows an $x-t$ diagram for a stationary specimen disc impacted by a projectile of the same material with a velocity of $v_p$. For the convenience of the drawing, the coordinate is selected to be a point between the two objects, moving at a velocity of $\frac{1}{2}v_p$ towards the specimen, so that the impact happens at the zero point of the $x$ coordinate. The $x$ axis shows the location of the waves and the interface between the materials. The $y$ axis is time. This diagram can show the wave movement through time. At time $t_0$, there is a gap between the surface of the projectile and the target. They are moving towards each other and meet at time $t_1$, where two shock waves are generated at the interface. The shadowed area of the material is compressed by the shock wave. The two shock waves are propagating towards the back surface. At time $t_2$, the shock waves bounce back from the free surfaces, transferring to two release waves. The released areas of the specimen and target have velocities of $-\frac{1}{2}v_p$ and $\frac{1}{2}v_p$. The two release waves meet at the interface between the two objects at time $t_3$. Then the projectile and the specimen separate due to opposite velocities. In a practical experiment, when spall plates are used, the shock wave will exit the specimen without release. The material will remain under pressure until released by the release wave from the back surface of the projectile. As shown in Figure 2.11, the release wave reflected from the projectile back surface (at $t_2$) will keep moving after propagating through the target/projectile interface

at $t_3$, unloading the specimen pressure to 0 and exiting the specimen via the back surface at $t_4$.

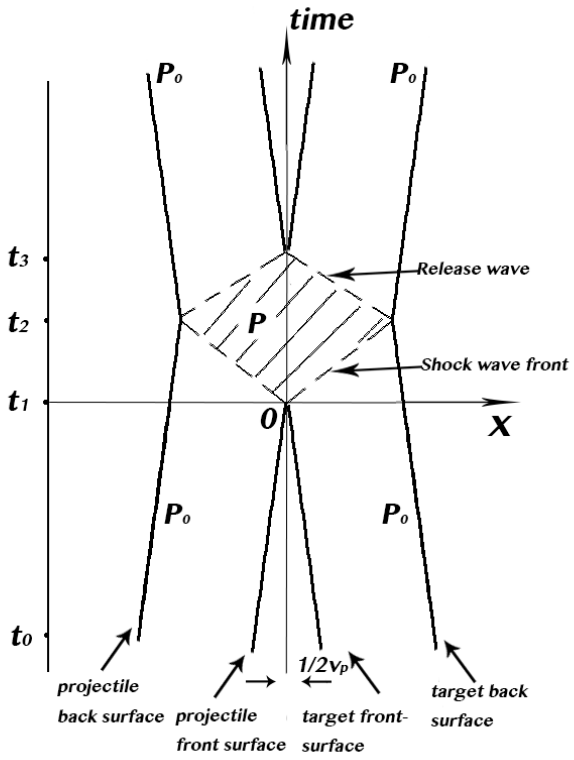


Figure 2.10: The $x - t$ diagram for wave propagation in the projectile and target. At time $t_0$ the specimen and projectile start to move towards each other and they meet at position 0 at time $t_1$. In the shadow area the material is compressed to a pressure P. After the specimen and projectile being compressed and released, they separated at time $t_3$.

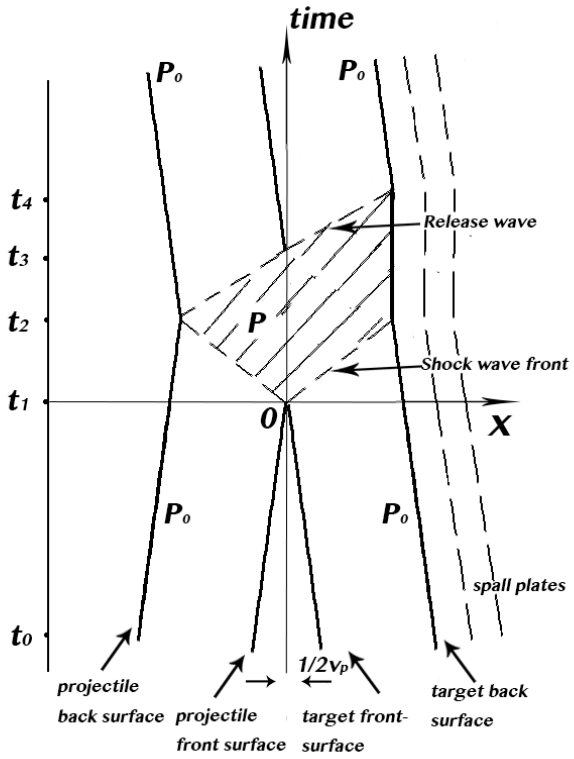


Figure 2.11: The $x - t$ diagram for wave propagation in the projectile and target with spall plates. The shock wave propagates through the sample back surface at time $t_2$ without reflection back into specimen. The release wave from projectile back surface enters the specimen at time $t_3$ and exit from the back surface at time $t_4$.

### 2.2.6 The shock wave profile

From the viewpoint of the material at the front surface of the specimen in Figure 2.11, it is loaded by the shock wave at $t_1$, and unloaded by the reflected release wave

at $t_3$. The pressure suffered by the material at point X can be represented using the $P - t$ profile (Figure 2.12), in which the $y$ axis is the pressure and the $x$ axis is the time. The shock wave arrives at point X at time $t_1$ and compresses the material to pressure $P$. This pressure holds until $t_3$, when the release wave arrives and the pressure is gradually decreased to zero. The twisting of the plot on the shock front is due to the initiation of dislocation plastic flow and twinning/phase transformations. If these phenomena are absent, the twisting will not appear in the profile. During pressure release, the material will be released elastically first and then plastically.

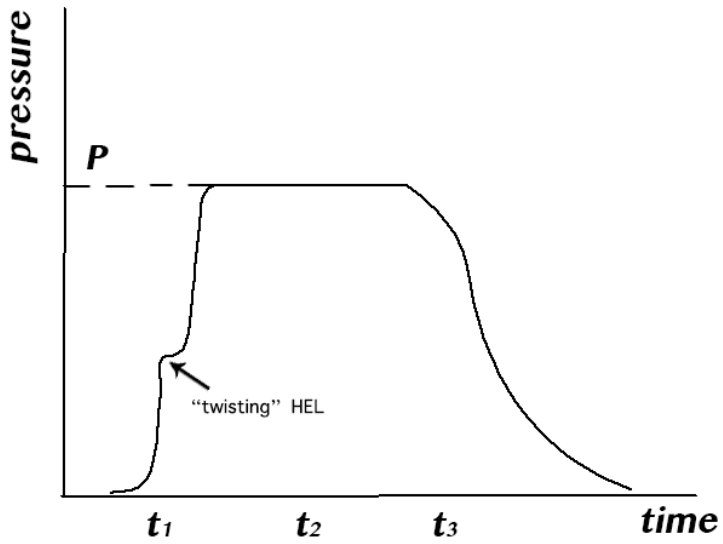


Figure 2.12: Schematic diagram of pressure of a point of a material in shock loading. The elastic wave arrives at the point at time $t_1$. The pressure rises rapidly to the HEL point, and then go up to the shock pressure P with a slower rate. The release wave arrives at the time $t_3$ and gradually unload the material to pressure 0.

## 2.3 Micromechanics of shock compression of solids

Continuum solid mechanics has been successful in describing the shock compression process. However, micromechanics concepts such as the crystal lattice and dislocations are not considered in shock mechanics. The relationship between macro-scale deformation and the underlying micro-scale processes are therefore not thereby ex-

plained. Micro-scale mechanisms can be studied either by real time observations, or post-shock microstructure studies. The real time defect behaviour is difficult to analyse because the time for the shock deformation is usually a few microseconds. Therefore the existing micro-mechanisms are all established based on substantial 'guesswork' through post shock microstructure studies. More recent research on the deformation mechanisms has sometimes included computational simulations of the dynamic behaviour of crystal defects and comparison with the post shock microstructure examination.

The first attempt to interpret the metallurgical effect of shock waves in terms of dislocations was made by Smith [22]. In his model (Figure 2.13), a small volume of specimen at the shock front is selected as representing the deformation. If there are no dislocations produced by the shock wave, the material behind the shock wave front would be compressed uniaxially with strain $\varepsilon$ along the $x$ axis. The strain tensor can be written as:

$$\begin{pmatrix} \varepsilon & 0 & 0 \\ 0 & 0 & 0 \\ 0 & 0 & 0 \end{pmatrix}$$

If the compression strain is hydrostatic, the strain tensor becomes:

$$\begin{pmatrix} 1-\sqrt[3]{1-\varepsilon} & 0 & 0 \\ 0 & 1-\sqrt[3]{1-\varepsilon} & 0 \\ 0 & 0 & 1-\sqrt[3]{1-\varepsilon} \end{pmatrix}$$

Although the strains in these two conditions are different, the dimensions of the compressed volume stay the same. Figure 2.13 shows a schematic sketch of the strained condition. The unit elements with hydrostatic strain are compressed evenly in all directions, with the material flow to the side of the sampled volume. The elastic strain energy of the uniaxial condition is much higher than for the hydrostatic one. The change from uniaxial to hydrostatic strain can be achieved by dislocation motion. Smith's model in Figure 2.13 shows a possible route. A row of straight edge dislocations is produced behind the shock front, moving with the wave and producing the plastic flow. In three dimensions, a second group of dislocations oriented perpendicular to the paper is needed to accomplish the strain on the vertical axis.

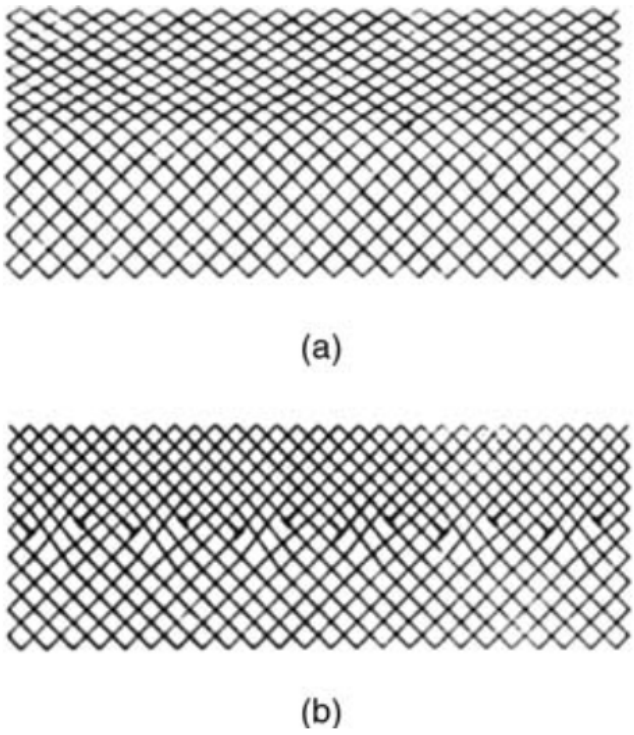


Figure 2.13: The Smith model for dislocation generation at the shock front [22]. The uniaxial strain in (a) is resolved to hydrostatic in (b) by an array of dislocations. See text for detail of the model.

Smith's model is a good conceptual model to describe the material flow under shock loading. However, it cannot be used as a guiding model since it does not involve screw dislocations which are commonly observed after shock. It requires the dislocations to move supersonically, which is theoretically not possible to achieve. Hornbogen solved the screw dislocation problem by replacing the edge dislocations in Smith's model with a screw dislocation dipole with an edge segment at the end [23].

This model explained the residual high density of screw dislocations in shocked $\alpha$-iron. Meyers improved Smith's model, assuming the dislocations are homogeneously produced behind the shock front and move subsonically. New dislocation interfaces are generated periodically as the shock wave propagates through the material [24].

The relaxation time from one-dimensional strain to a near-hydrostatic state is very short. At low pressure (under $10GPa$) the stress can be relaxed in about $10ns$, which corresponds to a $40\mu m$ distance behind the shock front. However, this is very dependent on the initial mobile dislocation density and microstructure of the material, since the stress relaxation is based on a classic dislocation motion/multiplication mechanism. For a shock wave at high pressure, homogeneous nucleation is activated to decrease the time for strain relaxation. A typical value is $3.5ns$ for a $60GPa$ shock compression[25].

Lots of other structural changes can occur during the plastic deformation of metals, such as twinning [26] [27] [28], phase transformation [29] [30] and fracture [31]. Mechanical twinning has mainly two effects on plastic deformation: (1) It can subdivide the grains, acting as a barrier for dislocation slip, and therefore increase the work hardening rate. (2) It can make a contribution to the plastic deformation and reduce the work hardening rate [32]. Twinning is produced when the stress required for dislocation glide is higher than the activation stress for twinning[32]. The change of deformation mechanism from dislocation slip to twin is called the slip-twin transition. The critical event for deformation twinning is mostly nucleation, which usually requires more stress than growth. It has been found that the stress for dislocation slip is much more sensitive to temperature and strain rate than is the

twinning stress [13]. In the analysis of the slip-twin transition, the required twinning shear stress can therefore be treated as a constant. When the slip stress is increased to reach the critical stress for twin nucleation, the deformation transfers from slip to twinning. Figure 2.14 shows the slip ($\sigma_S$) and twinning ($\sigma_T$) stress against shock loading pressure of nanocrystalline nickel, with a critical pressure of $78GPa$. When the shock pressure is higher than this value the slip stress becomes higher than the twinning stress and slip is replaced by twinning [13].

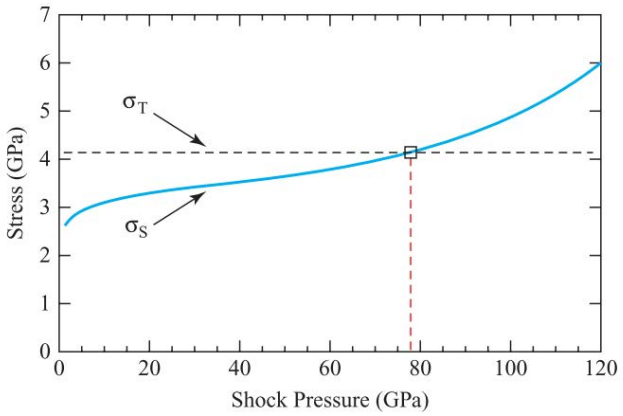


Figure 2.14: Slip and twinning stress versus shock pressure for nanocrystalline nickel with a grain size of $30nm$. The twinning stress $\sigma_T$ is seen as independent with the shock pressure which the slip stress is very sensitive to. When the shock stress is under $78\,GPa$ the stress required for twinning is higher than slip. When the shock stress is higher than $78\,GPa$ the twinning stress is lower and therefore twins activated. The twinning threshold is $78\,GPa$ [13].

## 2.4 Deformation of tantalum in shock loading

### 2.4.1 Hugoniot elastic limit

The Hugoniot elastic limit of tantalum is $1-3GPa$ [31][33][34]. The yield behaviour of tantalum in shock loading is strongly influenced by the material and the shock conditions (e.g. grain size, deformation history and travelling distance of the shock wave). A summary of the HEL measurements on tantalum is shown in Table 2.1. The elastic precursor decay effect reduces the HEL with a longer wave travelling distance, as seen from the Rasorenov's work [31], the material with grain size $50\mu m$ and wave travelling distance $0.64mm$ has higher HEL ($3.24GPa$) than the material with same grain size and longer wave travelling distance ($1.98mm$ and $2.12GPa$ HEL). A material with a larger grain size will have a higher Hugoniot elastic limit. With the same sample thickness (same wave travelling distance), the ultra fine grain tantalum has lower HEL than the as-received specimen. Preshock treatment of a sample will decrease significantly the HEL. The slip systems of tantalum in shock loading are $\langle 111 \rangle$ on $\{110\}$ and $\{112\}$ [35][36].

### 2.4.2 Dislocations and hardening

Shock waves can work harden metals due to the increase in dislocation density. In tantalum, the work hardening by shock is similar to the strengthening effect of quasi-static deformation for the same strain [36]. The cross slip of tantalum is restricted at high strain rate. The dislocation storage is rate-independent, only being related to the shock strain[36]. Figure 2.15 is a summary of the dislocation densities

Table 2.1: The HEL of tantalum in shock loading from the literature

| HEL (GPa) | Grain size ($\mu$ m) | Sample thickness (wave travelling distance) (mm) | Comments |
|---|---|---|---|
| 3.24 | 50 | 0.64 | As-received[31] |
| 2.12 | 50 | 1.98 | As-received [31] |
| 2.66 | 0.5 | 0.68 | Forged to ultra fine grain [31] |
| 1.83 | 0.5 | 2.11 | Forged to ultra fine grain [31] |
| 2.0 | 50 | 0.6 | Pre-shocked $40GPa$ [31] |
| 1.7 | 50 | 2.0 | Pre-shocked $40GPa$ [31] |
| 1.85 | - | 7 | [33] |
| 2.06 | - | 5 | [33] |
| 2.25 | 30-60 | - | [34] |

reported in the literature. The dislocation density measured by every author from their own experiment shows the grain size has a strong effect on the dislocation density: materials with large grains (or single crystals) generate more dislocations in shock loading. This is probably because the annihilation of dislocations at the grain boundaries reduces the density of dislocations in the polycrystalline material [28]. However the results from different author don't follow. For example, the nano-grain tantalum of Lu has higher dislocation density (green square at 50 GPa) than Podurtes's $0.7\mu m$ tantalum loaded at the same pressure (blue circle on the left side). The probable reason for this is the materials used by different author are slightly different in interstitial element.

The dislocation substructures produced by shock in tantalum are similar to those after quasi-static deformation: screw dislocation dipoles, loops, heavily jogged dislocation tangles $\rightarrow$ dislocation cells [28][29][39][36]. The residual dislocation substructure after shock loading is summarised in Table 2.2. The dislocation structure

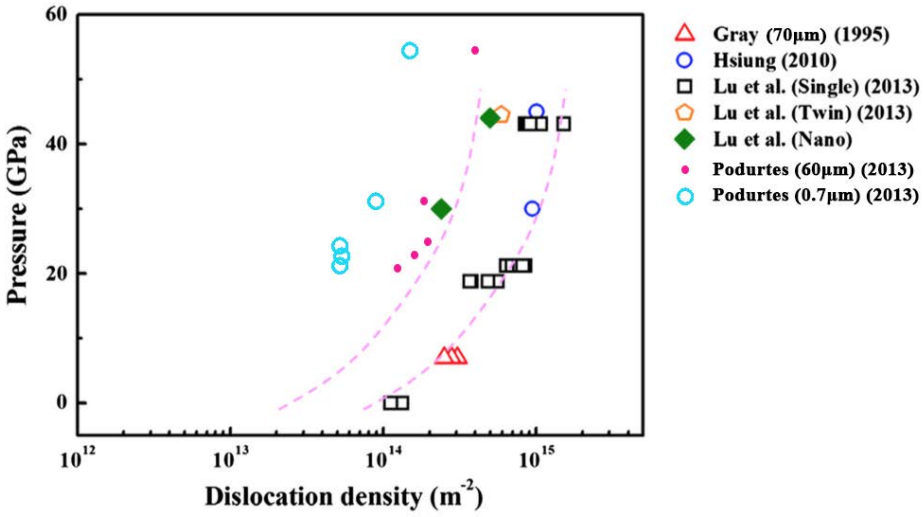


Figure 2.15: Dislocation density as a function of the shock pressure [36] [37] [38]. Please see text for detailed explanation for shock pressure and grain size effect.

is consistent with the hardening effect, showing similar microstructure evolution to quasi-statically deformed specimens. The dislocation micrographs of tantalum after shock loading from the literatures are shown in Figure 2.16.

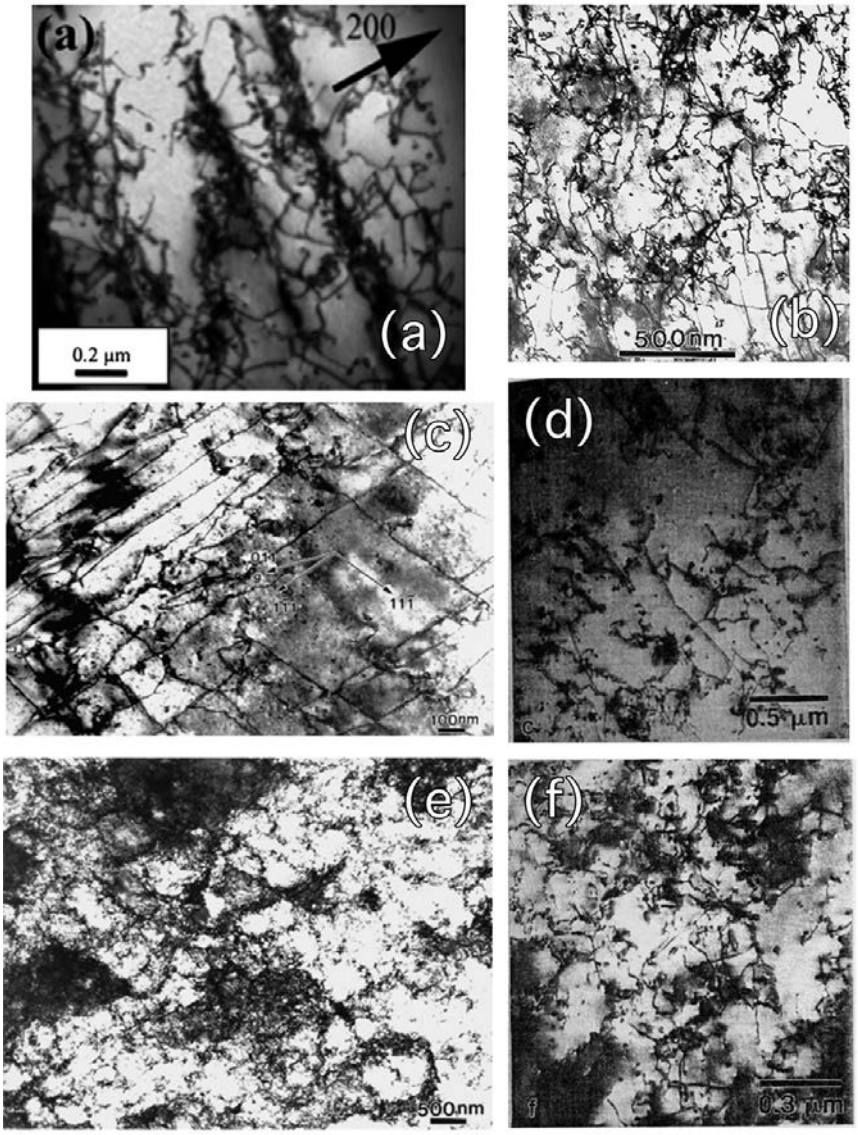


Figure 2.16: TEM dislocation micrographs of (a) 35 $GPa$ laser shocked tantalum single crystal[28]; (b) 15 $GPa$ plate impacted tantalum [29]; (c) 45 $GPa$ plate impacted tantalum single crystal [29]; (d) 7 $GPa$ plate impacted tantalum [36]; (e) 45 $GPa$ plate impacted tantalum [29]; (f) 20 $GPa$ plate impacted tantalum [36]

Table 2.2: Dislocation substructure of shock loaded tantalum

| Shock pressure (GPa) | Grain size ($\mu m$) | Comments |
|---|---|---|
| 30-40 (Laser) | 0.07 | Loose dislocation network, very low density due to annihilation at grain boundary. [28] |
| 35 (Laser) | Single crystal | Dislocation tangles, walls. [28] |
| 15 (Plate impact) | 50 | Loose, squiggly dislocation lines.[29] |
| 45 (Plate impact) | Single crystal | $'$Cross grid$'$ straight strew dislocations.[29] |
| 45 (Plate impact) | 50 | Dislocation cell size 0.5 $\mu m$.[29] |
| 50 | Single Crystal | High density jogged dislocations and debris/clasters.[39] |
| 7-20 | 70 | (a) Screw dislocation dipoles with edge cusps on the long screw segments.<br>(b) Dislocation tangles with mixed character.<br>(c) Loops and debris.[36] |

### 2.4.3 Twinning

Twinning is frequently observed in tantalum after recovering from shock loading. Table 2.3 is a summary of the twinning observed in shock impact experiments on Ta. The threshold pressure of tantalum is still subject to debate as the experimental results are controversial. The measured threshold from laser compressed tantalum single crystals is $35GPa$, under which pressure the stress required for dislocation slip is lower than the twinning nucleation stress [37]. Meyers calculated the theoretical critical pressure for twinning in tantalum using a constitutive model [32], giving a pressure in the range $35 - 71GPa$. The tendency for twinning is high at high strain rate and low temperature, because the dislocation flow stress can be raised effectively up to the critical stress for twin formation. This may be deduced directly from the high strain-rate and thermal sensitivity of dislocation glide. The flow stress for dislocations can be represented using the Zerilli-Armstrong equation 2.6 :

$$\sigma_s = \sigma_G + C_1 exp[-(C_3 - C_4 ln\frac{\dot{\epsilon}}{\dot{\epsilon}_0})T] \tag{2.6}$$

| Shock Pressure (GPa) | Grain size ($\mu$ m) | Comments | | | | | Reference |
|---|---|---|---|---|---|---|---|
| 25 | Single crystal | Shock direction | <100> | <110> | <111> | <123> | [26] |
| | | Twin fraction | <3% | <3% | <3% | <3% | |
| 55 | Single crystal | Shock direction | <100> | <110> | <111> | <123> | |
| | | Twin fraction | <3% | 25% | 6% | 5% | |
| 45 | 43 | Found twinning system <111>{112} | | | | | [27] |
| 15 & 45 | 50 | Found twinning system <111>{112}, omega phase transformation is also observed | | | | | [29] |
| 42 | 100 | Found twinning system <111>{112} | | | | | [40] |
| 30 | - | Found twinning system <111>{112}, omega phase transformation is also observed | | | | | [38] |
| 7 | - | No twinning is observed | | | | | [36] |
| 20 | - | Found twinning system <111>{112} | | | | | |
| 20-110 | Single crystal | Experiment obtain the slip-twin threshold pressure 32-43GPa | | | | | [37] |

Table 2.3: Twinning in shocked tantalum from the literature

$\sigma_G$ is the athermal component of the shear stress, which can be calculated from the Hall-Petch relationship. $C_1 - C_4$ are material constants, $\dot{\epsilon}$ is the strain rate and $\dot{\epsilon}_0$ is the reference strain rate.

A constitutive twinning nucleation model for body-centred cubic metals is shown in Figure 2.17. The dislocation pile-ups play a key role in providing the stress concentration for twinning nucleation. When the stress produced by the dislocation pile-up at the grain boundary exceeds the twinning stress, twin nucleation will occur. The twinning stress can be written as [27]:

$$\sigma_T = K\dot{\epsilon}^{\frac{1+m}{m}} exp[\frac{Q}{(m+1)RT}] \tag{2.7}$$

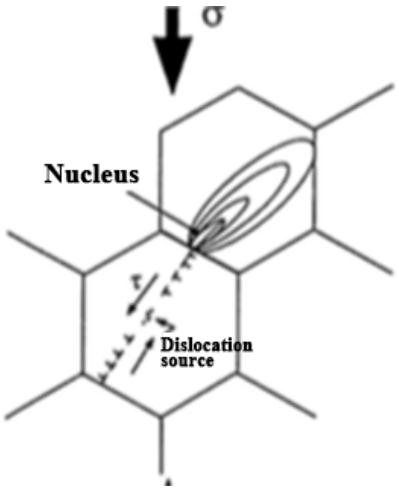


Figure 2.17: Twinning nucleation by dislocation pile-up [32]. The polycrystalline material is under a stress of $\sigma$. A dislocation source produces a dislocation pile-up across a grain with a stress $\tau$. The stress at the grain boundary exceeds the twinning stress and the twin is initiated.

$Q$ is the activation energy of dislocation slip, $T$ is the temperature, $m$ is a constant and:

$$K = M_T(\frac{nlE}{MA_0})^{\frac{m+1}{m}} \tag{2.8}$$

where $M_T$ is the orientation factor and $n$ is the number of piled-up dislocations. $l$ is the distance from the dislocation source to the boundary. $E$ is the elastic modulus. $M$ and $A_0$ are constants. The onset of twinning occurs at the stress where the slip stress equals the twinning stress, i.e. $\sigma_s = \sigma_T$. The stress on dislocations and twins is plotted in Figure 2.18 against shock pressure, showing that the range of critical pressures is from $35-70GPa$. However, twins are also found in specimens recovered from shock recovery experiments at stresses of $15GPa$ and $20GPa$. It is possible that

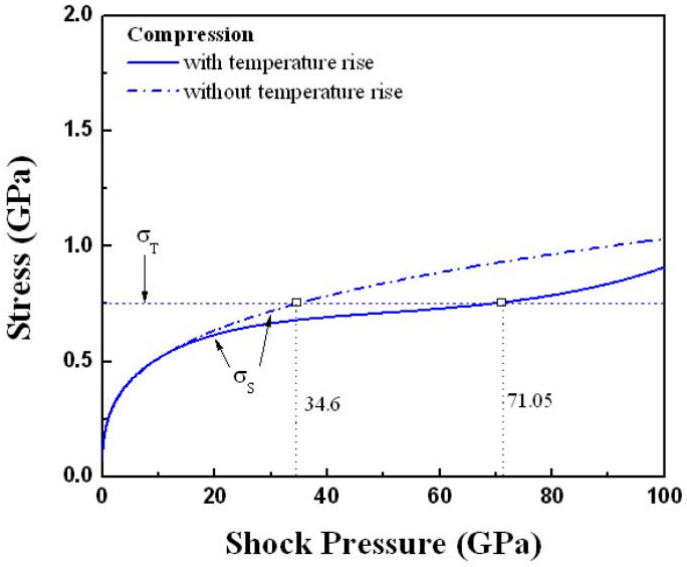


Figure 2.18: Slip and twinning stress as a function of shock pressure. The slip-twinning transition is in the range $35 - 70GPa$. [28].

twins are nucleated by the disturbance during the setup of the impact experiment, but the shear stress required for twinning and the mechanism of nucleation still need further investigation.

As a shear driven phenomenon, deformation twins can be strongly influenced by the shear stress during loading. It is reported that in $60GPa$ shocked tantalum, twins are preferentially created in the region with higher wave obliquity, where the shear stress can be significantly increased [41]. However, there is still a lack of knowledge of the effect of weak oblique waves, since they have the potential to influence the deformation mechanisms in the material (e.g. produce twinning at pressures lower than the usual threshold).

## 2.5 Objectives

Most previous studies on the deformation behaviour of tantalum in shock loading were focused on the effect of the shock wave front on the residual microstructure of the material. The release wave (either from the back surface of the projectile or the specimen) were considered to have a minor effect on the dislocation slip direction. This is because the loading direction of these release waves are the same as the shock wave and with lower strain rate. The lateral release wave has always been avoided in plate shock experiments and its significant effect on the plastic flow of material not fully understood.

The hardening behaviour of polycrystalline tantalum under shock loading and quasi-static deformation has been extensively studied. However, the orientation dependence of the dislocation substructure evolution under shock loading still needs investigation.

The objective of this project are therefore:

- To investigate the behaviour of twinning in tantalum single crystals under shock loading; the orientation dependence of the twinning behaviour; the influence of release waves on twinning nucleation/growth.

- To study the dislocation behaviour under shock wave loading, the influence of the loading direction and the release waves on dislocation substructure evolution.

# Chapter 3

# Electron channelling contrast imaging and its application of dislocation observation

## 3.1 Introduction

Electron channelling results from the interaction of high energy electrons with crystalline materials [42]. It can be used to examine the crystallography of a crystal in the SEM and to characterise the defects in the crystals. It has many advantages over transmission electron microscopy for the characterisation of crystal dislocations, e.g. easy sample preparation, large examination area, etc. However, it attracts less attention than TEM due to the relatively poor contrast, especially for heavy (high Z) materials. In this section, the shock induced dislocations in tantalum single crystals

are studied using electron channelling contrast (ECC). The dislocations in the same area of a TEM foil are imaged using both TEM and electron channelling contrast imaging (ECCI) to investigate the visibility of the dislocations. The influence of imaging conditions (diffraction deviation parameter, depth of dislocation) on the contrast of the dislocations is studied. The contrast profiles of dislocations are simulated using Matlab 2012b, based on the dynamic theory of electron diffraction and backscattering. The results are then compared and discussed with the experimental results. A methodology for dislocation density measurement in tantalum using ECCI is developed and discussed. This methodology is then used to measure the dislocation density distribution on the lateral section of the shocked tantalum single crystal.

## 3.2 Literature review

It is well known that all real crystalline materials have imperfections: point defects, line defects, surface or volume defects. A dislocation is a line defect. It provides a fundamental deformation mechanism for crystalline materials. The existence of these lines was deduced by inference in the early stages (1934 to the early 1950s), since when a wide range of observation techniques has been developed to image them. In 1953, Vogel and co-workers found a one-to-one correspondence of pits and dislocations on a etched crystal surface [43]. The dislocations could be revealed by chemical/electrolytic etching of a polished sample surface, producing small etch pits. In 1958, a decoration method was applied to a KCl crystal to make visible the

dislocations. By doping the material with impurity atoms, the dislocations were decorated with impurities and therefore revealed by visible light. The first observation of dislocations using a transmission electron microscope was made by Menter [44] in 1956. Using the high-resolution technique in TEM, Menter was able to image platinum phthalocyanine by direct resolution of the lattice planes and found dislocations spaced $1.2nm$ apart. In the same year, Hirsch and Whelan [45] imaged dislocations in an Al foil using diffraction contrast in the TEM. The Burgers vectors, distribution and interactions of dislocations were studied extensively in the 1950s and 1960s [46] [47] [45]. The tremendous advantages of TEM for dislocation observation (e.g. to determine Burgers vectors, in-situ tests, etc.) made it the major characterisation method for dislocations. However, the difficulties of sample preparation (electro-polishing, FIB slicing) make the TEM characterisation hard to perform. Also, the limited illumination area of a conventional TEM specimen (normally a few microns) makes it difficult to investigate the dislocation distribution over a large area. As an alternative to TEM, the backscattered electron image in an SEM has the advantage of easy sample preparation (electro-polish or mechanical polish and chemical etching). Also, a large area examination is allowed since it only depends on the size of the specimen chamber of the SEM. The mechanism of this imaging contrast using a backscattered electron detector is electron channelling. Electron channelling contrast imaging in SEM has been used as a characterisation method for dislocations for over twenty years. However, it received less attention than TEM since the resolution is not as high [42] [48]. The limited applications of ECCI have mostly been performed on relatively light materials like Ni, Al, Fe, semi-conductors, etc [49]

[50] [51]. The advantages of ECCI are to allow fast examination of a large amount of specimen, especially quantitative measurements of dislocation density. It has potential for industrial users or researchers who need a simple dislocation density study. The objective of this section is to optimise the imaging condition of ECCI on tantalum (a heavy material) through the simulation of dislocation contrast profiles under various imaging conditions and to confirm the result with experimental results. Thus a methodology for dislocation characterisation in tantalum in an SEM will be developed.

The possibility of observing crystal defects using ECCI was predicted in 1962 by Hirsch [52]. An early observation of electron channelling contrast in an SEM was reported by Coates in 1967 [53]. The rapid change of backscattered electron intensity near the Bragg condition was then explained by Hirsch and Humphreys as an electron channelling effect in 1970 [54]. As shown in Figure 3.1, in the ′rocking curve′ of the electron intensity against incident angle, the intensity drops rapidly near the Bragg condition and gradually increases with deviation from the Bragg condition. In 1972, Spencer developed a full description of the dynamic theory on the channelling contrast image of a crystal containing defects, predicting the visibility of dislocations in the backscattered electron image [48]. However, at that time the resolution of SEM was not high enough to see those dislocations. In the early years electron channelling contrast in an SEM was mainly used to determine the crystal orientation and to observe deformation of the materials [42].

In 1979, Morin made the first observation of dislocations by ECCI, using an SEM with a field emission gun [55]. Experimental results on silicon made by Czernuszka

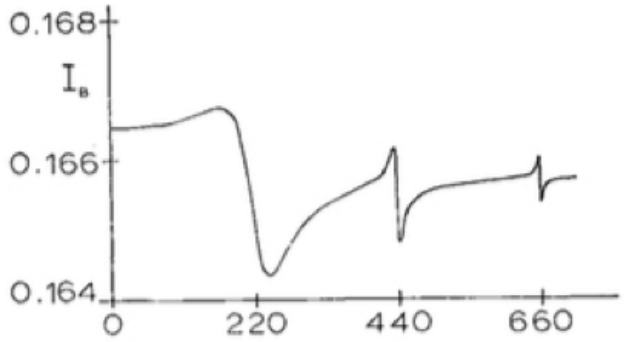


Figure 3.1: Theoretical BSE intensity profile across (220), (440) and (660) channelling pattern lines [54]. The y axis is the intensity of the backscattered electrons and the x axis is the angle of electron beam with respect to the Bragg condition with (220), (440) and (660) crystal plane.

in 1990 suggested that the $g \cdot b = 0$ invisibility criterion can be applied to screw dislocations [56]. Image simulations carried out by Wilkinson indicate that invisibility criteria hold for ECCI [57] [58]. The ECCI contrast was also predicted to be generated only generally within $5\xi_g$ ($\xi_g$ is the extinction distance) of the specimen surface [57]. This phenomenon was further confirmed by later experiment work [51] [59].

As a characterisation method similar to transmission electron microscopy (diffraction contrast), ECCI contrast was also sensitive to the deviation parameter. It was reported that the image contrast is optimised at the condition $s \approx 0$ [60], and changes rapidly when $s$ become negative [61]. Simulation work by Wilkinson [58] shows that the stress relaxation of a dislocation close to the crystal surface would only give minor effects on the electron channelling contrast image. Therefore in the numerical calculations of dislocation contrast profile, it is reasonable to use the

crystal displacement of a dislocation in an infinite medium.

ECCI has been used as a efficient tool for measuring dislocation density. Crimp [62] carried out an in-situ experiment on a titanium alloy. In his study, dislocation densities were measured by counting the dislocations in the image [62]. A different method was also employed by Gutierrez-Urrutia on iron. The probe depth $t$ calculated by Wilkinson [57] was used as the thickness of the materials and dislocation density was calculated using the relationship $\rho_D = 2N/Lt$, in which $N$ is the number of dislocation lines intersecting a grid of the total line length $L$ on the corresponding ECC image; $t$ is the thickness of the sample foil [63].

ECCI could be performed while a mechanical test is in progress to see the microstructure evolving. In-situ experiments using ECCI were carried out on NiAl single crystals [49] [62]. However, ECCI still has some limitations. Unlike TEM, ECCI of dislocations is only optimised with $s = 0$, and image contrast falls off rapidly with both positive and negative deviations from the perfect Bragg condition [60].

It should be mentioned that, in early studies, a high-tilt imaging configuration $(50° - 70°)$ was always used to increase the total number of BSEs with the assistance of a backscattered electron detector standing by the side of the specimen [55]. This was considered a good arrangement because it allows a large $'$tilt$'$ of the specimen, i.e. a large range of crystallographic directions can be reached simply by sample rotation, without changing the angle between specimen surface and detector. However, this setup requires a special modification of the microscope. Instead of using the regular $'$ring$'$ shape BSE detector, a rectangular BSE detector needs to be positioned by

the side of the tilted specimen. In the current study, the backscattered electron detector is fixed under the pole piece, which is a popular configuration of SEM for metallurgical use. This geometry will be investigated in the light of the previous tilt experiments.

## 3.3 Theory of electron channelling and dislocation imaging

In this section the formulae used in the simulation for electron channelling contrast image are reviewed. A method for calculating the Bloch wave function [64], backscattered electron intensity [48] in a crystal with dislocation and the column approximation [64] is introduced.

### 3.3.1 Column approximation

An image acquired by a scanning electron microscope (normally black/white) is formed by a matrix of many pixels. Each pixel has a value on a grey-scale, which represents the electron intensity received by the detector from the corresponding area on the specimen. The idea of simulating the backscattered electron image is to calculate the intensity of the electrons received by the backscattered electron detector when the area corresponding to every pixel (usually a few nanometres) is illuminated by the electron beam. Since the scattering angles for electron diffraction are very small, diffraction of electrons is essentially a forward scattering process. This means, even with the electrons being scattered several times in the crystal,

most of them will still travel nearly parallel to the incident electron beam. If we make an exaggerated assumption for the maximum scattering angle, say 1° after travelling 200 $nm$ into the crystal – the electron will move at most 3.5$nm$ away from the projection of the entrance point on the exit plane. This means that the electrons in this small column (with 3.5 $nm$ diameter, parallel to the incident beam) will not have any interaction with the electrons or matter of adjacent columns. Therefore, it is a good approximation to assume that the electrons will not leave this cylindrical column. For the purpose of numerical simulation it is more convenient to use rectangular columns (normally with $5 - 10\,nm$ width).

Consider an imaging area with dimension $X \times Y$ on the electron entrance surface of the sample. It can be subdivided into square elements with edge length 1. The total number of these elements is therefore:

$$n = \frac{X \times Y}{l^2} = \frac{X}{l} \times \frac{Y}{l} = N_x N_y \tag{3.1}$$

where $X/l$ and $Y/l$ are the numbers of squares in the $x$ and $y$ directions, respectively, on the sample area. In practice, the electron intensities from these $n$ elements need to be solved and rearranged into $N_x N_y$ pixels, which can be labelled with two integers $(i, j)$. In this way, we can calculate the backscattered electron image for the selected sample geometry. This assumption is called the column approximation.

### 3.3.2 Electron wave function in a faulted crystal

The wave function of the transmission/diffraction waves in a faulted crystal with a two beam condition can be calculated via a set of differential equations [64]:

$$\begin{aligned}\frac{d\psi_0}{dz} &= -\frac{\pi}{\xi_0'}\psi_0 + \pi(\frac{i}{\xi_g} - \frac{1}{\xi_g'})\psi_g \\ \frac{d\psi_g}{dz} &= \pi(\frac{i}{\xi_g} - \frac{1}{\xi_g'})\psi_0 + (-\frac{\pi}{\xi_0'} + 2\pi i(s + \frac{\alpha}{2\pi dz}))\psi_g\end{aligned} \tag{3.2}$$

$\psi^{(0)}$ and $\psi^{(g)}$ are the wave function of the transmission and diffraction wave.

$\underline{g}$ the lattice plane reciprocal vector.

$\alpha$ is the phase angle caused by the strain field, $\alpha = 2\pi\bar{g} \cdot \bar{b}$.

$\bar{b}$ is the Burgers vector of the dislocation.

$\underline{R}$ is the displacement vector of the crystal lattice caused by the defect.

${\xi_g}'$ and ${\xi_0}'$ are the absorption coefficients of the material; normally ${\xi_g}' = {\xi_0}' = 10\xi_g$.

$\xi_g$ is the extinction distance.

$s$ is the deviation parameter $s = w/\xi_g$.

$z$ is the travelling depth of the wave inside the material.

The backscattered electron intensity is directly related to the Bloch wave intensity in the material. Therefore the transmitted/diffracted wave amplitudes need to be transformed to the Bloch waves, according to Equation 3.3 [64].

$$\begin{pmatrix}\psi_0(z) \\ \psi_g(z)\end{pmatrix} = \begin{pmatrix}C_0^{(1)} & C_0^{(2)} \\ C_g^{(1)} & C_g^{(2)}\end{pmatrix} \begin{pmatrix}exp(2\pi i\gamma^{(1)}z) & 0 \\ 0 & exp(2\pi i\gamma^{(2)}z)\end{pmatrix} \begin{pmatrix}\psi^{(1)} \\ \psi^{(2)}\end{pmatrix} \tag{3.3}$$

The Bloch waves amplitude are then:

$$\begin{pmatrix}\psi^{(1)}\\ \psi^{(2)}\end{pmatrix} = E^{-1}C^{-1}\begin{pmatrix}\psi_0(z)\\ \psi_g(z)\end{pmatrix} \tag{3.4}$$

where $E$ and $C$ represent the matrix with the exponential terms and the diffraction coefficients Cs, respectively.

For the problem of calculating the wave amplitude in a crystal with a simple planar defect, like a stacking fault, the function can be analytically solved by adding the term for crystal displacement. For the image of a dislocation with a continuous strain field, the differential equation for the wave amplitudes needs to be solved numerically along the wave propagation path using a computer programme.

### 3.3.3 Electron backscattered intensity

The intensity of the backscattered electrons (with scattering angle higher than 90°) leaving the entrance surface ($I_B(0)$) is a function of the Bloch waves.

$$I_B(0) = \sum_j I_B^{(j)}(0) = \frac{1}{1+p't}[p't + \sum_j (p^{(j)} - p') \int_0^z I^{(j)}(z)dz] \tag{3.5}$$

$I_B^{(j)}(z)$ is the backscattered electron intensity of the $j$th Bloch wave at a depth z in the material.

$p'$ is the fraction of intensity backscattered from the forward/backscattered wave.

$p^{(j)}$ is the fraction of intensity backscattered from the Bloch wave $j$.

# Chapter 4

# Experimental procedure

## 4.1 Shock loading experiment and modelling

The shock loading experiments were performed by Atomic Weapons Establishment (AWE), UK. Tantalum single crystal ($> 99.99\%$) discs with [111], [011] and [001] sample normal directions were subjected to plate impact. The flyer plate was accelerated by a single stage gas gun to a velocity of $200m\,s^{-1}$. The gas gun is shown in Figure 4.1. The thickness of the projectile is $3mm$. The samples have $12mm$ diameter and $4mm$ thickness. The specimen configuration is shown in Figure 4.2. The surface appearing in the picture is the surface impacted by the projectile. The outer ring is the fixture for installing the specimens onto the shock loading chamber. The three single crystals mounted in the epoxy are labelled as [111], [011] and [001]. The big disc on the bottom is a tantalum polycrystalline specimen. The momentum trap and spall plates in Figure 2.8 were not used in the current setup. The velocity of the

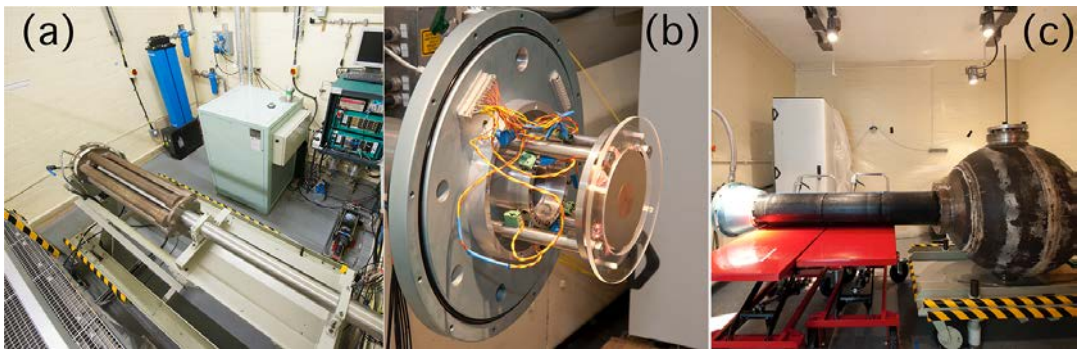


Figure 4.1: Single stage gas gun for plate shock experiment. (a) projectile acceleration component; (b) specimen fixture; (c) recovery chamber

centre area of the back surface of every disc was measured by the HetV system. The three single crystals were recovered from the chamber for microscopic investigation. Finite element hydrocode simulations (using ANSYS Autodyn software) for pressure and shear stress of a polycrystalline tantalum disc with the same dimensions as the single crystals under the same loading condition were provided by AWE, to give an indication of the wave propagation inside the material.

## 4.2 Scanning electron microscope

A sketch of the recovered tantalum single crystals is shown in Figure 4.3. To study the influence of the shock and release waves, the lateral surface of the specimens need to be revealed. The single crystal discs were cut in half along the shock loading axis from the centre. The cutting plane for sample [111] was $(2\bar{1}\bar{1})$, for sample [011] was $(1\bar{1}1)$ and for sample [001] was (110). The lateral surfaces of part A of all the samples were ground using ′wet and dry′ SiC paper from grit 400 to grit 4000.

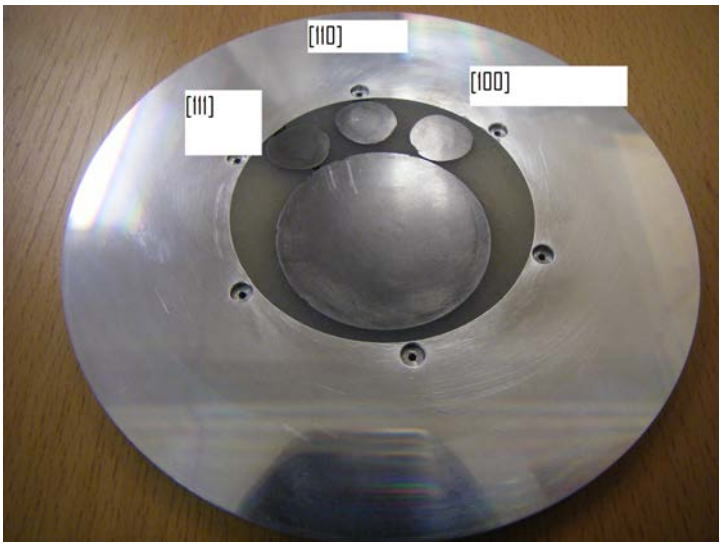


Figure 4.2: Configuration of the fixture for the tantalum specimens. The outer ring is the plate used to fix the specimens to into the chamber of the gas gun. The samples are mounted in epoxy. The three small discs are the single crystals. The big disc is polycrystalline tantalum.

Then they were subjected to polishing with OP-S polishing suspensions (Struers) for 1 hour. The polished surfaces were then characterised using a backscattered electron detector in a Tescan Mira3 XM scanning electron microscopy, working at $30kV$ voltage. The dislocation density distribution in the specimen was measured using the electron channelling contrast imaging (ECCI) technique, which is discussed in section 3. The twinning produced by shock and release waves were identified by electron backscattered diffraction (EBSD) in a JEOL 7000F scanning electron microscope.

Because the backscattered electron signal is very sensitive to the orientation of the crystal, the twinning inside the material produced by the shock loading and release is very clear on the BSE image. In a single crystal, the boundary of twins with the same type will show their trace in the BSE image. The twin images were filtered out using a script in ImageJ to show the twinning distribution in the sample lateral surface.

Electron channelling contrast image performed by the Tescan Mira3 XM SEM is used to measure the distribution of dislocation densities in the single crystals. The methodology and configuration of the SEM is discussed in detail in Chapter 3.

## 4.3 Transmission electron microscope

### 4.3.1 Sample preparation

Part B of the specimens in Figure 4.3 was used to prepare the TEM sample for dislocation microstructure analysis. The cutting method is shown in Figure 4.4.

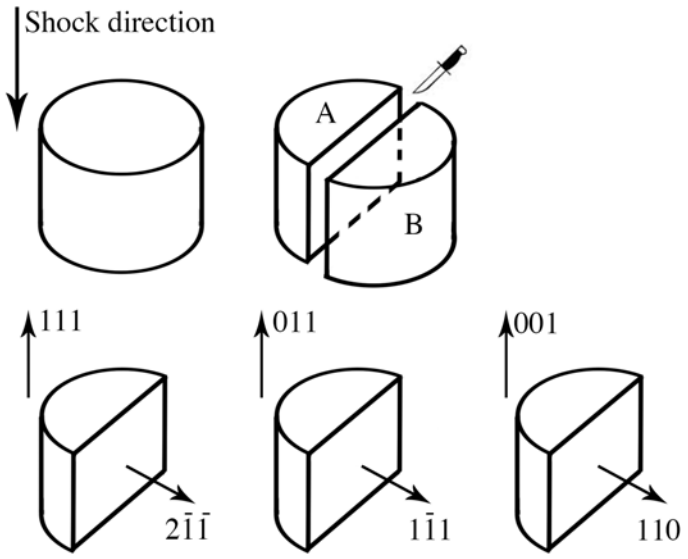


Figure 4.3: A sketch of the cutting of the shocked tantalum single crystals. The tantalum discs were cut along the shock loading direction into A and B. The A pieces were used for the SEM characterisation. The sample normal of the SEM specimens are labelled in the bottom row graphs.

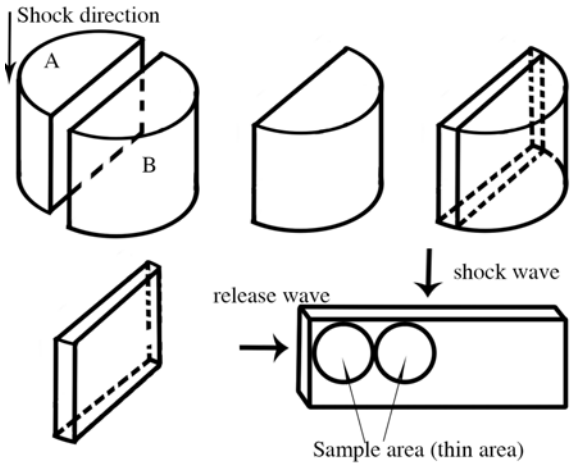


Figure 4.4: A sketch of the cutting of the TEM foil for shocked tantalum single crystals. A plate was cut along the shock loading direction from the part B of every sample. 3 $mm$ discs were pouched from the plates as indicated in the bottom right graph.

The TEM area in Figure 4.4 was then thinned by electropolishing in an electrolyte of 4% hydrofluoric acid, 20% sulphuric acid and 76% methanol at $-25 \sim -30°C$ using a voltage of $25VD.C.$

### 4.3.2 TEM observations

TEM observations were carried out on a JEOL 2100 operating at $200kV$. The defect analysis techniques: Burgers vector analysis and trace analysis of directions were performed according to the description by Loretto and Smallman [65]. The dislocations were imaged by TEM bright field imaging in a two beam condition. The twins in the sample were analysed via selected area diffraction patterns (SADP's).

## 4.4 Electron channelling contrast imaging

### 4.4.1 Numerical simulation of dislocation contrast profile in ECCI

In the transmission electron microscope, a two-beam condition is normally used to characterise crystal defects [64]. For the dislocation contrast in the backscattered electron image in an SEM, a two-beam condition can still be employed to optimise the contrast of the dislocation. Therefore, only two Bloch waves will be considered: $\psi^{(1)}$ and $\psi^{(2)}$. The intensities of these two waves $I^{(1)}$ and $I^{(2)}$ are:

$$I^{(1)} = \psi^{(1)} \cdot \psi^{(1)\star} I^{(2)} = \psi^{(2)} \cdot \psi^{(2)\star} \tag{4.1}$$

Consider a screw dislocation located at $(x, y)$ in a semi-infinite material (Figure 4.5). The dislocation line direction and Burgers vector are normal to the paper (the strain field is shown as a colour map). An array of small columns with $5nm$ width was defined across the dislocation for over $50nm$. The small slabs in the columns with height dz are perfect but with displacement $R$ from the original position. Wilkinson [58] indicates that a dislocation in an infinite medium can be assumed with minor influence on the dislocation contrast profile (i.e. no image dislocation is necessary). According to the elastic model of the dislocation strain field [66] $R$ is related to the position of slab, thus:

$$R = \frac{\underline{b}}{2\pi} tan^{-1} \frac{y - Y}{x - X} \tag{4.2}$$

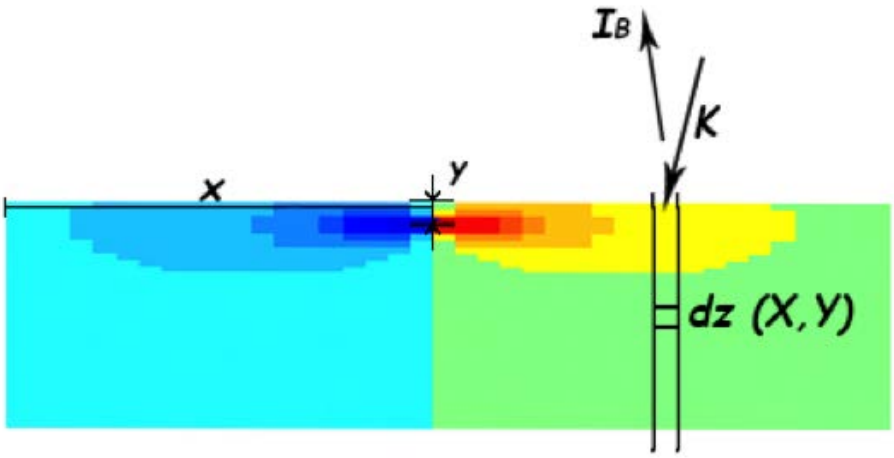


Figure 4.5: The material for ECCI profile simulation. A dislocation is located at depth y of a semi-infinite crystal. The strain field of the dislocation is represent as a colour map. A column of the material is picked out on the right side of the map. The location of a small element $dz$ in the column is (X,Y).

Then the amplitude of the electron in the material can be calculated using the differential Equations 3.2. The intensity of the backscattered electrons leaving the crystal surface of each column can be determined since it is directly related to the amplitude of each Bloch wave by Equation 3.5. The equations used in the simulation can be summarised as:

$$\begin{aligned}
\frac{d\psi_0}{dz} &= -\frac{\pi}{\xi_0'}\psi_0 + \pi(\frac{i}{\xi_g} - \frac{1}{\xi_g'})\psi_g \\
\frac{d\psi_g}{dz} &= \pi(\frac{i}{\xi_g} - \frac{1}{\xi_g'})\psi_0 + (-\frac{\pi}{\xi_0'} + 2\pi i(s + \frac{\alpha}{2\pi dt}))\psi_g \\
\begin{pmatrix}\psi^{(1)} \\ \psi^{(2)}\end{pmatrix} &= E^{-1}C^{-1}\begin{pmatrix}\psi_0(z) \\ \psi_g(z)\end{pmatrix} \\
I_B(0) &= \sum_j I_B^{(j)}(0) = \frac{1}{1+p't}[p't + \sum_j (p^{(j)} - p')\int_0^z I^{(j)}(z)dz]
\end{aligned} \tag{4.3}$$

The intensities of the backscattered electrons exiting the sample surface from all the columns were calculated and plotted against the y axis to give the dislocation profile. The various parameters used in the simulation are shown in Table 4.1. In the examination of the deviation parameter effect, the depth of dislocation beneath the crystal surface was fixed to be $0.2\xi_g$. In the test for the effect of dislocation depth, the deviation parameter is 0.

Table 4.1: The parameters for the ECCI simulation

| Dislocation depth 0.2 $\xi_g$ | a | b | c | d |
|---|---|---|---|---|
| Deviation parameter w | 0 | 0.1 | 0.3 | 0.9 |

| Deviation parameter w=0 | a | b | c | d |
|---|---|---|---|---|
| Dislocation depth | 0 | $0.1\xi_g$ | $0.3\xi_g$ | $0.9\xi_g$ |

### 4.4.2 Sample preparation

A single crystal tantalum disc with $< 111 >$ sample normal was subjected to a plate impact experiment at a peak pressure of $6GPa$. The sample had $12mm$ diameter and $4mm$ thickness. It was shock loaded by a $3mm$ thick tantalum projectile. A $1mm$ slice was taken from the front surface of the specimen using a spark erosion machine. A $3mm$ TEM disc was punched from the central area of the slice. This disc was then electro-polished in a solution with 5% HF, 95% methanol (volume percentage solution) at $-10$°C and $25V$ voltage [27].

Another sample with the same loading condition was cut transversely through the centre of the disc. The lateral surface of the specimen was polished using a standard polishing procedure and then slightly etched using 20% HF + 80% water for 10 seconds [27].

### 4.4.3 Transmission electron microscopy

A JEOL 2100 transmission electron microscope working at $200KV$ was employed to characterise the shock induced dislocations in the $3mm$ tantalum disc. In the thin area, the dislocations were imaged using two beam conditions. The Burgers vectors of the dislocations were determined using the $g \cdot b = 0$ extinction criterion the direction of the dislocation line was determined using tilting experiments in the TEM.

### 4.4.4 Imaging configuration in scanning electron microscope

The electron channelling contrast image was acquired from both the $3mm$ TEM foil and the polished sample lateral surface using a Tescan scanning electron microscope with a field emission gun. The imaging assembly is shown in Figure 4.6. To maximise the signal received by the backscattered electron detector, the sample was brought to a position very close to the pole piece ($5mm$ working distance). This means that the distance from the sample surface to the detector is about $3mm$, and a $\pm 5^{\circ}$ tilt is allowed. The sample was tilted slightly to set the crystal at a two beam condition. The area on the $3mm$ disc imaged by TEM was imaged in the SEM using electron channelling contrast. The images were stitched together and compared with the TEM image.

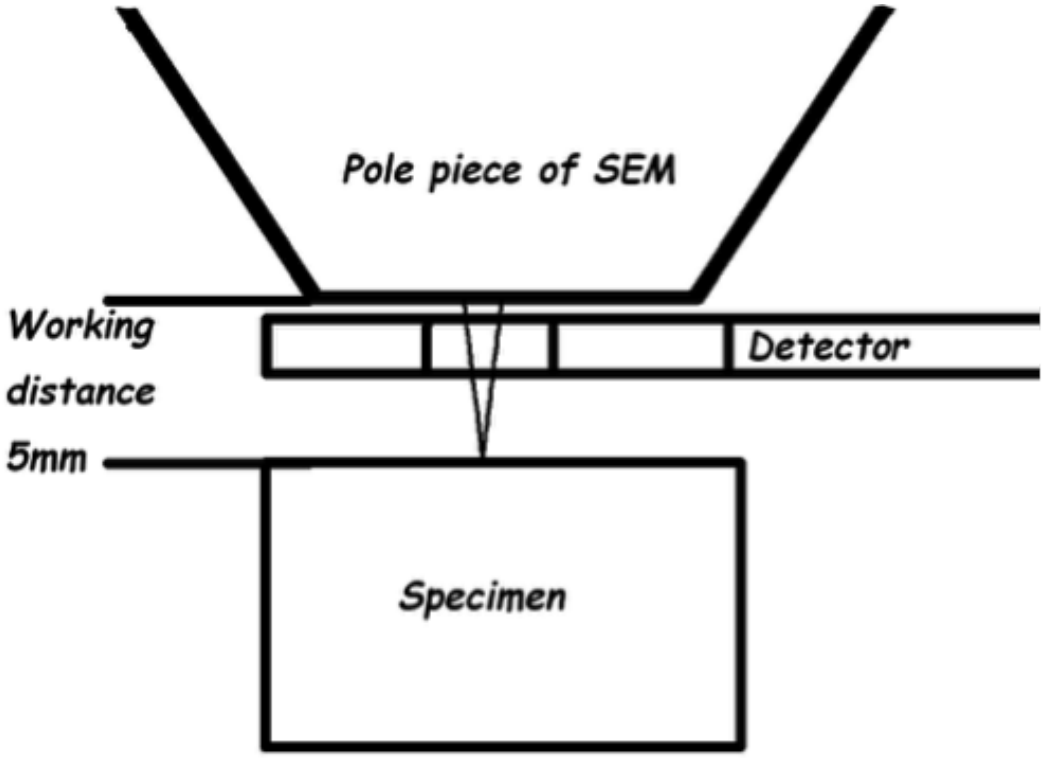


Figure 4.6: The imaging configuration for the tantalum single crystals

The same imaging condition was then applied to the bulk specimen to measure the dislocation density distribution induced by the shock compression. The sampling points formed a matrix across the specimen surface as shown in Figure 4.7.

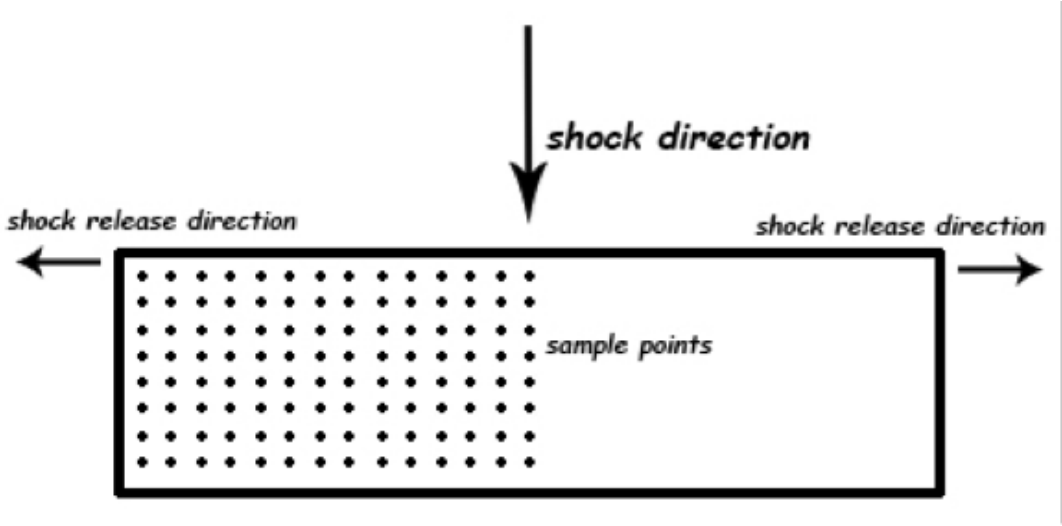


Figure 4.7: The sampling points for the dislocation density distribution measurement. The shock wave enters the material from the top; the strained crystal is then released from the lateral directions

# Chapter 5

# Results

## 5.1 Wave propagation through the specimen

The free surface velocity profile measured at the centre of the back surface of the specimens by the HetV is shown as a function of the time in Figure 5.1. The shock wave front arrives at the back surface at time 111 $\mu s$, appear as the velocity raise dramatically to around $100 m\, s^{-1}$. According to equation 2.5 the shock pressure $P$ is square proportional to the free surface velocity (which is $2v_p$), the rise of the free surface velocity in Figure 5.1 can be seen as the rise of shock loading pressure. The velocity rises rapidly to the HEL. The single crystal [001] has the highest Hugoniot elastic limit, with a free surface velocity of $126\, m\, s^{-1}$. The free surface velocities of the HEL of [011], [111] and polycrystalline specimens are $82\, m\, s^{-1}$, $120\, m\, s^{-1}$ and $75\, m\, s^{-1}$, respectively.

After yielding, the free surface velocities show a significant drop and then rise

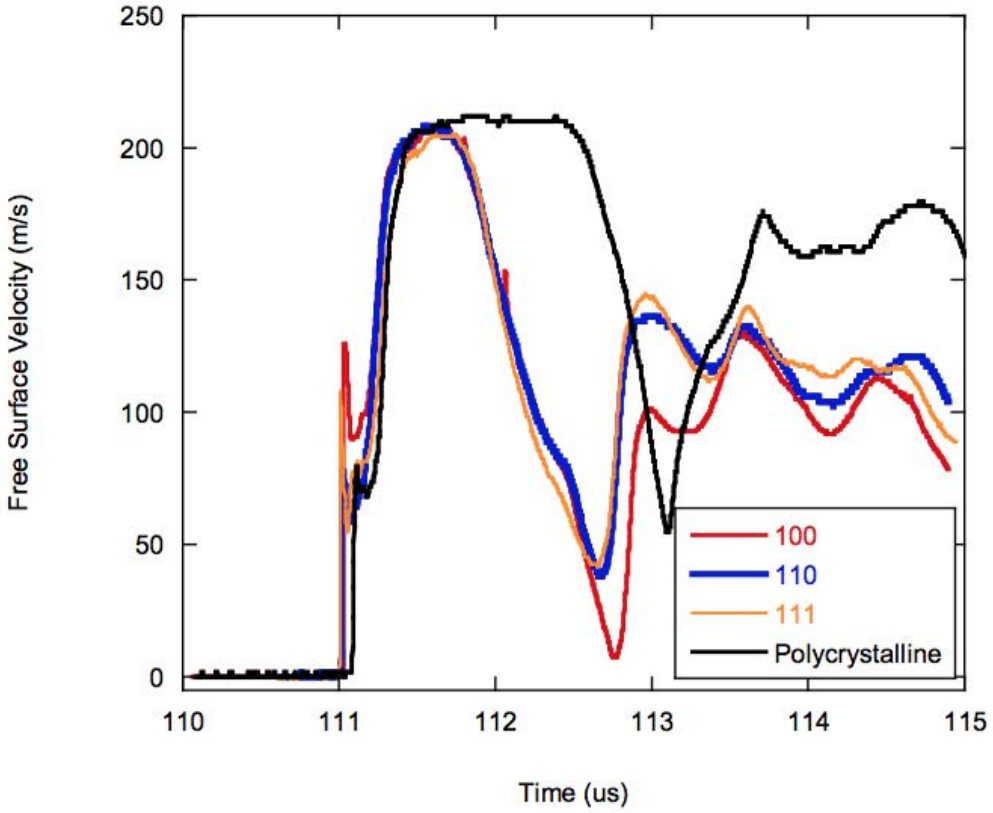


Figure 5.1: Free surface velocities of the centre of the specimen back surfaces as determined by HetV. See text for detailed explanation.

to 212 $m\ s^{-1}$ at time 111.5 $\mu s$. The pressure holds for about 0.5 $\mu s$, and then the velocity of the single crystals starts to drop to around 50 $m\ s^{-1}$. The velocity of the back surface of the polycrystalline specimen holds at 210 $m\ s^{-1}$ for around 1.9 $\mu s$ before it starts to drop. The velocities then oscillate between 50 $m\,s^{-1}$ and 170 $m\,s^{-1}$ for the next few microseconds.

## 5.2 Twinning

### 5.2.1 Identification of twinning

Backscattered electron (BSE) SEM images of twinning in the shocked single crystals are shown in Figure 5.2. The images in the first row are taken from the shocked front surface. The images in the second row are taken from the lateral surface, cut through the transverse section) of the sample as shown in Figure 4.3. These images are taken with the beam direction very close to a low index zone axis (parallel to the specimen normal), which leads to strong diffraction of the electron beam and a dark background intensity. The background intensity changes gradually across the image. This suggests that the crystal has some residual strain induced by the shock deformation. The samples are filled with long thin twins. Most of the twins in the images show a brighter intensity than the background. The thickness of each twin is typically a few microns. In the front surface of the [111] and [001] specimens, the typical length twin is $50 - 100\mu m$. The twins in the [011] and [111] side surfaces and the [011] front surface are mostly longer than $150\mu m$. The twinning boundaries in all the images are perfectly straight except in images $(a)$ and $(b)$. The twins in the front surface of [111] and [011] are generally straight, but locally squiggly with very strong local strain.

A stereographic projection was employed to identify the twinning planes. This method is shown in Figure 5.3. The stereographic projection in Figure 5.3(b) projects the plane A in Figure 5.3(a) onto the plane $z = 0$, which is the sample surface. The line OB (connection line between zero point and the projection point

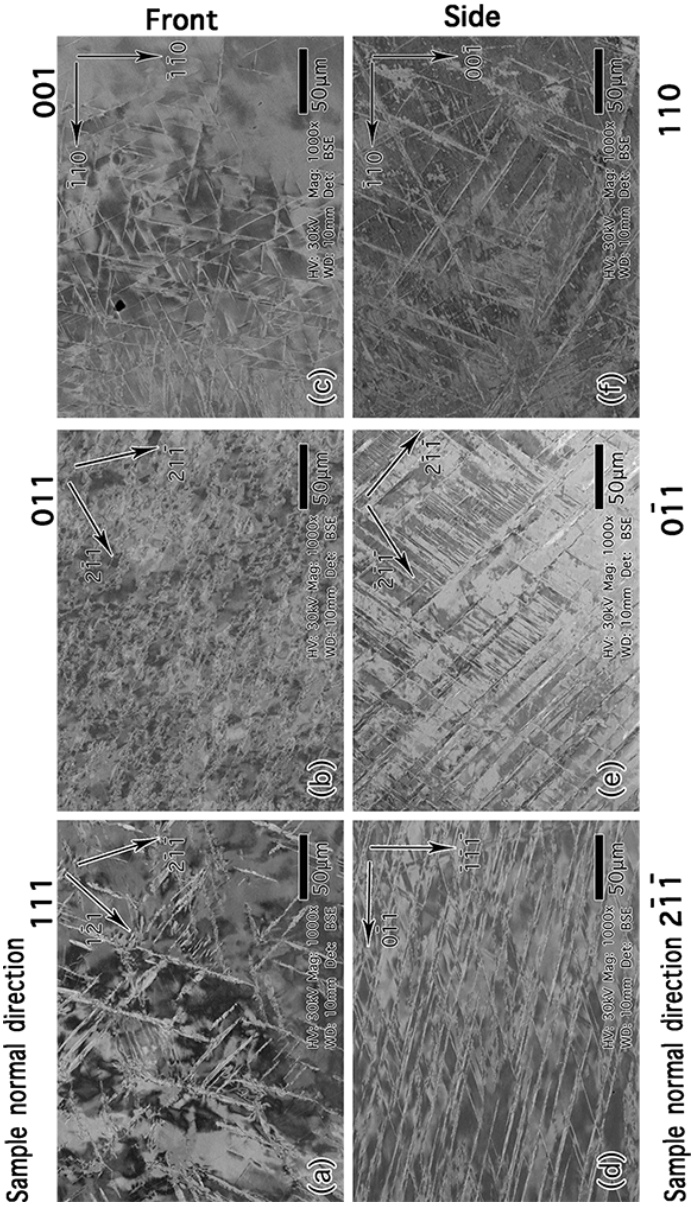


Figure 5.2: SEM BSE micrographs of tantalum single crystals. (a) Front surface of [111]; (b) Front surface of [011]; (c) Front surface of [001]; (d) Side surface of [111] (section $(2\bar{1}\bar{1})$); (e) Side surface of [011] (section $0\bar{1}1$); (f) Side surface of [001] (section (110))

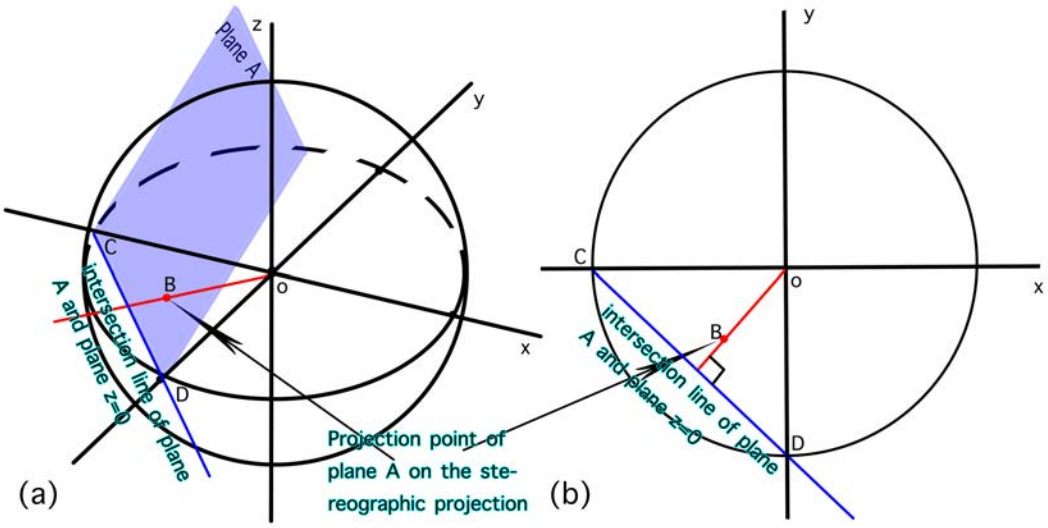


Figure 5.3: The relationship between the intersection line of plane A with plane $z = 0$ and the projection point of the plane A in a stereographic projection. The point B in the stereographic projection in (b) is the projection point of plane A on the $z = 0$ plane in (a). The line OB is perpendicular to the intersection line of plane A and $z = 0$ (CD).

of plane A) should be perpendicular to the line CD (intersection line of the plane A and the plane $z = 0$). The projection point of the plane A should be on the line which passes through the zero point and be perpendicular to the intersection line CD. Using this mechanism, the twinning planes can be identified.

The identification of the twins in the [111] specimen is shown in Figure 5.4. The micrograph in the top row shows a typical twinning microstructure of the front surface of specimen [111]. The twins are lying in three different directions with 60° intersection angles. These directions are parallel to the intersection lines of the twinning plane and the sample surface ((111)). The projection points of the {112} planes are sketched on the right side of the micrograph. A line (blue) is drawn

through the centre point of the stereographic projection and perpendicular to a twinning direction (twin A). It can be seen that this blue line passes through two {112} projection points: (211) and $(2\bar{1}\bar{1})$. This means that the twins with mirror planes (211) and $(2\bar{1}\bar{1})$ will appear in the same direction as the twin A in the image taken from the (111) top surface, i.e. the twinning plane of A is either (211) or $(2\bar{1}\bar{1})$. Similarly, the probable twinning planes of the twin B are (112) or $(\bar{1}\bar{1}2)$. For the twin C they are (121) or $(1\bar{2}1)$. After examining the whole surface, the twins have only these three directions on the sample [111] front surface.

The sample was then cut in half (as shown in Figure 4.3) to look at the twinning from the $[2\bar{1}\bar{1}]$ beam direction. The micrograph in Figure 5.4 shows the direction of the three types of twins from the side view. By comparing the micrograph with the stereographic projection, the twinning line directions (the cross section line of the twin plane with the sample surface) match with (112), (211) and (121) plane on the stereographic projection. The mirror planes of these twins are confirmed to be (112), (211) and (121).

The image of the twins in the [011] specimen is shown in Figure 5.5. Most twins at the front surface only lie on the direction. The potential twinning types are $(\bar{2}11)$ and (211). The side view image (Figure 5.5(b)) shows that these two types of twin both exist in the specimen.

From Figure 5.2($c$) and ($f$), there are many twinning systems activated in the sample [001]. The stereographic method is no longer useful here because multiple types of twins with different mirror planes appear in the same directions in the image. Electron backscattered diffraction (EBSD) is used to identify the twins in

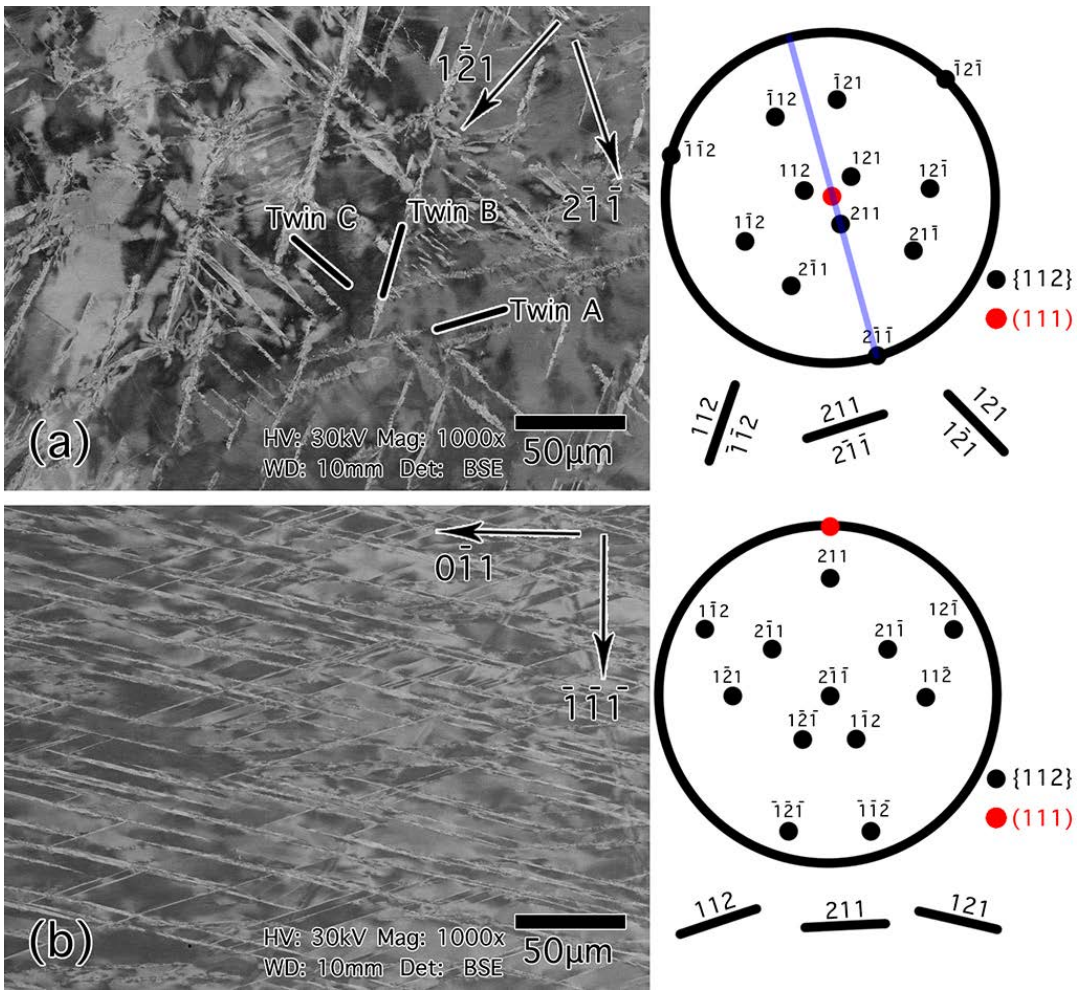


Figure 5.4: Identification of twins in sample [111]. (*a*) sample front surface; (*b*) sample side surface. The stereographic projection shows the sample normal orientation and the orientation of al the {112} twinning planes.

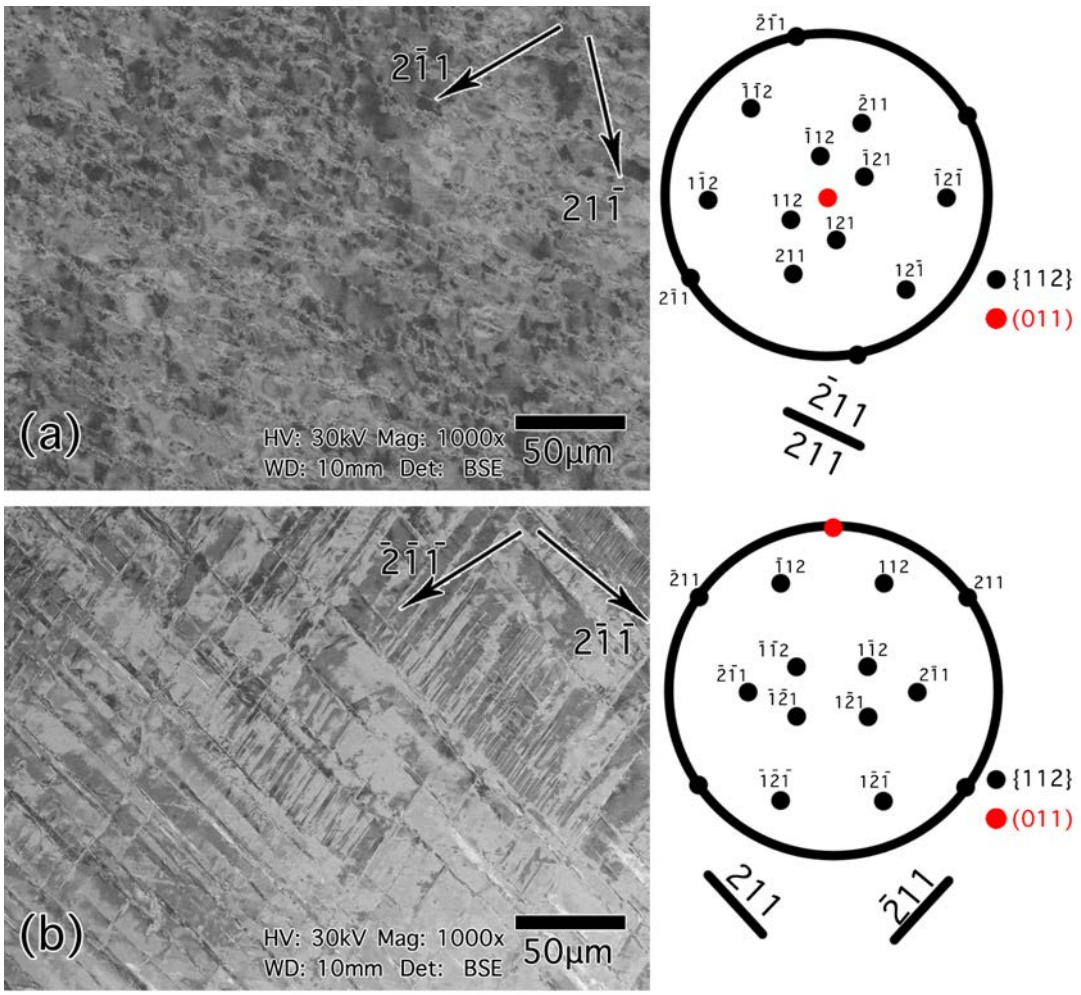


Figure 5.5: Identification of twins in sample [011]. ($a$) sample front surface; ($b$) sample side surface. The stereographic projection shows the sample normal orientation and the orientation of al the {112} twinning planes.

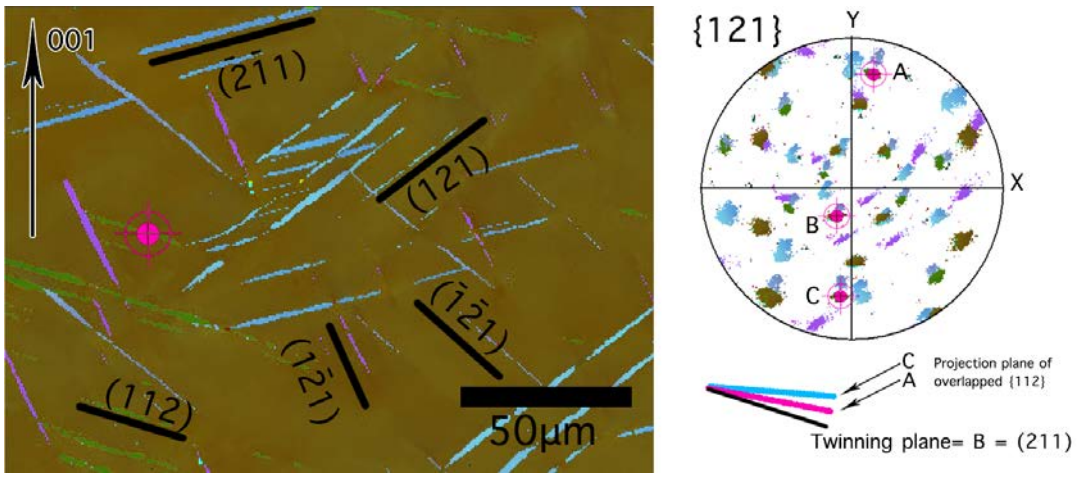


Figure 5.6: EBSD analysis of the twinning plane in sample [001]. There are five types of twinning in the area of the image: twin plane ($\bar{2}\bar{1}1$), (121), ($\bar{1}\bar{2}1$), ($1\bar{2}1$) and (112).

this sample. The EBSD analysis is shown in Figure 5.6. The twinning with the light green colour are picked to show an example of the analysis (labelled as red circle). There are three {112} planes of the twinning is overlapping with the {112} plane of the matrix: A, B and C. The intersection line of them and the sample surface are shown to the right bottom of Figure 5.6. Only the cross section line of plane B is totally parallel to the twinning line direction. This plane B corresponds to the plane (211) of the matrix. Therefore the plane of the light green twin is (211). After scanning through the front and side surface the twins in the sample [001] have planes (121), (211), (2$\bar{1}$1), (1$\bar{2}$1), ($\bar{1}\bar{2}$1), ($\bar{2}\bar{1}$1), ($\bar{2}$11) and ($\bar{1}$21).

### 5.2.2 Processing of twinning micrograph

To measure the distribution of the different twin across the whole specimen, the twinning in the SEM images must be picked out from the image background. Because the shock loaded specimens are single crystals, the twinning with a same type of twin plane in one sample will have the same direction in the SEM images. This makes it very easy to filter out the twins from the SEM images using a computer programme. The method of filtering is shown in Figure 5.7. The original SEM image is processed using the Fast-Fourier-Transform (FFT) function in the ImageJ software. Figure 5.7(b) is the resulting FFT. In this FFT, the contrast change across the twin boundaries in the original image has transformed into two bright lines which are perpendicular to the two types of twin. A mask is applied to one of the bright lines, to select the particular twin. Then the resulting image was inverse-FFTed. A particle analysis function in ImageJ was applied to remove the noise points. The resulting image is shown in Figure 5.7(d). The black lines in the filtered image fitted well with the twins in the original image.

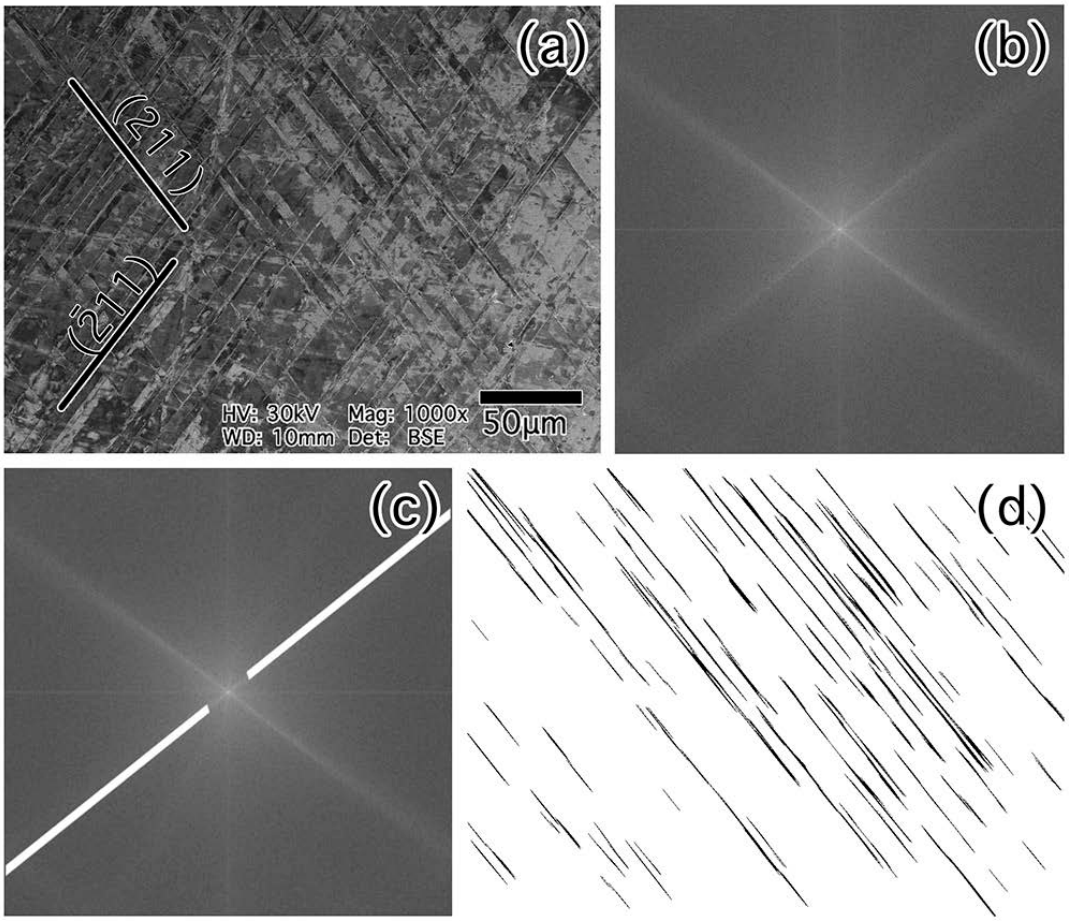


Figure 5.7: Filtering the (211) twinning in the tantalum [011] specimen. (*a*) original SEM image; (*b*) Fast-fourier transform (FFT) of the SEM image; (*c*) Filter mask on the FFT; (d) The resulting image after inverse-FTT and applied particle analysis in ImageJ

### 5.2.3 Distribution of twinning

#### Sample with [001] loading direction

The filtered twin micrographs were stitched together to show the distribution of twins across the sample. Figure 5.8 shows all the twins in the front surface of the [001] specimen. Only half of the sample is shown in the image because the distribution of the twins is symmetrical around the horizontal line. The twins are very dense within $1mm$ of the edge of the specimen. The density gradually decreases from the edge to the centre of the sample.

The stitched image of the [001] sample taken from the side with a beam direction $[\bar{1}\bar{1}0]$ is shown in Figure 5.9. Only the left half of the specimen is shown in this image. The structure is symmetrical around the centre axis. The shock wave impacted the upper side of the sample. The upper right side of the material popped out about $0.3\,mm$ from the original sample. There are some black dots on the left side of the image about $1\,mm$ from the sample front surface. These are voids which have a typical diameter of about $0.2\,mm$. They form into a cluster which has a length of $3\,mm$ (of which $1.5\,mm$ appears in the image). The image contrast of the voids is very significant due to their morphology. The FFT filtering method picks out the strong contrast in the image along the twinning boundary direction and therefore the voids appear in the filtered image.

In the region very close to the sample front surface (about $0.1\,mm$), the twinning density is very low. The area $0.1\,mm$ to $1\,mm$ away from the sample front surface is full of very dense and mixed types of twins. Then the number of twins gradually reduces and in the region $0.5mm$ from the back surface of the specimen, the twinning

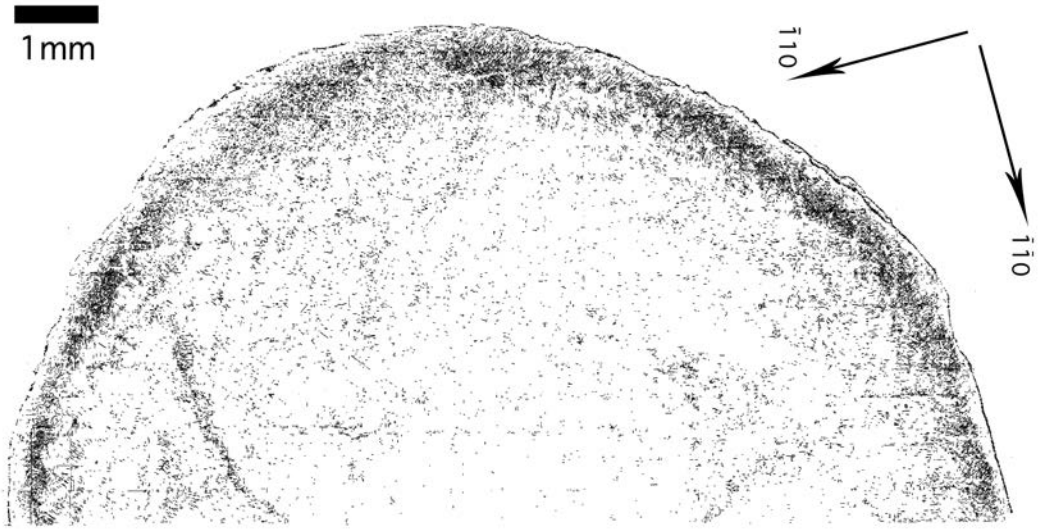


Figure 5.8: The distribution of twins on the front surface of sample [001]. Only half of the disc is shown in the figure since the distribution is symmetrical along the central line. The black lines in the graph are the twins. The twinning density is high at the edge and low at the centre.

density is almost zero. In the middle layer of the specimen ($1-3.5mm$), the twinning density varies from the sample centre to the edge. Close to the specimen centre ($0 - 2.5\,mm$) the twinning type is mixed and the density is high. The twins near the edge are long, straight and of one type.

The $(\bar{1}\bar{2}1)$, $(1\bar{2}1)$ and (211) twins were filtered out to examine their distribution. The results are shown in Figure 5.11. The density of the $(\bar{1}\bar{2}1)$ and (211) twins is higher at the specimen centre than at the edge. Their density is also high close to the shock interface, decreasing with distance and disappearing at the back surface. The $(1\bar{2}1)$ twin density is strongly related to location in the specimen. It is high on the left side but zero on the right side of the sample. The twins appearing on the right side of Figure 5.9 all have the twinning plane $(1\bar{2}\bar{1})$, which has an opposite distribution to the $(1\bar{2}1)$ twins. They are very dense on the right side and have a low density on the left side. The voids cluster induced by the loading in the sample [001] is shown in Figure 5.10. The total length of the cluster is around $4\,mm$ and the height is around $1\,mm$. The voids generally has circular shape.

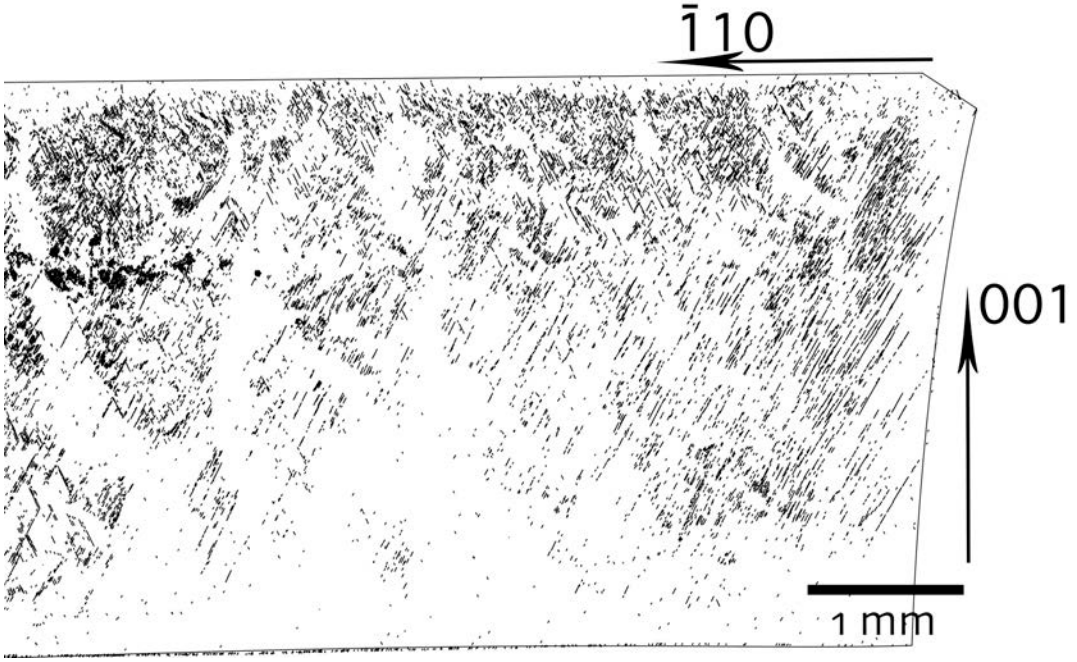


Figure 5.9: The distribution of twins on the side of sample [001]. Only half of the sample is shown in the figure since the distribution is symmetrical along the central line. The black lines in the graph are the twins. See text for detailed description.

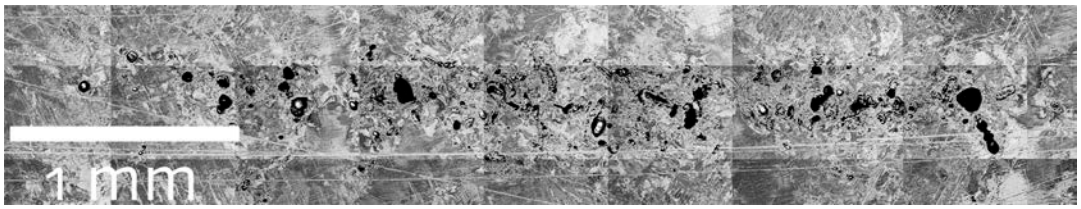


Figure 5.10: The void clusters in the 001 specimen. The total length of the cluster is around 4 $mm$ and the height is around 1 $mm$. The voids generally has circular shape.

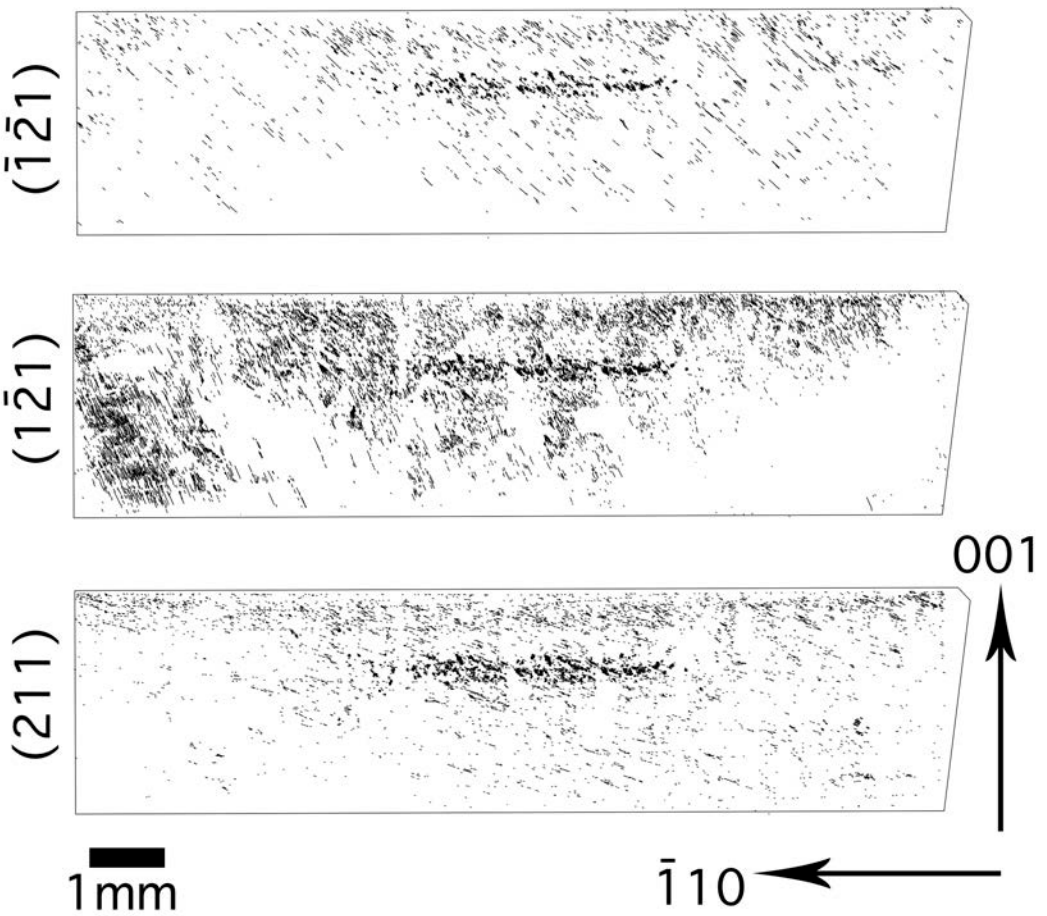


Figure 5.11: Distribution of $(\bar{1}\bar{2}1)$, $(1\bar{2}1)$ and (211) twins in the [001] specimen. The black lines in the graph are the twins. See text for detailed description.

### Sample with [011] loading direction

The twinning microstructure of the [011] sample front surface is shown in Figure 5.12. The density of twinning here is high and evenly distributed across the front surface. The horizontal and vertical straight lines on the image come from the stitching of multiple images.

The filtered image from the side surface of the [011] sample is shown in Figure 5.13. The voids are elongated and oriented in the same directions as the twinning. The void cluster is thicker and longer than in the [001] sample, about $0.5\,mm$ thick vs $6\,mm$ long (of which $3\,mm$ appears in the image). The twins in this specimen are very long. Some of them even cross the whole disc. The density of the twins is high at the front surface and decreases with depth.

There are only two types of twins in the sample with a [011] shock loading direction. They are filtered out and shown in Figure 5.15. It can be seen that the $\bar{2}11$ twins are popular on the right side and the 211 twins on the left.

### Sample with [111] loading direction

Figure 5.16 is a stitched and filtered image of all the twins intersecting the [111] sample front surface. Like the [011] sample, the twins on the [111] front surface are evenly distributed. In the region within $0.5\,mm$ of the edge, the image does not show much twinning because the material has very heavy residual strain here. The contrast is complex and hard to analyse by the programme. There is a cell network where the twin density is low.

The side view of twinning in sample [111] is shown in Figure 5.17. Only the

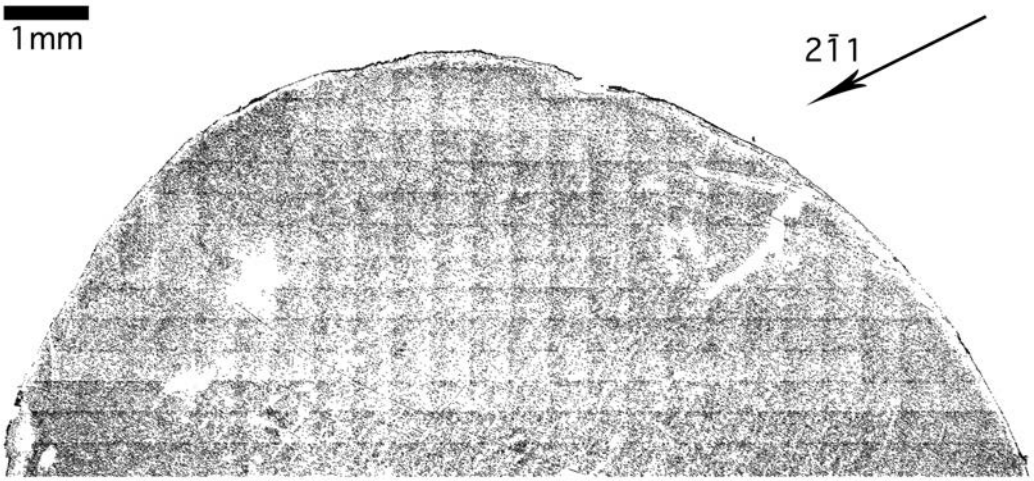


Figure 5.12: The distribution of twins on the front surface of sample [011]. Only half of the sample is shown in the figure since the distribution is symmetrical along the central line. The black lines in the graph are the twins. The density of twinning here is high and evenly distributed across the front surface. The horizontal and vertical straight lines on the image come from the stitching of multiple images.

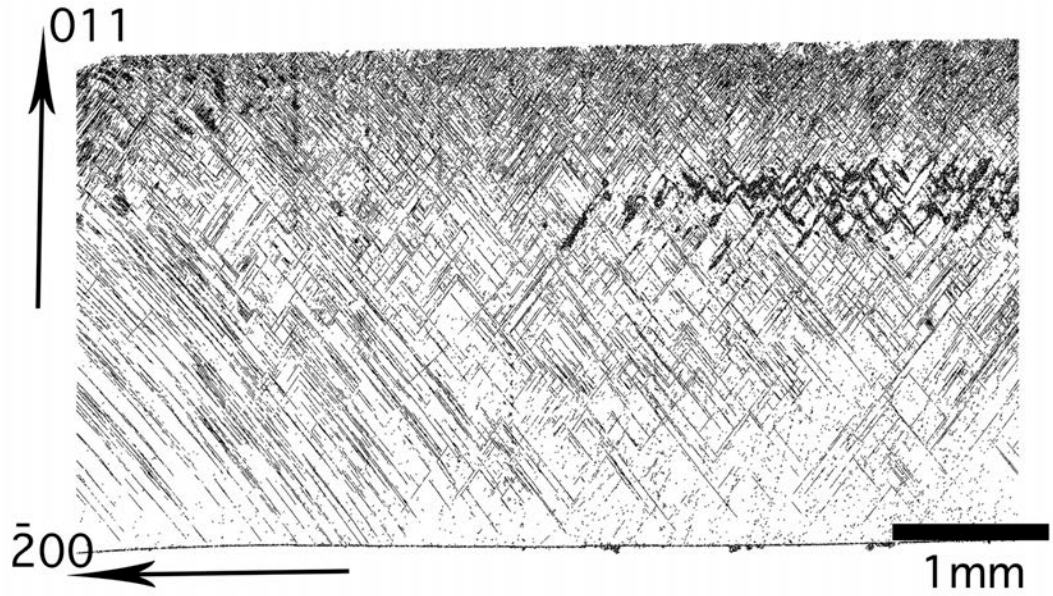


Figure 5.13: The distribution of twins on the side surface of sample [011]. Only half of the sample is shown in the figure since the distribution is symmetrical along the central line. The black lines in the graph are the twins. The twinning density is higher in the top and lower in the bottom.

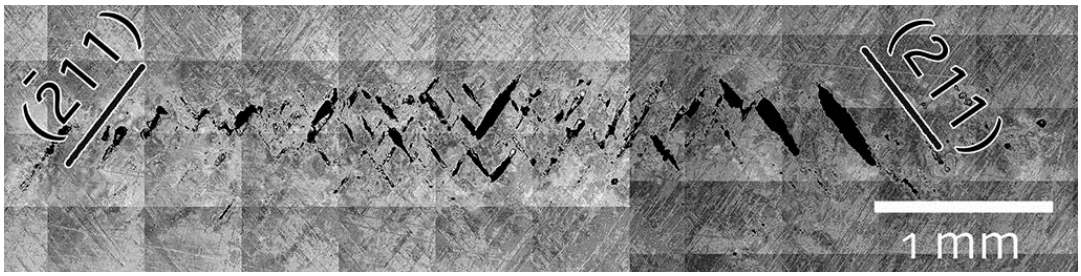


Figure 5.14: The void clusters in the [011] specimen. The voids are elongated and oriented in the same directions as the twins.

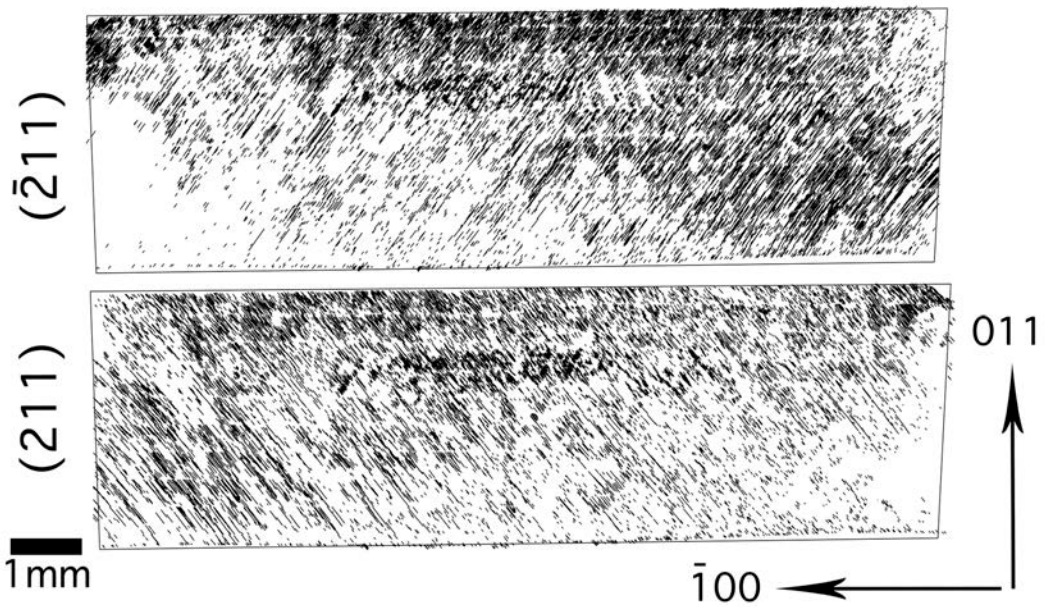


Figure 5.15: Distribution of ($\bar{2}11$) and (211) twins in [011] sample. The $\bar{2}11$ twins are popular on the right side and the 211 twins on the left.

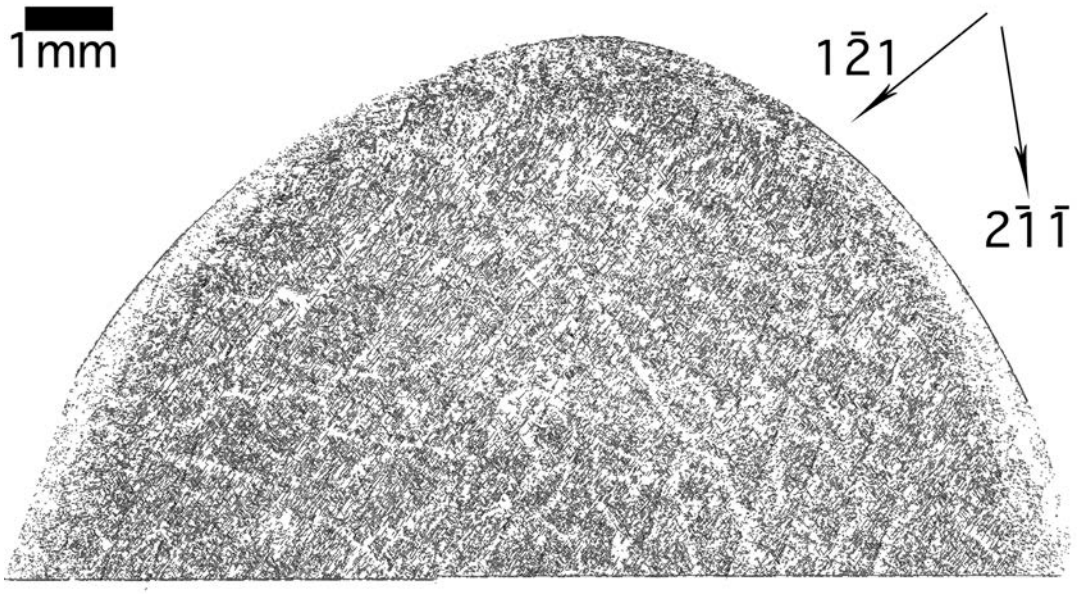


Figure 5.16: The distribution of twins on the front surface of the [111] sample. The twins on the [111] front surface are evenly distributed. In the region within 0.5 $mm$ of the edge, the image does not show much twinning because the material has very heavy residual strain here. The contrast is complex and hard to analyse by the programme. There is a cell network where the twin density is low.

right half of the sample is shown since the twin distribution is symmetrical about the central axis of the sample. The voids in this sample are not very obvious in the filtered image, because there is no contrast inside the voids in the original image. A stitched image of the voids is shown in Figure 5.18. Compared with the [011] sample, the void cluster here is thin and short, with dimensions 0.5 $mm$ thick vs 4 $mm$ long. Most voids are elliptical with the major axis parallel to the direction of the twins in the image. The twinning density is high at the front and edge surfaces, but low in the bottom centre of the specimen.

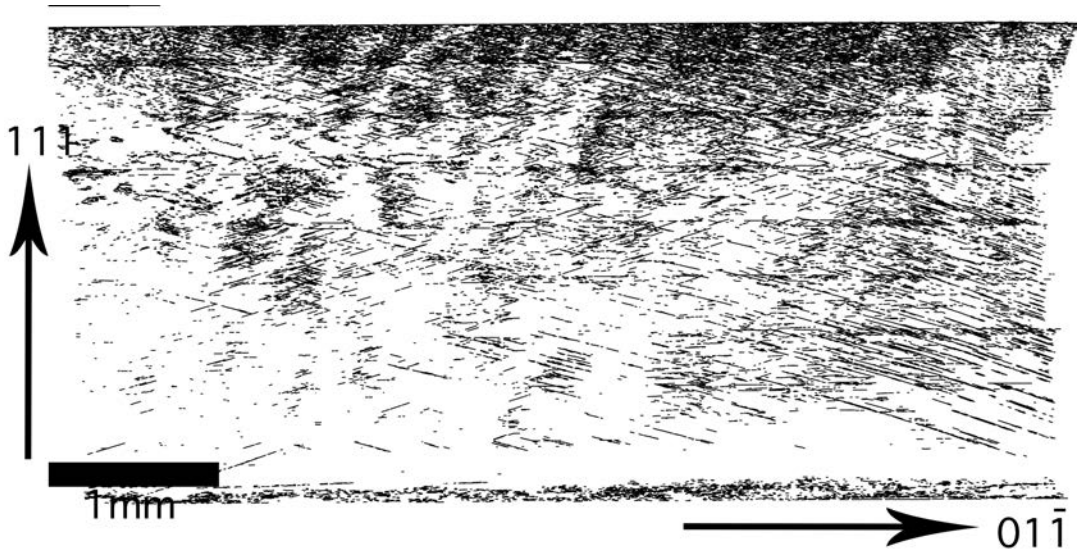


Figure 5.17: The distribution of twins on the side surface of the [111] sample. Only the right half of the sample is shown since the twin distribution is symmetrical about the central axis of the sample. The twinning density is high at the front and edge surfaces, but low in the bottom centre of the specimen.


Figure 5.18: The voids in the [111] specimen. Most voids are elliptical with the major axis parallel to the direction of the twins in the image.

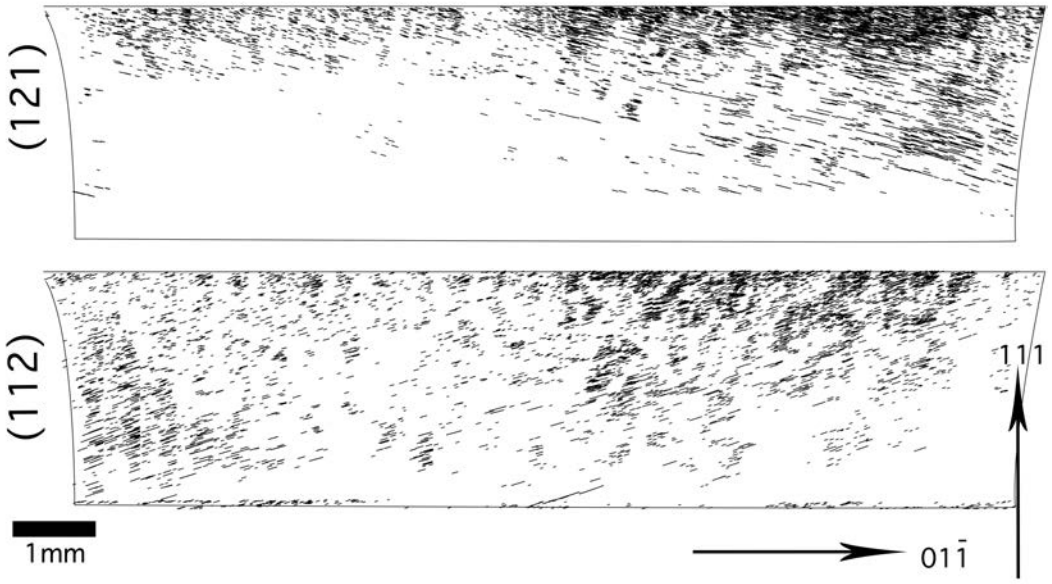


Figure 5.19: The distribution of (121) and (112) twins in the [111] sample. The (121) twins appear mainly on the right side and the (112) twins on the left.

The density of the (211) twins in sample [111] is very small so they were not processed by the FFT filter. The filtered images of the other two types of twin: (112) and (121) are shown in Figure 5.19. The (121) twins appear mainly on the right side and the (112) twins on the left.

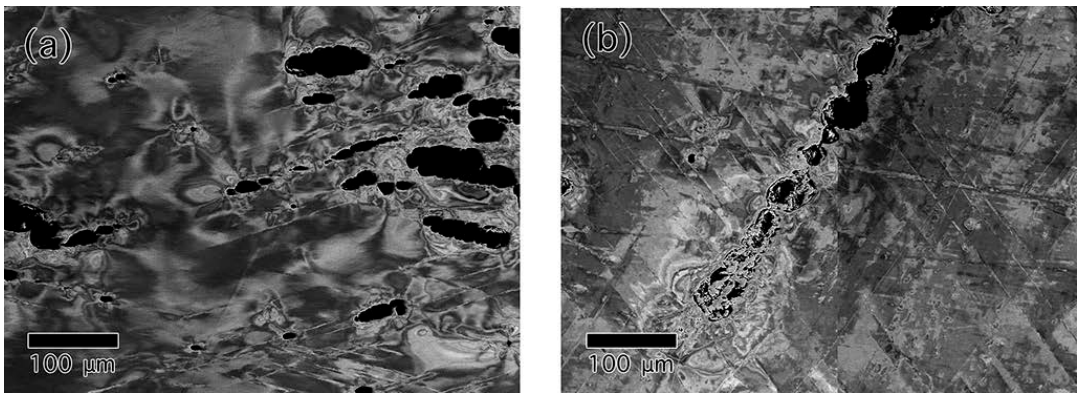


Figure 5.20: BSE image of voids in sample (a) 111; (b) 011

## 5.3 Dislocations

The sampling regions for TEM observation are shown in Figure 5.21. Two types of TEM discs were obtained from the slice in Figure 4.4. After electropolishing, the thin area to be characterised by TEM is $1 \sim 1.5\,mm$ away from the shock interface (TEM disc A) whereas disc B is close to the centre of the specimen ($4 \sim 4.5\,mm$ from the edge, $1.5 \sim 2\,mm$ from the sample centre). The directions of the shock wave and the release wave were carefully recorded on the edge of the discs using scratches. A list of the TEM specimen types is shown in Table 5.1. The shock wave direction (SWD) and the release wave direction (RWD: the radial direction towards the centre of the sample) are also shown in the table. In this section, 5.3, the location of the sample area is represented by symbols A and B, as shown in Figure 5.21.

Table 5.1: The crystallographic directions of the shock wave (SWD) and release wave (RWD) of the TEM discs

| Sample normal direction | SWD | RWD |
|---|---|---|
| [001] | $[00\bar{1}]$ | $[\bar{1}\bar{1}0]$ |
| [011] | $[0\bar{1}\bar{1}]$ | $[\bar{2}00]$ |
| [111] | $[\bar{1}\bar{1}\bar{1}]$ | $[1\bar{2}1]$ |

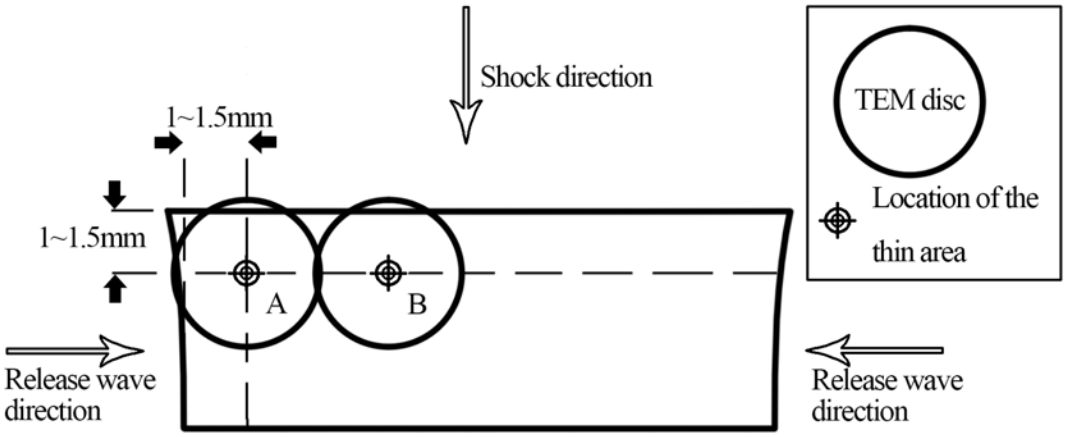


Figure 5.21: The location of the TEM thin area in the bulk specimen. The A and B point shows the location of the thin area characterised using TEM. A is close to the edge of the specimen and B is close to the centre.

### 5.3.1 Dislocation morphology

**TEM specimen [001]-A (close to edge)**

A TEM bright field micrograph of the dislocations in sample A (close to the edge, as shown in Figure 5.21) of Ta-001 is shown in Figure 5.22. The substructure after shock loading consisted of straight dislocation walls parallel to the shock wave

loading direction $[00\bar{2}]$. The width of each dislocation wall is around $100\,nm$. The spacing between them is $0.5 \sim 1\,\mu m$. In this space, the dislocation density is relatively low, and consists of long dislocations and small loops. There is a small misorientation in the crystal caused by the dislocation wall. This can be recognised from the brightness change of the bright field image across the walls.

**TEM specimen [001]-B (close to centre)**

The dislocation substructure imaged from the central region of Ta-001 (sample B in Figure 5.21) is shown in Figure 5.23. The majority of the dislocations in the image are long and straight in the $[\bar{1}11]$ and $[1\bar{1}1]$ directions. There are loose dislocation tangles homogeneously distributed throughout this area without any obvious preferred orientation. A high density of small dislocation loops is also observed in this region.

**TEM specimen [011]-A (close to edge)**

Similarly to Ta-001-A, the dislocations in sample A of Ta-011 also form into dislocation walls. This can be found in Figure 5.24. The dislocation walls have a thickness of around $100\,nm$, and lie parallel to the shock wave direction $0\bar{1}\bar{1}$. In some other areas of this specimen, instead of forming straight walls, the dislocation tangles are relatively loose, as shown in Figure 5.25, forming elongated dislocation cells. The spaces inside the cells and in between the walls are filled with low density long straight dislocations in the [111] and $[\bar{1}11]$ directions. The density of the small loops is similar to that in the [001] sample (Figure 5.23).

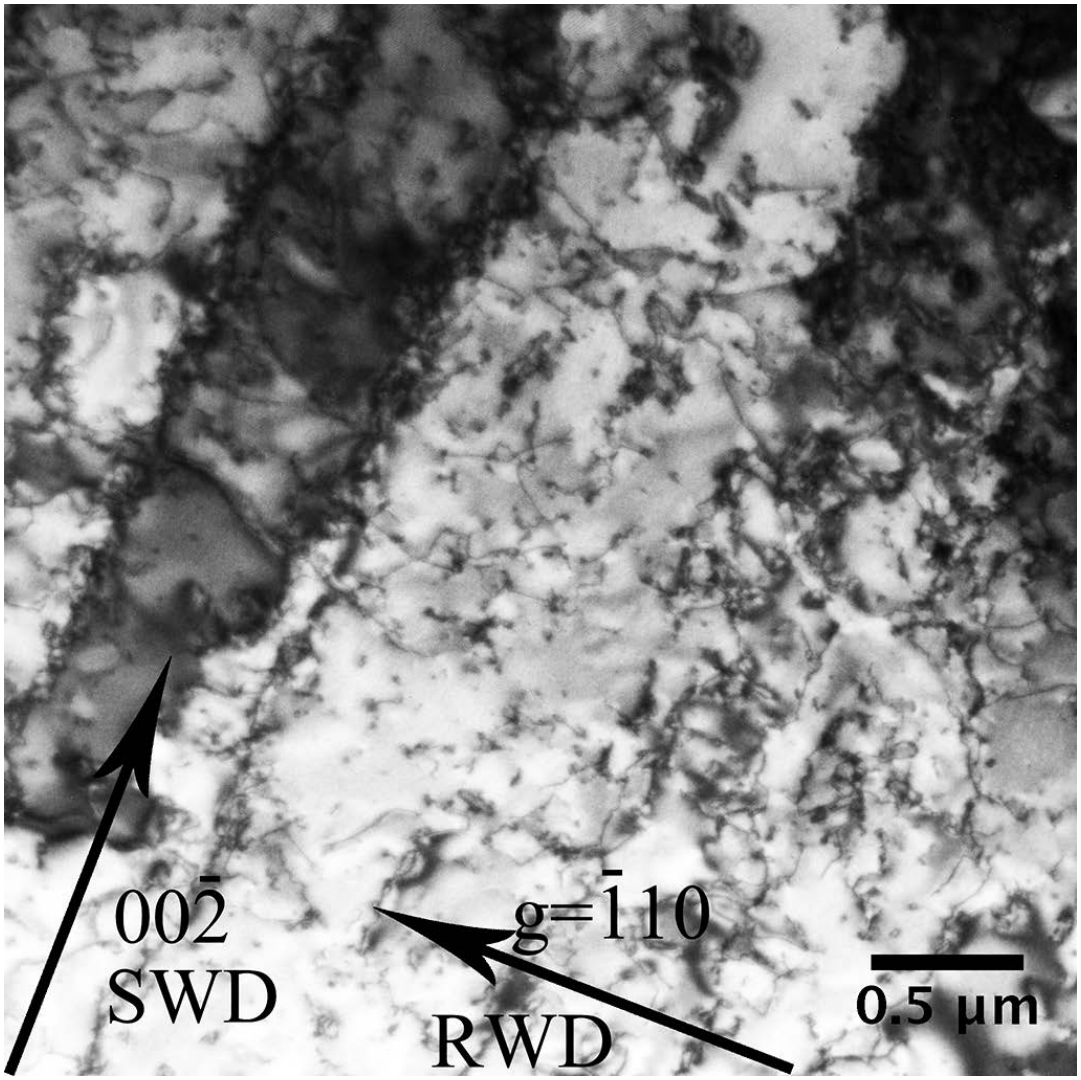


Figure 5.22: TEM bright field micrograph of sample A (close to the edge) of tantalum [001], B=[110]. SWD is shock wave direction and RWD is release wave direction.

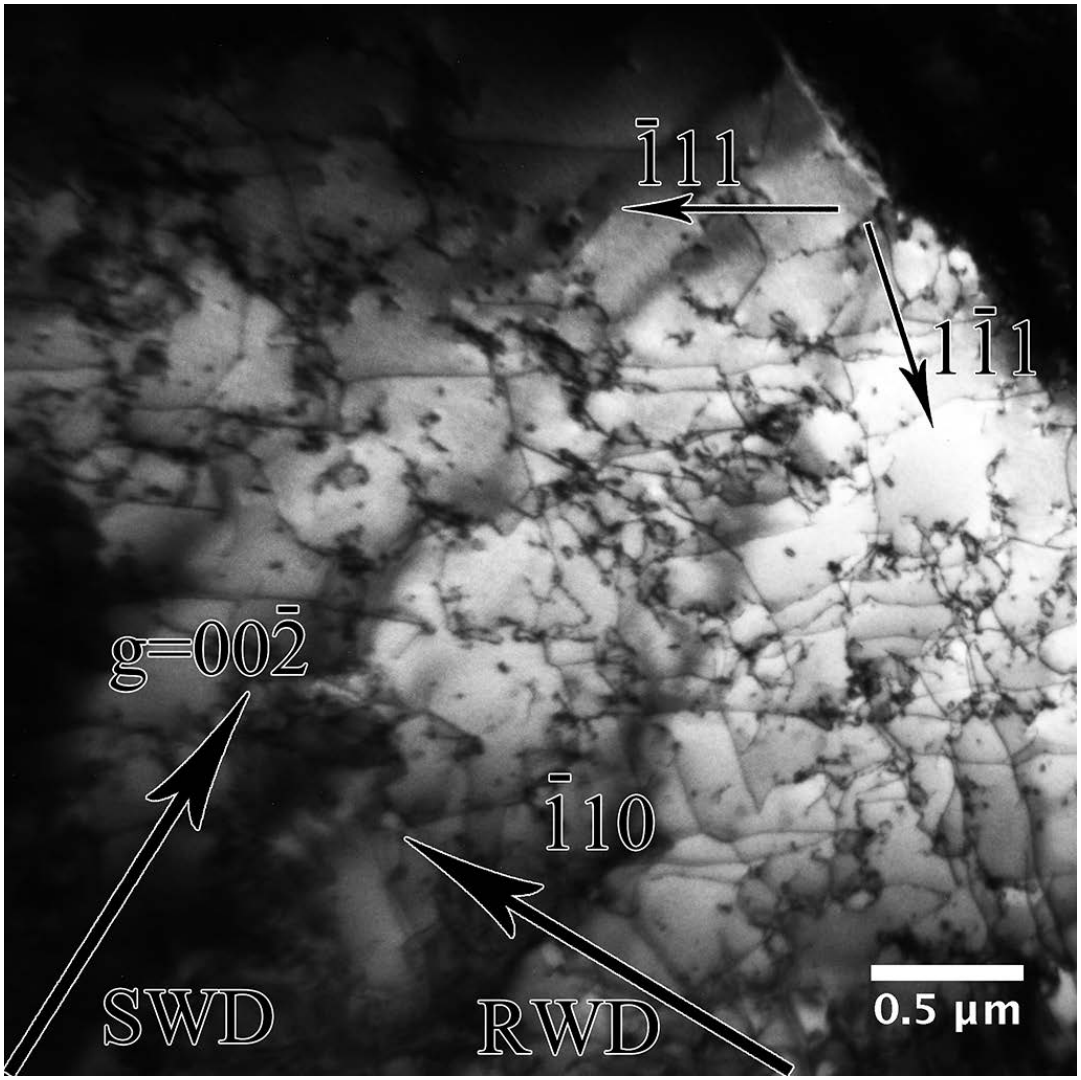


Figure 5.23: TEM bright-field micrograph of sample B (close to the centre) of tantalum [001], B=[110]. SWD is shock wave direction and RWD is release wave direction.

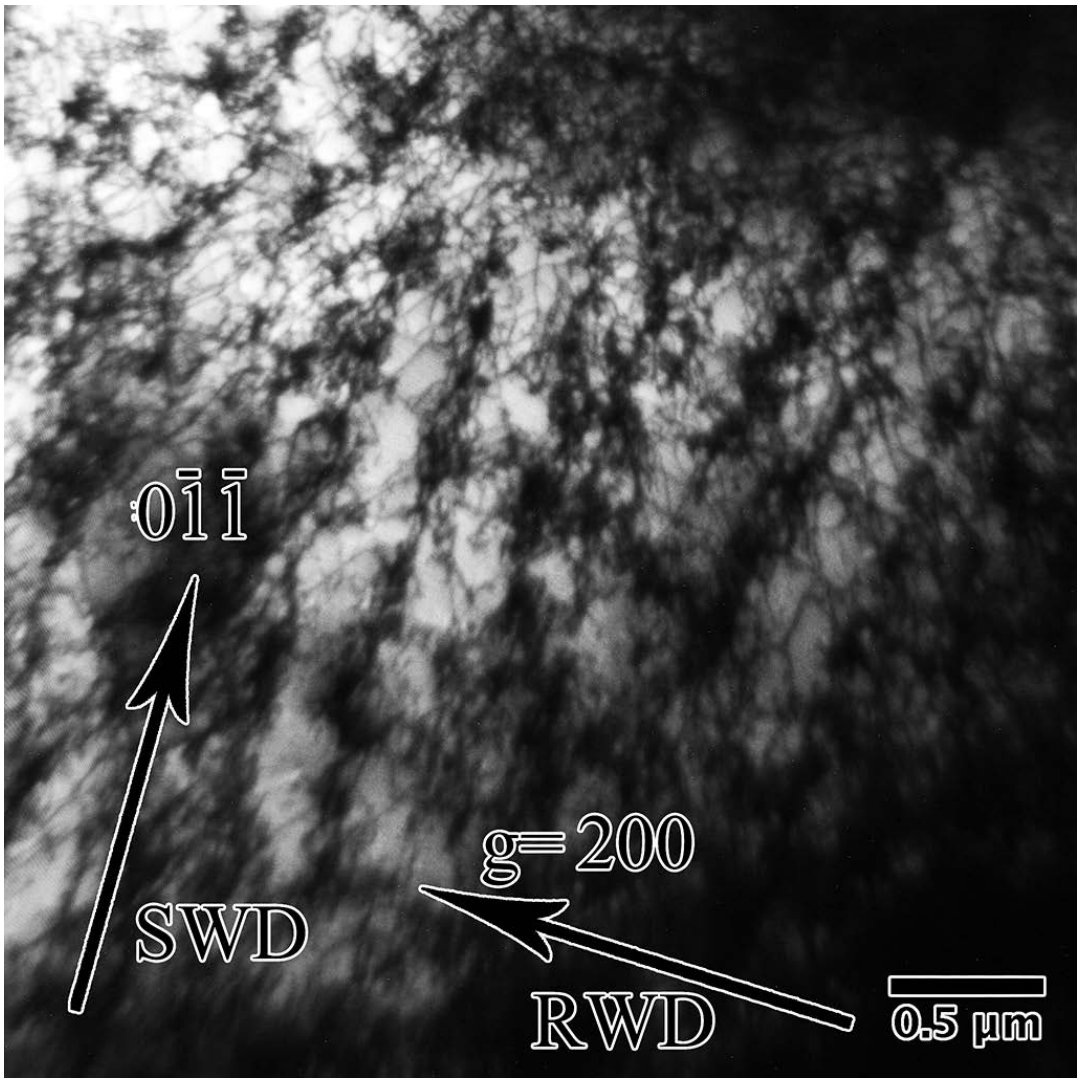


Figure 5.24: TEM bright field micrograph of sample A (close to the edge) of tantalum [011], with parallel dislocation walls, B=[0$\bar{1}$1]. SWD is shock wave direction and RWD is release wave direction.

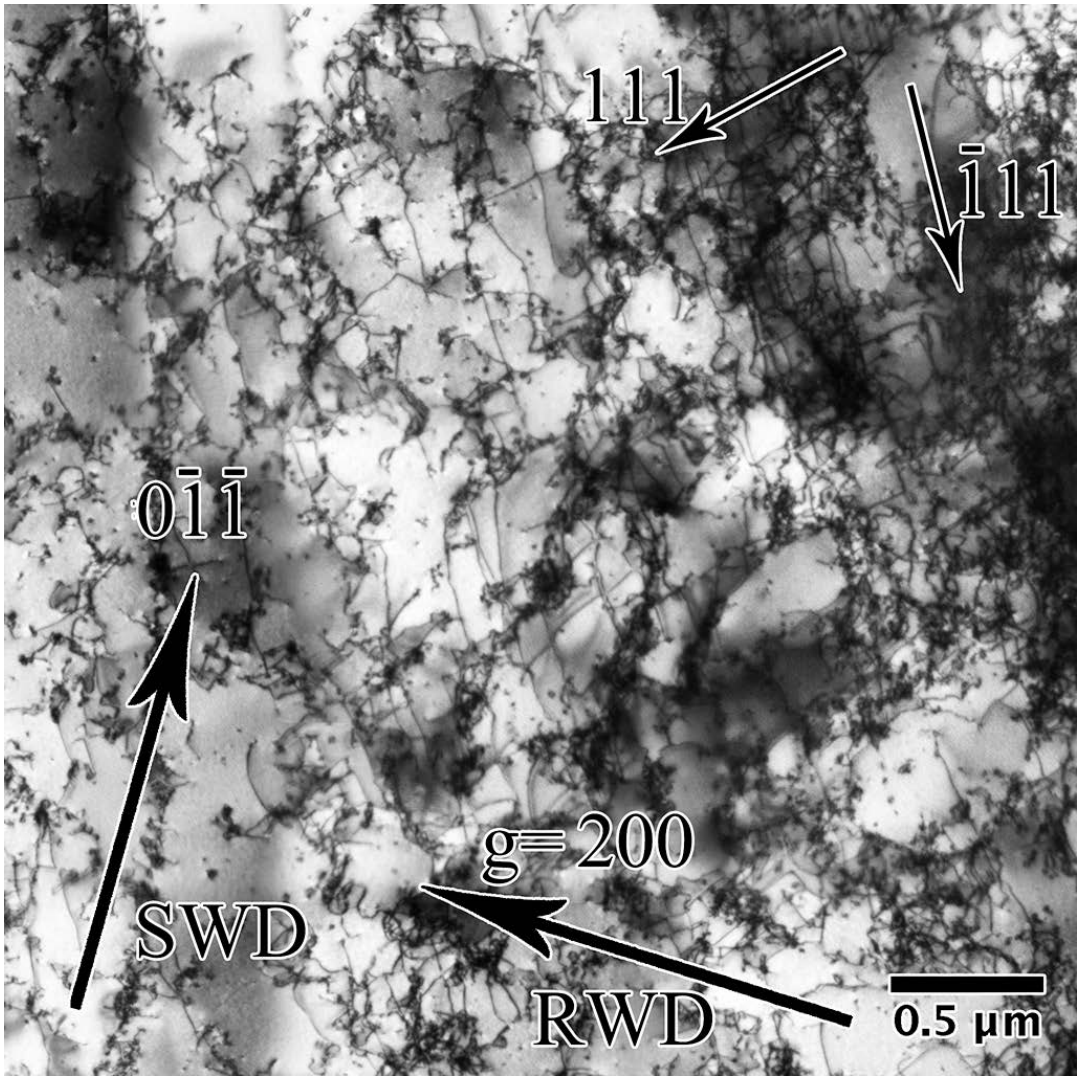


Figure 5.25: TEM bright field micrograph of sample A (close to the edge) of tantalum [011], with elongated dislocation cells,B=[$0\bar{1}1$]

**TEM specimen [011]-B (close to centre)**

Figure 5.26 shows the dislocation substructure of sample B of Ta-011. The sudden changes in the intensity of the matrix (vertical and horizontal) are caused by the stitching of multiple images. The dislocation tangles are randomly distributed across the specimen. The dislocations between the tangles are curly, without specific crystallographic directions.

**TEM specimen [111]-A (close to edge)**

The dislocation walls on the edge side of the Ta-111 specimen have two different orientations, parallel to the crystallographic directions [101] and [121]. They are shown in Figures 5.27 and 5.28, respectively. In the spacing between the [121] walls, there are some small dislocation tangles lying in the [111] direction, as labelled by the line 111 in Figure 5.28.

**TEM specimen [111]-B (close to centre)**

The dislocation substructure of the tantalum 111 sample B is shown in Figure 5.29. Several TEM images are stitched. The dislocations are heavily tangled in an irregular manner. The areas between these tangles contain straight dislocation lines parallel to the $0\bar{2}0$, $[1\bar{1}1]$ and [111] directions (on the image).

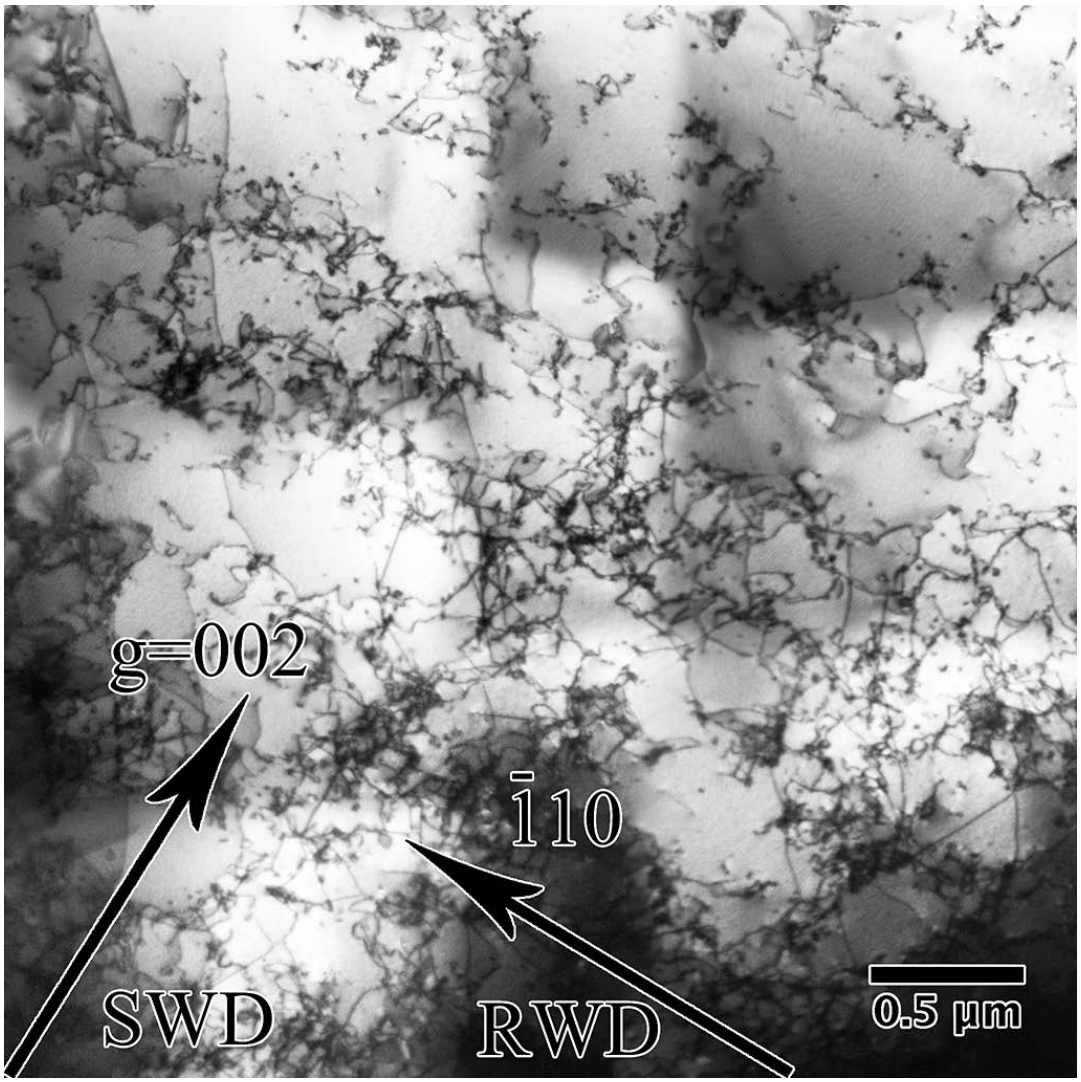


Figure 5.26: TEM bright field micrograph of sample B (close to the centre) of tantalum [011], B=[110]. SWD is shock wave direction and RWD is release wave direction.

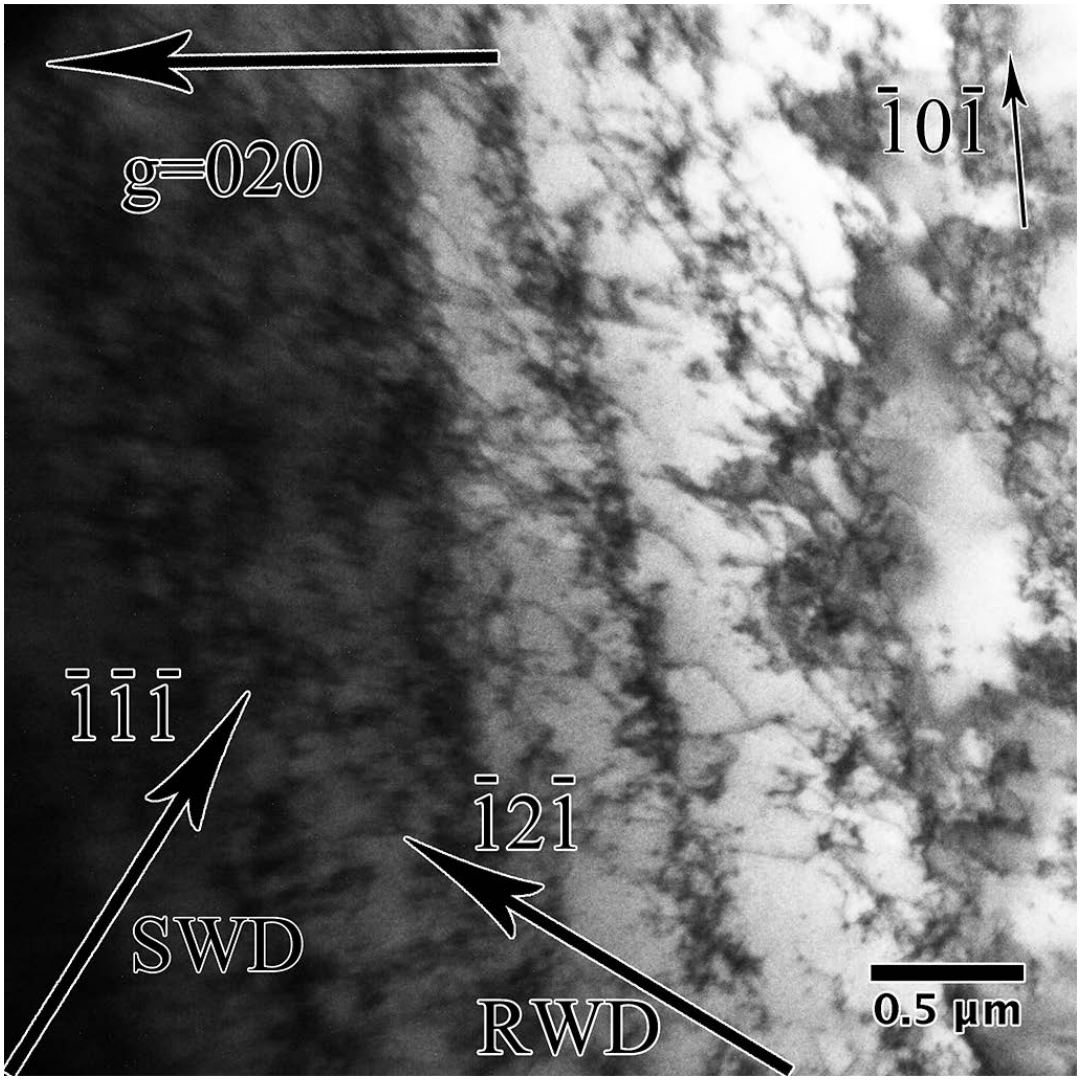


Figure 5.27: TEM bright field micrograph of sample A (close to the edge) of tantalum [111], B=[10$\bar{1}$]. SWD is shock wave direction and RWD is release wave direction.

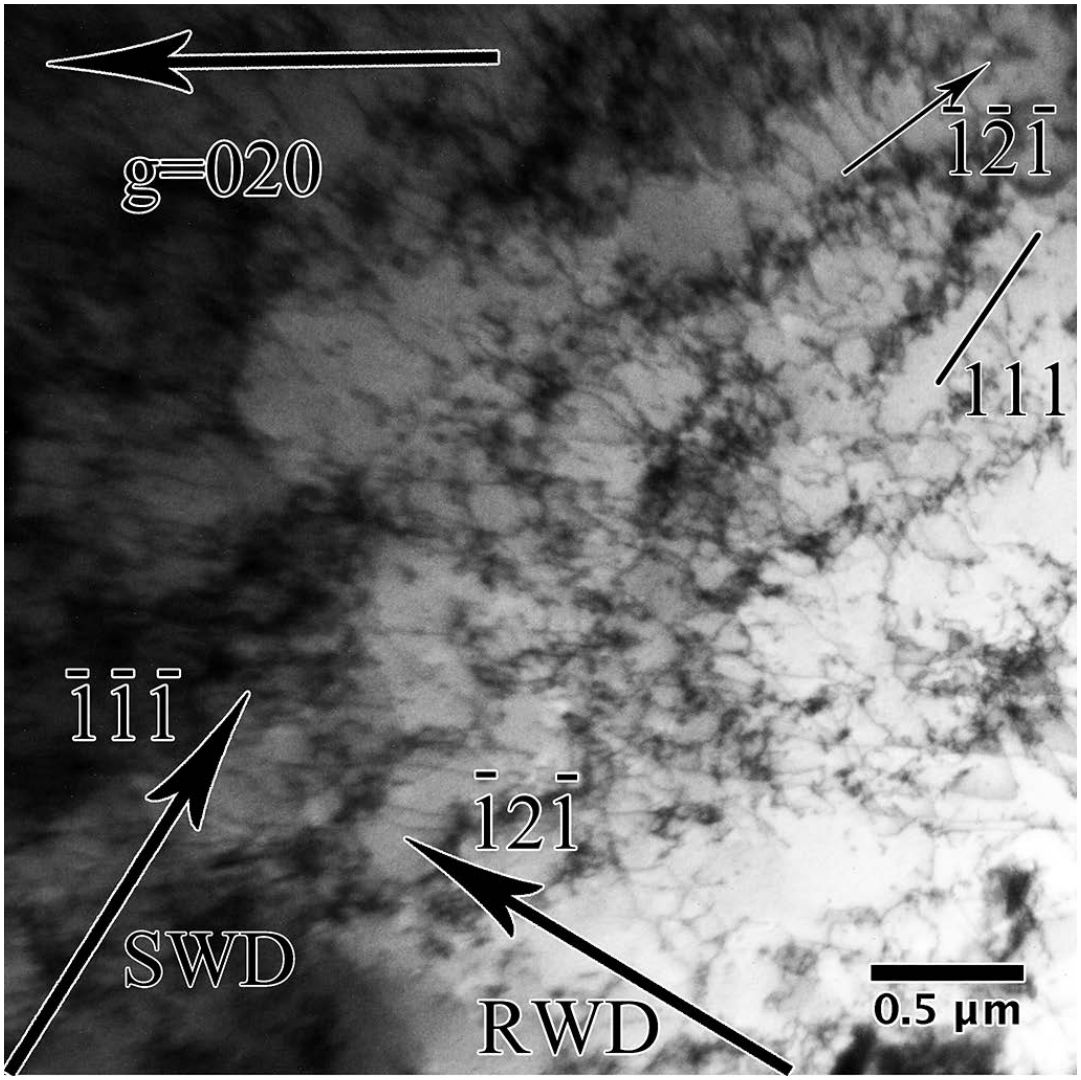


Figure 5.28: TEM bright field micrograph of sample A (close to the edge) of tantalum [111], B=[10$\bar{1}$]. SWD is shock wave direction and RWD is release wave direction.

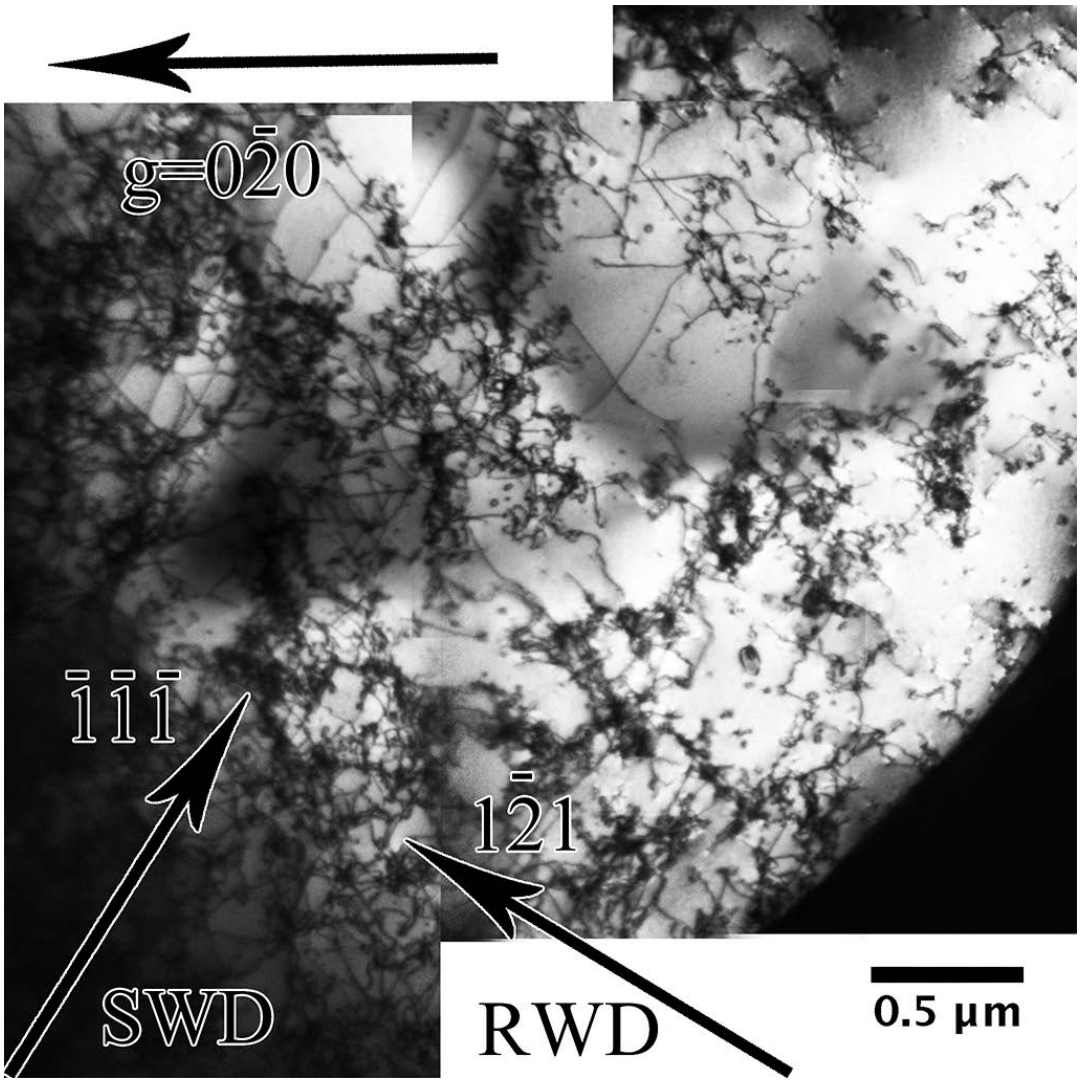


Figure 5.29: TEM bright field micrograph of sample B (close to the centre) of tantalum [111], B=[10$\bar{1}$]. SWD is shock wave direction and RWD is release wave direction.

### 5.3.2 Burgers vector analysis

The Burgers vectors of the dislocations in the tantalum TEM samples were studied using the $g \cdot b = 0$ extinction criterion. An example of the analysis is shown in Figure 5.30. The Burgers vector expected in a body-centred cubic material is $\frac{1}{2} < 111 >$. Using $g$ vector $\bar{2}00$ in Figure 5.30-(a), all the dislocations should be visible in the image. In image (b), using $g = \bar{1}10$, the dislocations with Burgers vector $\frac{1}{2}[111]$ and $\frac{1}{2}[11\bar{1}]$ will disappear. When using $g = \bar{1}1\bar{2}$, $b = \frac{1}{2}[\bar{1}11]$ disappears. The dislocations with $b = \frac{1}{2}[1\bar{1}1]$ or $b = \frac{1}{2}[111]$ will disappear at $g = 1\bar{1}\bar{2}$ and $g = \bar{1}2\bar{1}$, respectively. When comparing the micrographs Figure 5.30-(a), (b) and (e), very few dislocations disappear in the images with $g = \bar{1}10$ and $g = \bar{1}2\bar{1}$. This indicates that the density of $\frac{1}{2}[111]$ and $\frac{1}{2}[11\bar{1}]$ dislocations is very low. In the image (c) with $g = \bar{1}1\bar{2}$, all the dislocations parallel to the $[\bar{1}11]$ direction disappear. In the image (d) with $g = 1\bar{1}\bar{2}$, the dislocations parallel to $\bar{1}1\bar{1}$ disappear. This shows that the majority of the dislocations in this area are $\frac{1}{2}[\bar{1}11]$ and $\frac{1}{2}[\bar{1}1\bar{1}]$ screws.

The results of the Burgers vector analysis are shown in Table 5.2. For convenience, the $\frac{1}{2}$ before the crystal direction indices is skipped. It should be noted that the dislocation Burgers vectors listed all have a major presence in the TEM observations; the rare dislocation Burgers vectors or those which cannot be distinguished from the dislocation wall contrast, have not been listed. When using different $g$ vectors, the dislocation densities appear to show no significant change, meaning that the Burgers vectors listed in the table are equally activated in the same specimen.

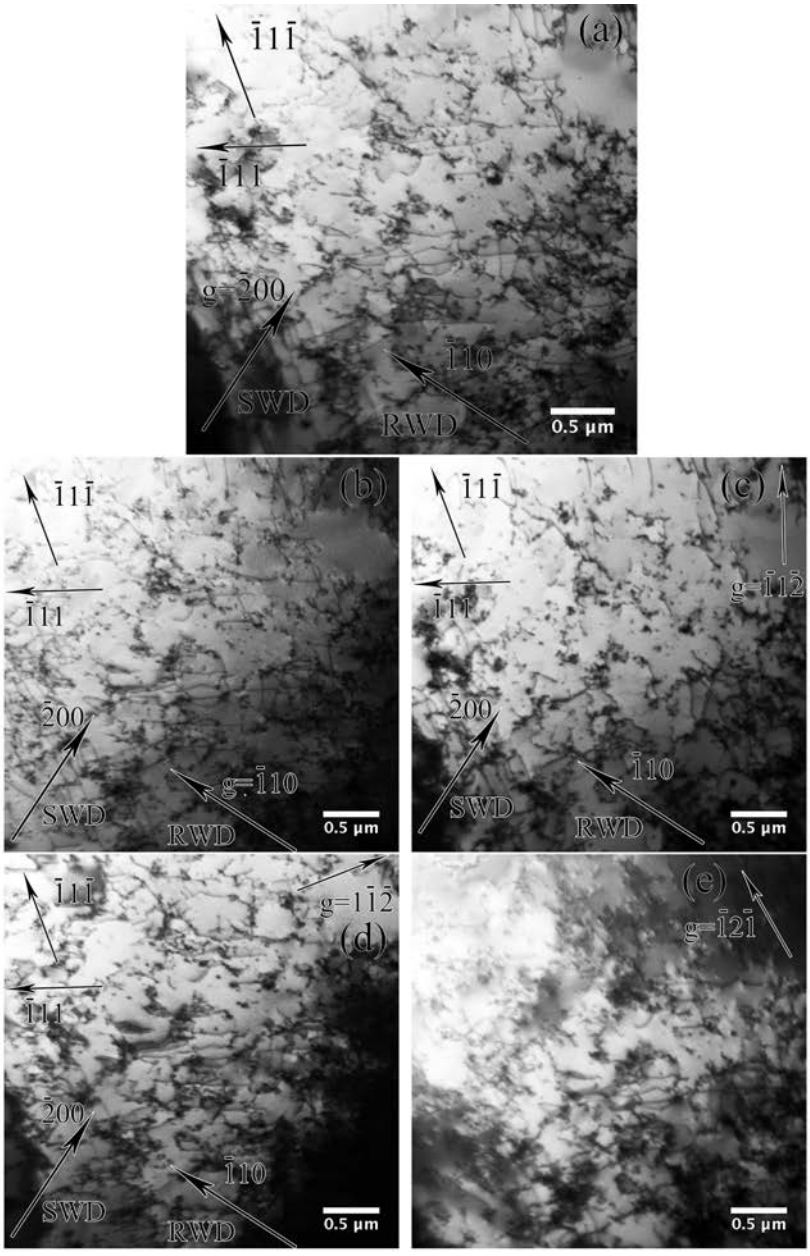


Figure 5.30: Burgers vector analysis of the Ta-001 sample B. (a) g=$\bar{2}00$; (b) g=$\bar{1}10$; (c) g=$\bar{1}1\bar{2}$ (d) g=$1\bar{1}\bar{2}$; (e) g=$\bar{1}2\bar{1}$

Table 5.2: Summary of dislocation Burgers vectors

| Specimen | A | B | Directions | |
|---|---|---|---|---|
| | Dominant Burgers vectors | | | |
| [001] | $\frac{1}{2}\bar{1}11]$, $\frac{1}{2}1\bar{1}1$ | $\frac{1}{2}\bar{1}11]$, $\frac{1}{2}1\bar{1}1$ | SWD | $[00\bar{2}]$ |
| | | | RWD | $[\bar{1}10]$ |
| [011] | $\frac{1}{2}[111]$, $\frac{1}{2}[\bar{1}11]$ | $\frac{1}{2}[111]$, $\frac{1}{2}[\bar{1}11]$, $\frac{1}{2}[1\bar{1}1]$, $\frac{1}{2}[11\bar{1}]$ | SWD | $[0\bar{1}\bar{1}]$ |
| | | | RWD | $[200]$ |
| [111] | $\frac{1}{2}[111]$, $\frac{1}{2}[\bar{1}11]$, $\frac{1}{2}[1\bar{1}1]$, $\frac{1}{2}[11\bar{1}]$ | $\frac{1}{2}[111]$, $\frac{1}{2}[\bar{1}11]$, $\frac{1}{2}[1\bar{1}1]$, $\frac{1}{2}[11\bar{1}]$ | SWD | $[\bar{1}\bar{1}\bar{1}]$ |
| | | | RWD | $[\bar{1}2\bar{1}]$ |

### 5.3.3 Electron channelling contrast images

#### Simulation of the electron channelling contrast profile

A simulation profile across a screw dislocation in a tantalum crystal at a depth of $0.2\xi g$ beneath the crystal surface is shown in Figure 5.31. The dislocation is at a distance 50 $nm$ from the middle of the material. The background BSE intensity of the profile is around 0.06 with a starting wave amplitude 1 at the crystal surface. The strain field of the dislocation has significantly altered the intensity of the backscattered electrons. The BSE intensity on the left side of the dislocation is lower than the average background intensity. Meanwhile, on the right side, the intensity is higher than the background. The peak and valley have widths of about $20nm$, which means that the total width of the simulated dislocation contrast is about $2\xi_g$.

The effect of the deviation parameter $w(w = s\xi_g)$ could be investigated by plotting the simulated profiles of dislocation for different deviation parameters. Figure 5.32 shows plots of a screw dislocation in Ta, with $0.2\xi_g$ depth and w equal to $-1$, $-0.5$, 0, 0.5 and 1. The background intensity of the material is high when the deviation parameter is increased. The profile with $w = 0$ is symmetrical about the

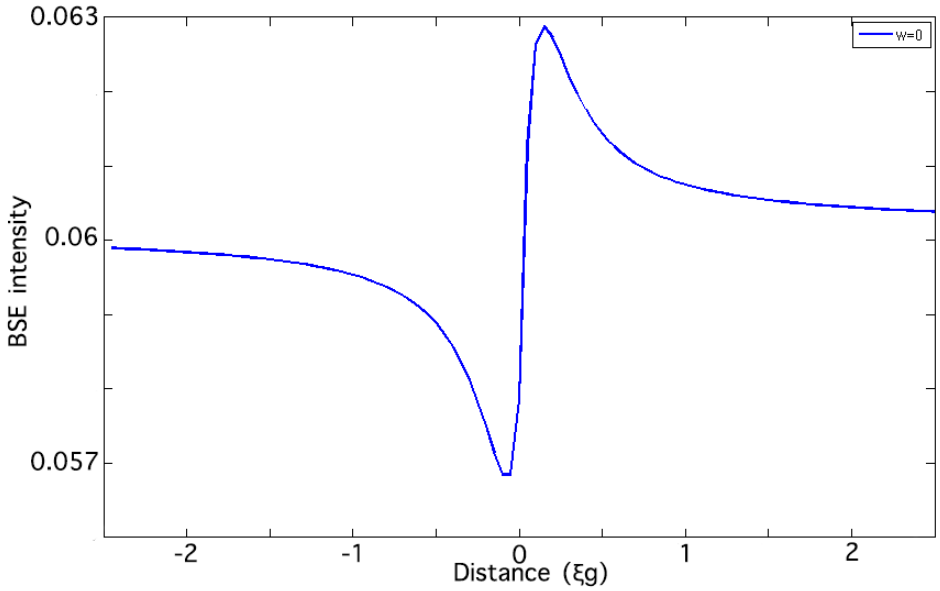


Figure 5.31: The simulated profile of backscattered electron intensity of a screw dislocation with $w = 0$, dislocation depth $0.2\xi_g$.

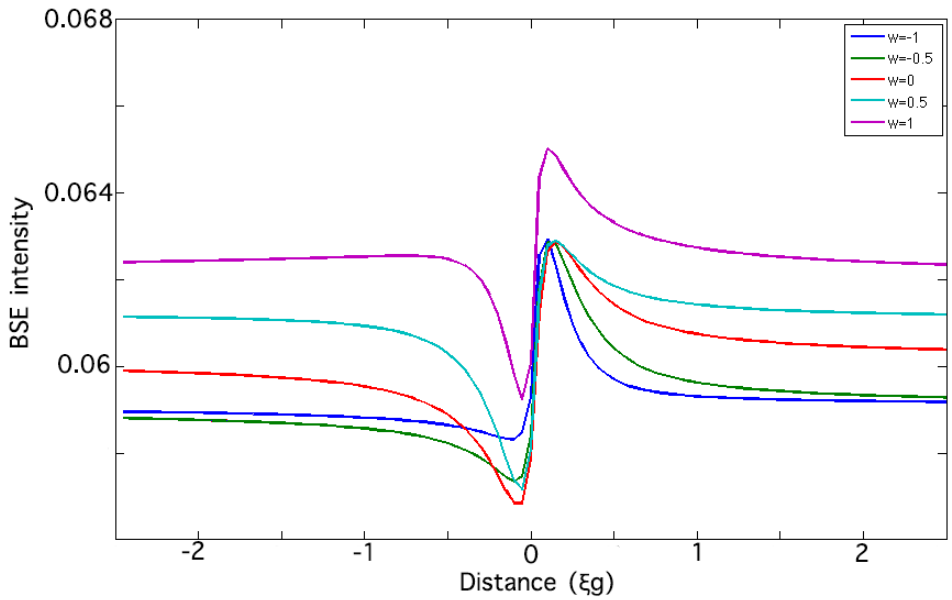


Figure 5.32: BSE intensity profiles of a screw dislocation with various deviation parameters $w$, dislocation depth $0.2\xi_g$

background intensity. When w is becomes negative, the background reduces dramatically. The peak point of the profile stays at around 0.063, the same as for the $w = 0$ plot. The bottom points of the valleys are lifted close to the background, making the plot a single peak on the right side of the dislocation. When the deviation parameter w is positive the background intensity increases and the contrast of the dislocation decreases. In summary, the dislocation contrast of a ECCI optimises at $w = 0$.

In the examination of the effect of dislocation depth, the deviation parameter w was set to 0. The profiles are shown in Figure 5.33. All the plots have the same background intensity. The width of the dislocation image becomes slightly smaller

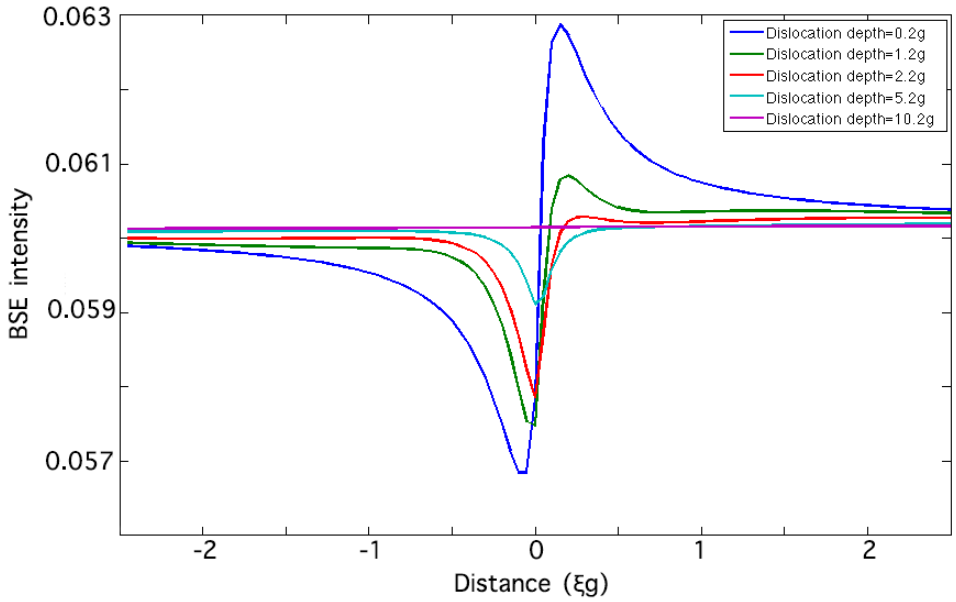


Figure 5.33: BSE intensity profile of a screw dislocation at various depths with imaging deviation parameter 0.

when the dislocation position become deeper in the material, but still within a range of around $30 - 50nm$. The contrast of the dislocation gradually attenuates with increasing depth, periodically rising and falling with a period of the extinction distance. The dislocation contrast totally disappears at a depth of around $10\xi_g$.

### Dislocation images from TEM and ECCI

A TEM micrograph of the shock-loaded tantalum is shown in Figure 5.34a. It could be seen that most of the dislocations in the specimen form a tangled structure with some loops/debris and individual dislocation lines in between. The same thin area of this TEM foil was examined by ECCI. Because the signal of the backscattered

electrons (which is the signal used in ECCI) is influenced by the specimen thickness, the brightness of the background of the electron channelling contrast image varies strongly across the image. This makes it difficult to optimise the contrast of all the dislocations in the image at the same time. Therefore, multiple images were taken of the same area and stitched together. The stitched electron channelling contrast image of the same area is shown in Figure 5.34b. The fringes on the image are a result of the image stitching. The image colour has been reversed to fit in with the TEM micrograph. The dislocation contrast in the ECCI is not as strong as in the TEM bright field image. There is a large number of dislocations in the TEM images absent in the ECC image. However the remaining dislocations show good agreement with the TEM bright field image. When using the same $g$ vector, all the dislocations in the ECCI can be found in the bright field image. For example, as shown in the higher magnification Figure 5.35, part of dislocation $A$ appears as line $A'$ in the ECCI in Figure 5.35b.

Burgers vectors analysis was carried out on the dislocation $A$ by taking a bright field image using three $g$ vectors $11\bar{1}$, $1\bar{1}1$ and $\bar{1}11$. These images are shown in Figure 5.36, which has a $g$ vector of $1\bar{1}0$. This indicates that the dislocation has Burgers vector $11\bar{1}$.

Tilting was employed to determine the slip plane of the dislocations. It can be seen in Figure 5.38 that the dislocation line $A$ from Figure 5.35 becomes longer as the beam direction approaches [231] from [213] (following the tilting shown in the stereographic projection in Figure 5.37). This suggests that the dislocation has slip plane (101).

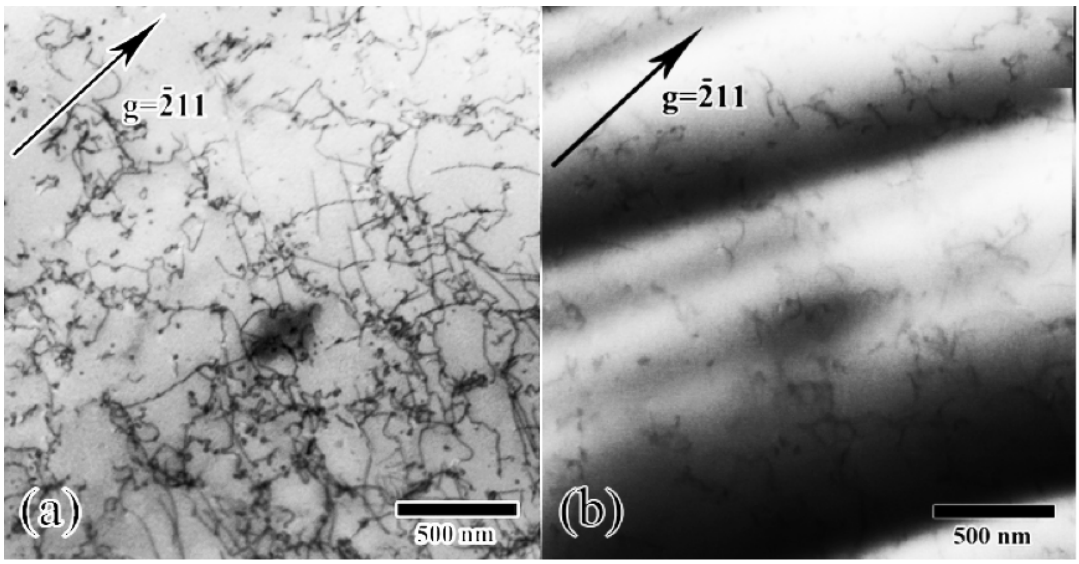


Figure 5.34: (a) TEM micrograph of the dislocations in the TEM foil of shock loaded tantalum single crystal with loading direction [111]; (b) ECCI of dislocations in the same area as (a)

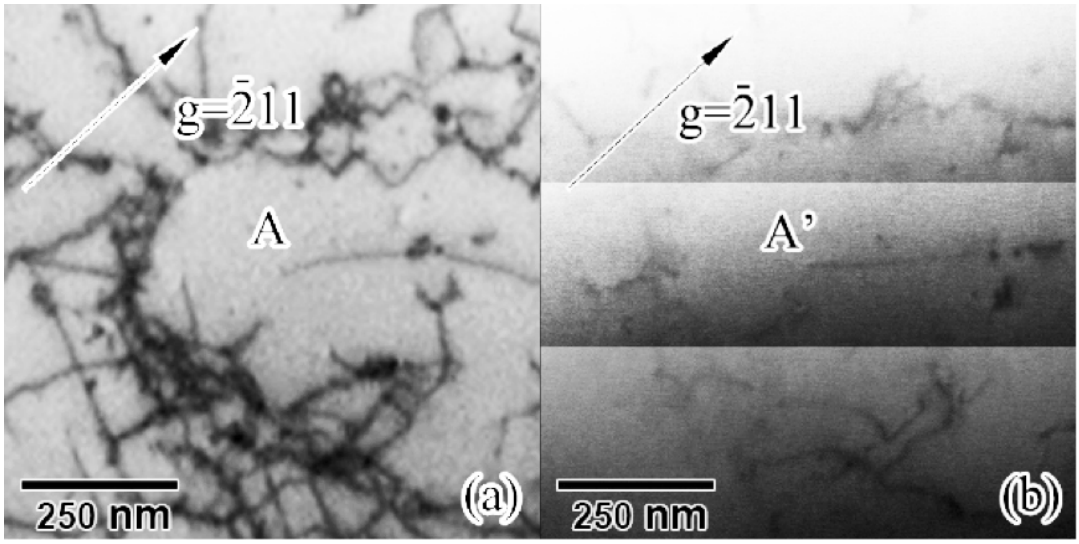


Figure 5.35: Dislocation micrographs showing detailed one-to-one correspondence between dislocation image in TEM and ECCI, (a) TEM (b) ECCI

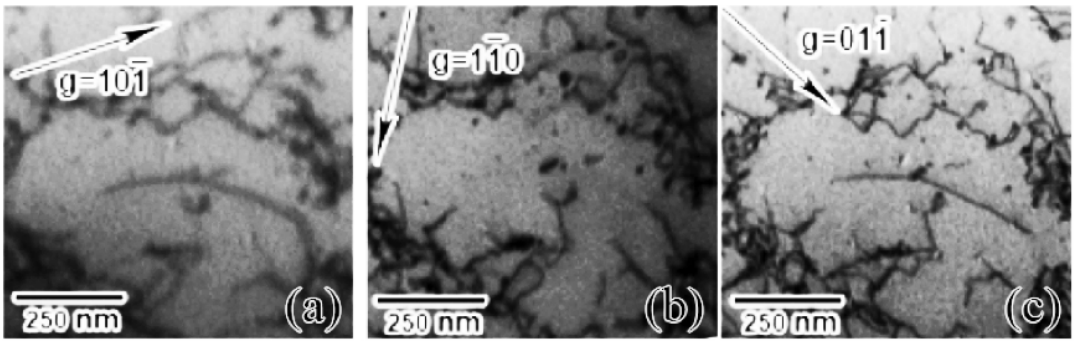


Figure 5.36: TEM Burgers vector analysis for dislocation A in Figure 5.35. (a) $g = 10\bar{1}$; (b) $g = 1\bar{1}0$; (c) $g = 01\bar{1}$

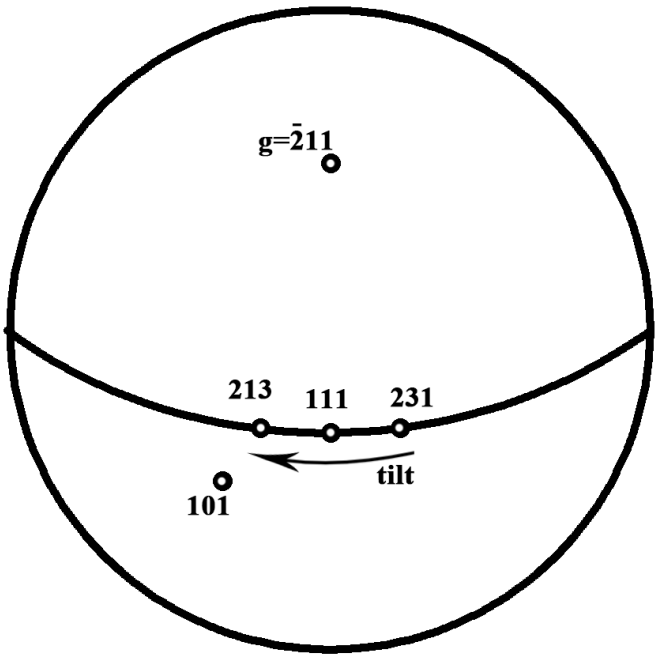


Figure 5.37: Stereographic projection of tilting experiment of Figure 5.38. The beam direction was tilted from [231] to [213].

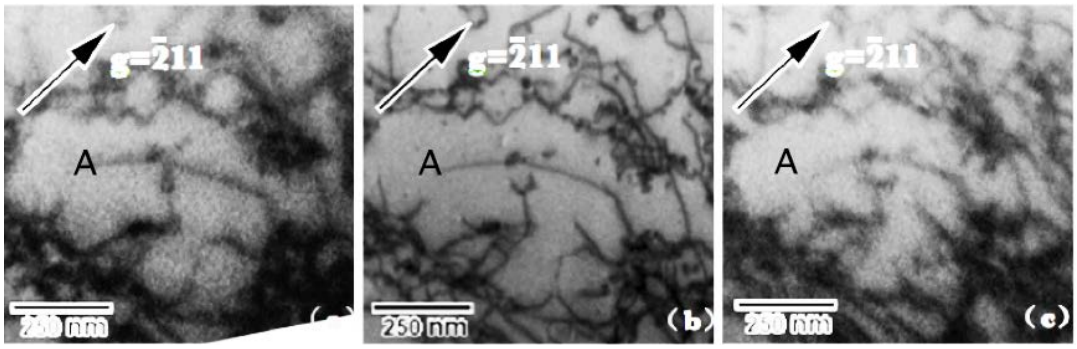


Figure 5.38: TEM bright field image of the dislocation at three different beam directions: (a) $B \approx [231]$; (b) $B \approx [111]$; (c) $B \approx [213]$

The configuration of dislocation $A$ is sketched in Figure 5.39. It can be seen that when tilted along the same $g$ vector $\bar{2}11$ as in the TEM, the image of the dislocation line changes in the same way as in the TEM.

Only part of the dislocation line appears in the ECC image, as shown in Figure 5.35. As shown in Figure 5.40, the visible dislocation line has a length of 200 $nm$ only. However, the total length of the dislocation is greater than 400 $nm$. This is due to the effective penetration depth of the $30kV$ electron in the SEM being shorter than can be seen in the TEM. This mechanism is shown in Figure 5.40. The red part of the dislocation is visible in the electron channelling contrast image. Through contrast calculations of many dislocations the average penetration depth of the electrons is around 120 $nm$ (about $6\xi_g$).

### The effect of the deviation parameter on the dislocation image

To optimise the dislocation contrast in ECCI, the effect of the deviation parameter was investigated by taking an image of the same area using a range of beam directions

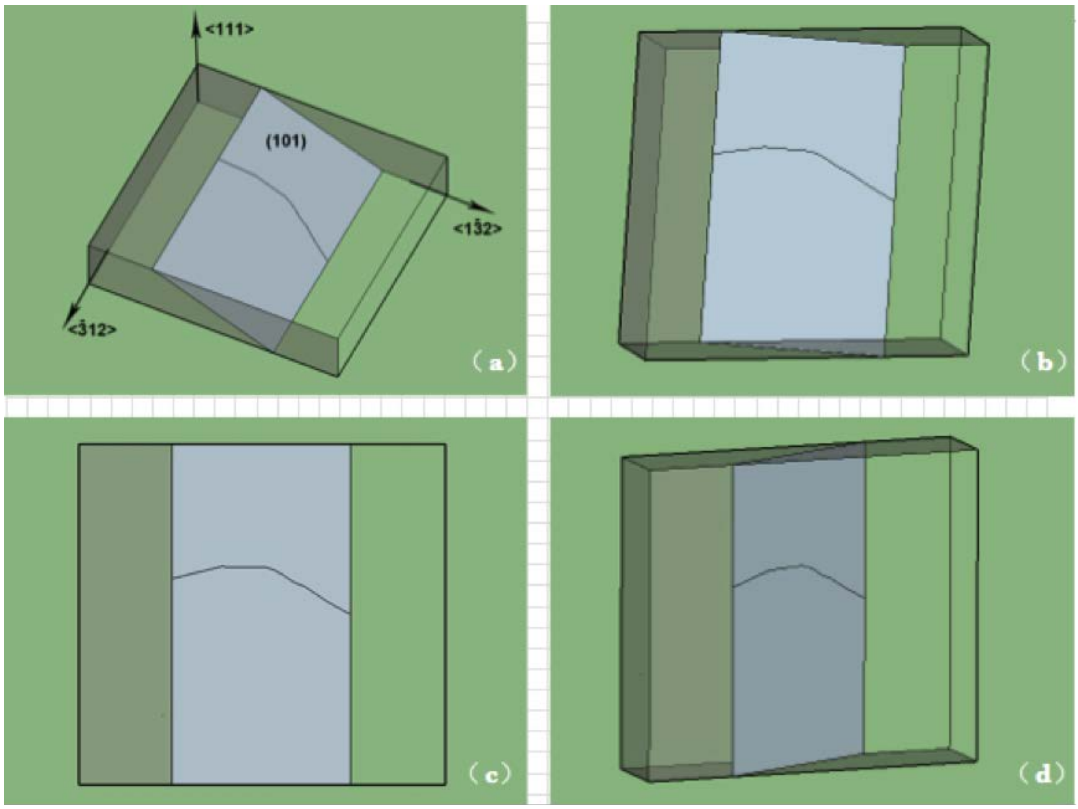


Figure 5.39: Sketch of dislocation A: The semi-transparent brick represents the TEM foil. A dislocation line starts from the top and ends at the bottom. The slip plane is (101). (a) Overview of the dislocations in the foil; (b) $B \approx [213]$; (c) $B \approx [111]$; (d) $B \approx [231]$.

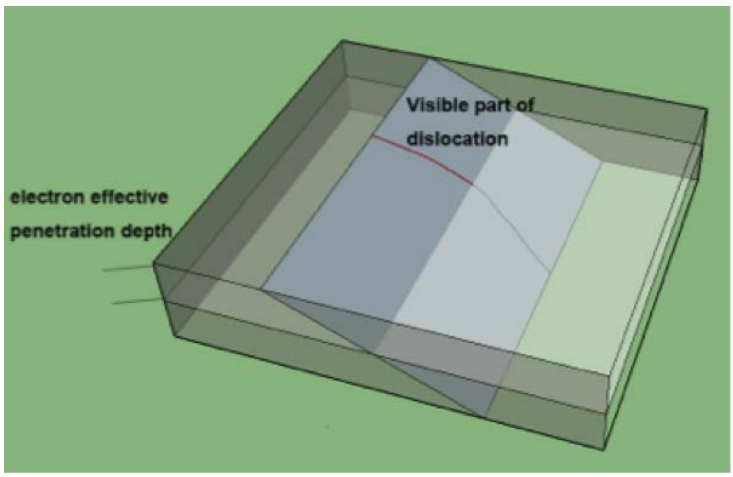


Figure 5.40: Sketch of the visible part of the dislocation in the electron channelling contrast image

with the same $g$ vector. The contrast of the dislocations was then measured as the intensity of the peak over the background intensity of the ECCI, as shown by the example in Figure 5.41. This method was applied to dislocation images taken at several different beam directions and beam voltages.

The influence of the deviation parameter is shown in Figure 5.42, in which all the images are taken using $30kV$. The $y$ axis is the contrast of dislocation images on the grey scale. The $x$ axis is the deviation parameter $w$. When $x = 0$ the beam direction is exactly at the Bragg condition for the $\bar{2}11$ reflection. It can be seen that the contrast is low at negative $s$, increases with deviation parameter up to the Bragg condition and decreases subsequently with $s$ when $s$ is positive. The maximum dislocation contrast is around 0.22 at the exact Bragg condition. From the actual images it is found that when $s$ is positive and small (less than 0.5), the contrast of the dislocation is acceptable.

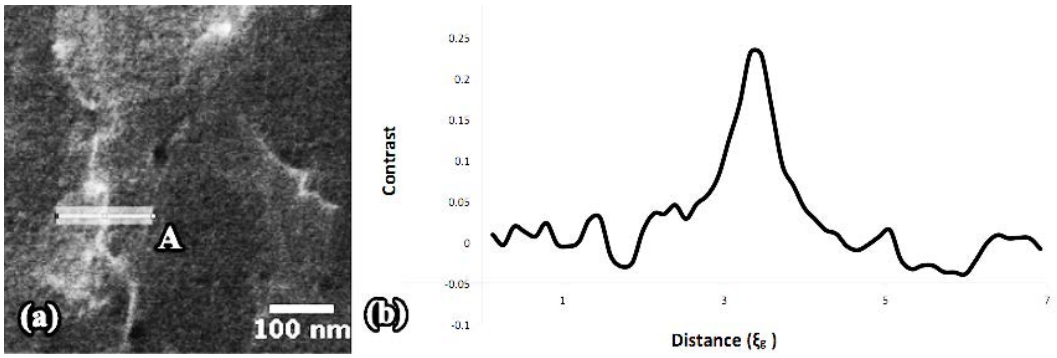


Figure 5.41: The procedure of the dislocation profile measurement on the ECCI. The brightness of the backscattered electron image along the line A in (a) is plotted against the distance in (b).

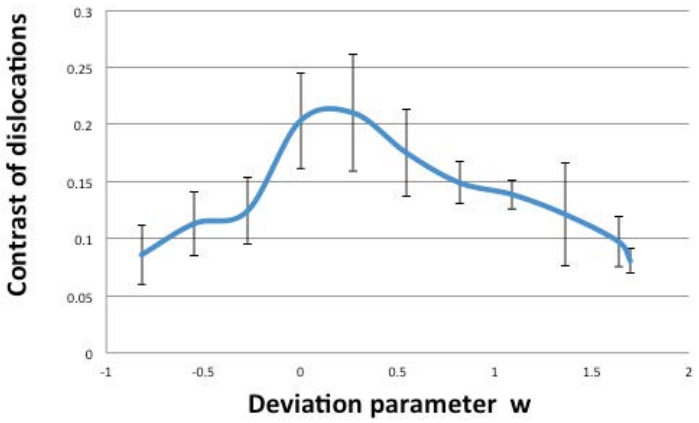


Figure 5.42: The influence of deviation parameter on the contrast of dislocations in ECCI. The contrast becomes highest when the deviation parameter close to 0.

### Dislocation density measurement

The dislocation density in the imaged area has been measured by counting the number of dislocation ends on the TEM bright field image. In Figure 5.43 it is $3.6 \times 10^{13}\, m^{-2}$. The dislocation density measured by ECCI using the same method is $3.4 \times 10^{13}\, m^{-2}$. The imaging depth of ECCI is known to be $120\, nm$ in the current set-up. The densities of the dislocations were then calculated using this depth. Several lines were drawn on the electron channelling contrast image. The dislocations crossed by these lines were counted (as $N$). The average dislocation density is then $n = \frac{N}{dL}$, where $d$ is the imaging depth of the ECCI and $L$ is the total length of these lines. The dislocation density measured by this method was $4.0 \times 10^{13}\, m^{-2}$.

### Application of ECCI to dislocation density measurement in shocked tantalum

The imaging condition ($30kV$, Bragg condition) was then applied to the shock loaded tantalum single crystal with a [011] loading direction. The dislocation densities were measured at the sample edge and centre and at the front (shocked) surface and back surface. The results are shown in Figure 5.43. It can be seen that the dislocation density is high (around $10^{12}\, m^{-2}$) close to the shock interface, but that far away from the interface there is a relatively low dislocation density. The region near the sample edge always has higher dislocation density than the central region except at the front surface, which has a consistently high density.

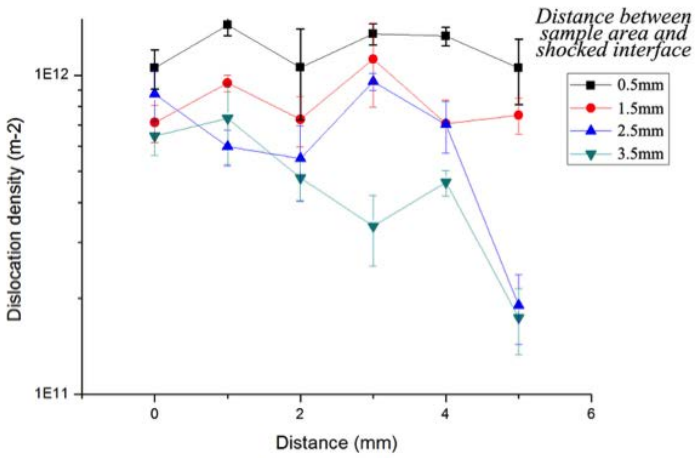


Figure 5.43: The dislocation density distribution of the shocked tantalum single crystal measured using ECCI

### 5.3.4 Dislocation density distribution

The transverse specimens through the tantalum single crystals were imaged using ECCI. The dislocation densities were measured by counting the number of dislocations in the images. The dislocation density $\rho$ is then:

$$\rho = \frac{N}{A} \tag{5.1}$$

where $N$ is the number of dislocations in the electron channelling contrast image. $A$ is the area of the ECCI. The dislocation density in the lateral surface of the sample [001] is plotted in Figure 5.44 vs distance from the sample edge. The $x$ axis is the distance from the edge to the sample point. The $y$ axis is the dislocation density. The different lines in this figure show the dislocation density for different distances

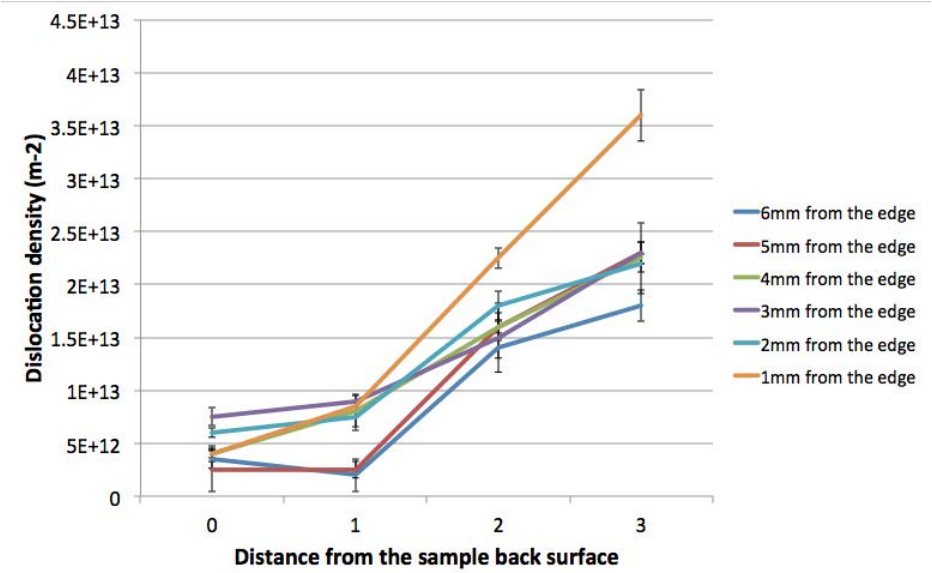


Figure 5.44: Dislocation density distribution in sample [001] is plotted against the distance from the sample back surface. The average dislocation density at the front surface of the sample is about 7 times higher than it is at the back surface. There are generally more dislocations at the edge of the specimen than in the central region.

from the shocked interface. Similar to the twinning distribution, the dislocation density is high in the region close to the shocked interface, and gradually decreases with distance. The average dislocation density at the front surface of the sample is about 7 times higher than it is at the back surface. There are generally more dislocations at the edge of the specimen than in the central region.

The dislocation density distribution of the [011] sample is shown in Figure 5.45. Again, the dislocation density is higher closer to the shock front surface. In the region close to the front surface ($0.5 - 1.5\,mm$), the density of the dislocations does not change much between the edge and centre. In the region $2.5\,mm$ from the front surface of the specimen, it is significantly less than close to the sample centre. At

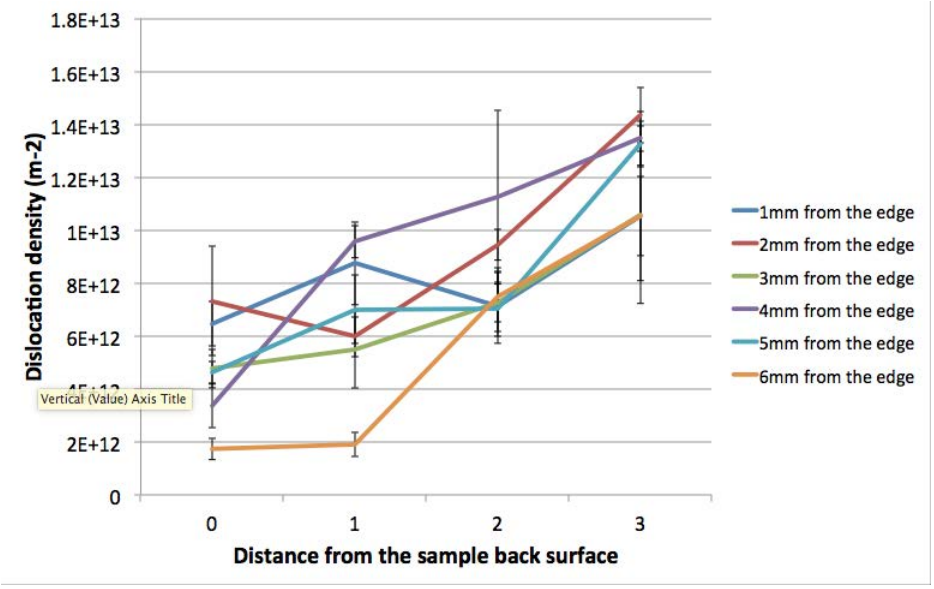


Figure 5.45: Dislocation density distribution in sample [011] is plotted against the distance from the sample back surface. The dislocation density at the front surface of the sample is higher than it is at the back surface.

the back surface, the dislocation density decreases from $6.5 \times 10^{12}\, m^{-2}$ at the edge to $1.9 \times 10^{12}\, m^{-2}$ at the centre.

There is a large difference between the dislocation density at the front edge and the front middle of the [111] sample. As shown in Figure 5.46, the lines at $0.5\, mm$ and $1.5\, mm$ fall from about $2 \times 10^{13}\, m^{-2}$ at the edge of the specimen to around $5 \times 10^{12}\, m^{-2}$ at the centre. At the back of the sample, the dislocation densities remain constant at around $5 \times 10^{12}\, m^{-2}$.

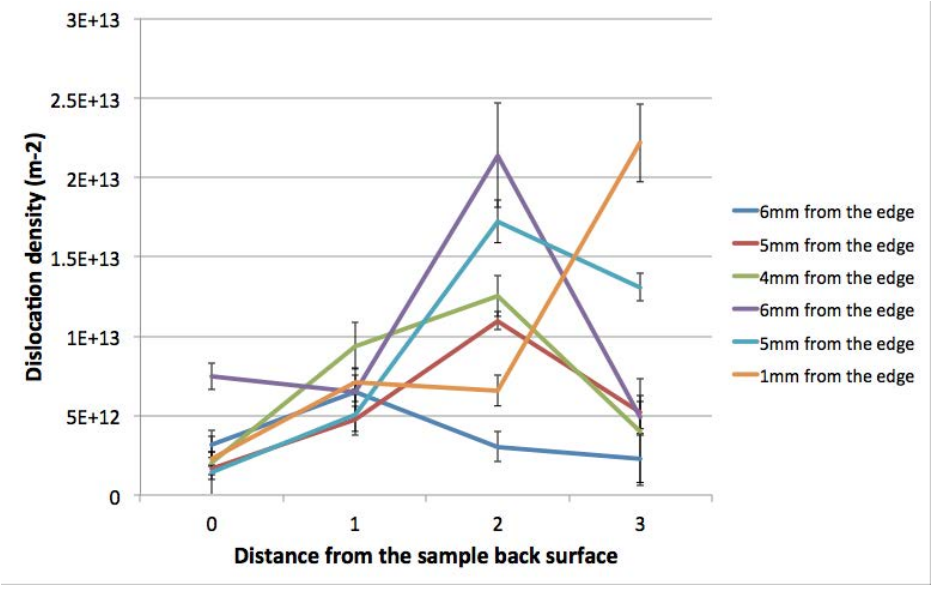


Figure 5.46: Dislocation density distribution in sample [111]

## 5.4 Summary of the defect distribution in the Ta single crystals

The distributions of defects in the three different orientation single crystals are summarised in Figure 5.47. The defect distributions in the three samples are symmetrical around the central axis. Therefore the (110) cross section for the [001] sample, $(0\bar{1}1)$ for [011] and $2\bar{1}\bar{1}$ for the [111] sample are symmetrical around the central line. The diagram at the top of Figure 5.47 shows the twinning distribution; the bottom one shows the dislocation distribution. The shock loading direction is from the top to the bottom of the figure. The distribution of twins inside the single crystals can be divided into three different zones. Zone (1) is the sample front surface. The cross section of each sample consists of a zone (2) and a zone (3), which have different

twinning types and area fractions. The pattern in the dislocation distribution diagram roughly shows the dislocation density distribution: high at the front surface and low at the back surface. The regions labelled (4) and (5) are the positions of the TEM observation areas A and B in Figure 5.21.

The distribution of the defects inside the three single crystals is summarised further below.

### 5.4.1 Voids

- Clusters of voids are observed in every specimen, with total dimensions as shown in Table 5.3. They all located $\sim 1\,mm$ from the sample shock interface.

Table 5.3: The dimensions of the void clusters in the tantalum single crystals

| | Width (mm) | Thickness (mm) |
|---|---|---|
| 001 | 3 | 0.2 |
| 011 | 6 | 0.5 |
| 111 | 5 | 0.5 |

- The voids in [011] and [111] samples are elongated along the direction of the nearby twins. The voids in [001] sample are circular and not related to the twin direction.

### 5.4.2 Twinning

- The twinning distribution in the single crystal specimens is summarised in Table 5.4.

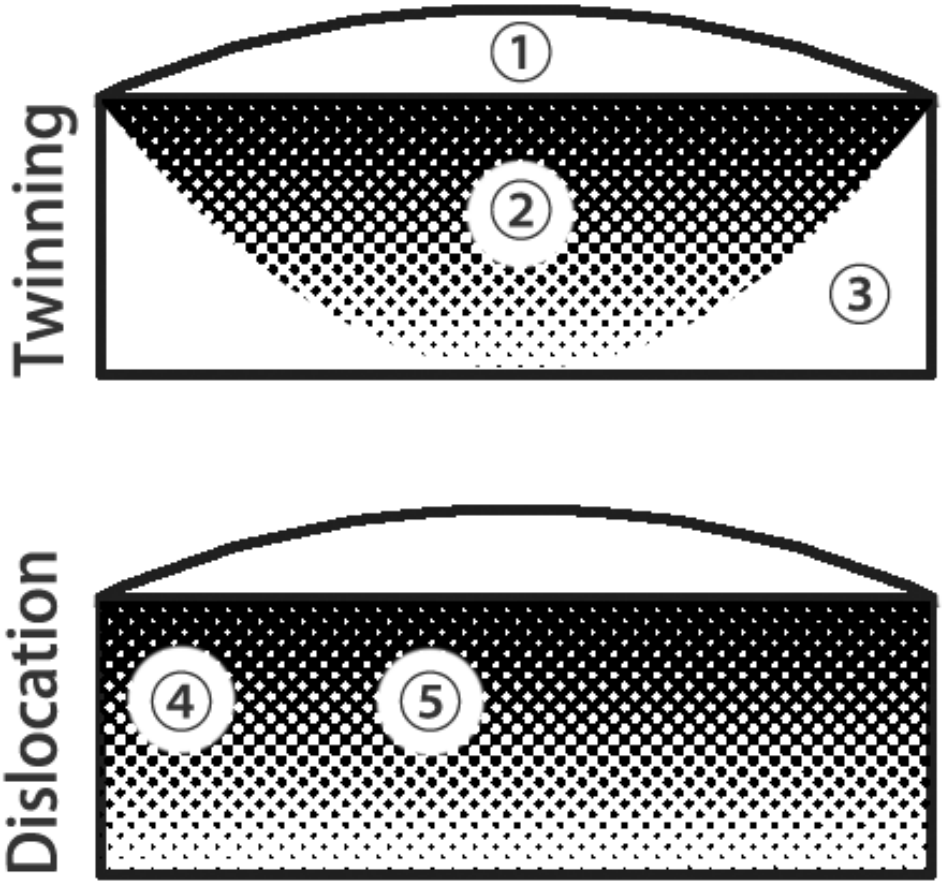


Figure 5.47: The summary of the defect distributions in the tantalum single crystals. The label (1)-(3) represent the twinning distribution, the label (4)-(5) represent the area of TEM observation.

Table 5.4: Summary of the twinning distribution in the shocked single crystals

| | Zone (1) | | Zone (2) | | Zone (3) | |
|---|---|---|---|---|---|---|
| Sample | Twinning plane | Comment | Twinning plane | Comment | Twinning plane | Comment |
| [001] | $(2\bar{1}1)$, (211), (121), $(\bar{1}21)$, $(2\bar{1}\bar{1})$, $(21\bar{1})$, $(12\bar{1})$, $(\bar{1}2\bar{1})$ | Twinning-free at centre. | $(2\bar{1}1)$, (211), (121), $(\bar{1}21)$, $(2\bar{1}\bar{1})$, $(21\bar{1})$, $(12\bar{1})$, $(\bar{1}2\bar{1})$ | 0-0.1 mm under front surface: twinning free; 0.1-4 mm area decreases with distance from front surface. | $(\bar{1}2\bar{1})$ | Only one type of twin. |
| [011] | (211), $(\bar{2}11)$ | Homogeneously distributed over front surface. | (211), $(\bar{2}11)$ | No twinning free region; area decreases with distance from front surface. | $(\bar{2}11)$ | Only one type of twin. |
| [111] | (112), (121), (211) | Homogeneously distributed over front surface. | (112), (121), (211) | No twinning free region; area fraction decreases with distance from front surface. | (121) | Only one type of twin. |

### 5.4.3 Dislocations

- The dislocation density measured using ECCI is around $10^{13}\, m^{-2}$ close to the impact interface. It decreases with distance away from the shock interface becoming $\sim 0.5 \times 10^{13}\, m^{-2}$ at the back surface.

- The dislocation density is generally higher at the sample edge than in the centre (especially at the front surface of the [001] and [111] samples).

- From the TEM observations, the dislocations in area (5) of Figure 5.47 (close to the sample centre) are heavily tangled. In the less tangled area most dislocations are near screw type. The dislocations in region (4) form into dislocation walls (elongated dislocation cells). The dislocation walls in the [001] and [011] samples are parallel to the shock loading direction. The dislocation walls in the [111] sample are parallel to the crystallographic directions [101] or [121].

- In the [111] sample, all the four available Burgers vectors are observed in the TEM image. In area (4) of the [011] sample, only $\frac{1}{2}\left[111\right]$ and $\frac{1}{2}\left[\bar{1}11\right]$ are found in the spaces between the dislocation walls. In area (5) of [011] sample, all

the four Burgers vectors are activated. The dislocations in the [001] sample all have Burgers vectors $\frac{1}{2}[\bar{1}11]$ or $\frac{1}{2}[1\bar{1}1]$.

# Chapter 6

# Discussion

## 6.1 Equation of state of Ta

According to the literature the shock coefficient of tantalum is as shown in Table 6.1.

Table 6.1: The shock coefficient of tantalum

| | C | S |
|---|---|---|
| Ta | 3.293 | 1.307 |

Using the equation of state (Equation 2.1), with free surface velocity 214 $m\ s^{-1}$ and material density 16.69 $g\ cm^{-3}$, the shock pressure in the specimen is calculated to be 6.13 $GPa$. The material yields at free surface velocities 126$m\ s^{-1}$, 82 $m\ s^{-1}$, 120 $m\ s^{-1}$ and 75 $m\ s^{-1}$ for [001], [011], [111] and the polycrystalline sample. The corresponding Hugoniot elastic limits (HEL) are 3.37$GPa$, 2.23$GPa$, 3.08$GPa$ and 2.09$GPa$. Figure 6.1 shows these results compared with the theoretical calculation of the elastic precursor decay in tantalum by Gillis [67]. The HEL of the polycrystalline

specimen fits onto the curve perfectly. The HELs of the single crystals are all higher than that of the polycrystal sample. This is consistent with Razorenov's results, in which the HEL of the coarse grained tantalum is significantly higher than that of the ultra-fine grain tantalum [31]. Normally in quasi-static deformation, the grain boundaries are a hardening feature which can block the movement of the dislocations. However, the dynamic yielding in shock loading phenomena is controlled by the initial mobile dislocation density (available slip systems) [16] [67]. The grain boundaries here in the polycrystalline specimen can act as dislocation source in plastic deformation [66]. Therefore even with the same initial dislocation density, the polycrystal sample has more initial mobile dislocation sources than the single crystals (which have no grain boundary). Also, the single crystals only have a limited number of slip systems. Compared with the polycrystalline sample with grains with different orientations and various available systems, the slip ability of the single crystals is less, and therefore they will only yield at much higher pressure.

The HEL of the single crystals is the stress required for the initial flow of the dislocations. Therefore the HEL is related to the maximum Schmid factor of the crystal. BCC metals are reported as having {110}, {112} and {123} slip planes with slip directions $< 111 >$ [5]. Table 6.2 shows the maximum Schmid factors of these slip systems in the three single crystals.

Table 6.2: The maximum Schmid factors of slip systems in tantalum single crystals

| Specimen \Slip plane | {011} | {112} | {123} |
|---|---|---|---|
| [001] | 0.408 | 0.471 | 0.463 |
| [011] | 0.408 | 0.471 | 0.463 |
| [111] | 0.272 | 0.314 | 0.309 |

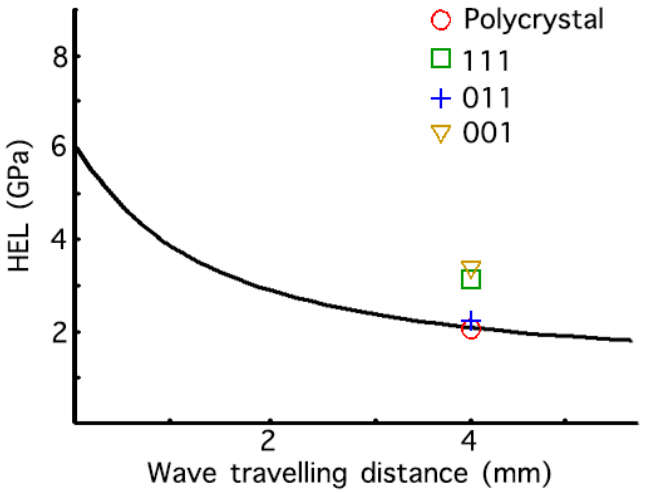


Figure 6.1: The theoretical [67] and experimental elastic precursor decay of tantalum in $6GPa$ shock loading. The HEL measured by HetV of polycrystalline tantalum agrees with the theoretical value. The single crystals have higher HEL than the polycrystalline specimen.

If the principal slip plane {011} [5] of BCC tantalum were operating, the [001] and [011] sample with relatively high maximum Schmid factors should have lower a HEL than the [111] specimen. However, in the shock experiments, the yield point of the [001] sample ($3.37GPa$) is higher than the other two. In quasi-static deformation, either room temperature or low temperature, the [011] loading direction is always the softest orientation (easy slip with low yield stress)[5] [6]. Molecular dynamic simulation performed by Ravelo [68] show that, based on homogeneous dislocation generation, the HEL for [001] sample should be similar to that for [111] sample. However, there is disagreement with the current experiment since the HEL calculated using their model is around $50GPa$, and the theoretical activation pressure calculated for homogeneous nucleation of dislocations is much higher than the pressure in the current condition, i.e. the dislocations in the $6GPa$ shocked specimen are created by normal multiplication mechanisms (e.g. Frank-Read source). From the Burgers vector analysis results presented in the last chapter, only two Burgers vectors are activated in the [001] sample, where all the four Burgers vectors have the same Schmid factor. The HEL in sample [111] could be raised by the limited number of slip systems. This slip system activation will be discussed in more depth in section 6.6.3. The work performed by Ravelo [68] according to the Preston-Tonks-Wallace strength model [69] shows the flow shear stress of [001] loading direction is always higher than the others, because the higher activation energy is high with this loading direction due to the high interatomic potential caused by the high pressure. This is possibly another reason why the [001] sample has significant high HEL.

## 6.2 Wave propagation

To investigate the loading experienced by the material, and to explain the free surface velocity figure, it is convenient to draw an x-t diagram of the sample in the shock experiment. Using Equation 2.1, the shock wave velocity is calculated to be $3432\,m\,s^{-1}$. The velocity of the release wave is often higher than that of the shock wave, but here it is simplified to be equal to the speed of the shock wave. The x-t diagram of the projectile and the specimen is shown in Figure 6.2. The x axis is the distance. $x = 0\,mm$ is the impact interface between the projectile and the specimen. $x = -3\,mm$ is the back surface of the projectile. $x = 4\,mm$ is the back surface of the tantalum specimen. Shock waves are created at the impact interface at time $t = 0\,\mu s$. The shock wave inside the projectile reaches its back surface at time $0.9\,\mu s$, and is reflected as a release wave. The shock wave inside the specimen arrives the back surface of the specimen at time $1.2\,\mu s$. After the material at this back surface is released to 0 pressure, the surface is accelerated to a velocity of $2v_p$, via the mechanism shown in Figure 2.6. This velocity is then detected by the HetV system. The release wave from the projectile back surface arrives at the specimen back surface at time $3\,\mu s$, $1.9\,\mu s$ after the region being compressed. Thus, the duration of this shock loading is $1.9\mu s$. It should be noted that the two release waves (one from the projectile, the other from the specimen) meet at position $x = 1\,mm$, at time $t = 2.1\,\mu s$. The interaction of these two release waves converts them to two tension waves, still moving in their original propagation directions [16]. This tensile stress can generate voids/fracture in the region of the wave interaction [70]. When the tension wave reaches the back surface of the specimen, due to the energy loss

into the voids/fracture, it cannot decelerate the material to zero free surface velocity. This phenomenon can be seen in the HetV profile of the polycrystalline Ta in Figure 5.1. The free surface velocity of the polycrystal Ta starts to decrease at 112.7 $\mu s$, which is 1.7 $\mu s$ after the shock wave. This loading duration is slightly shorter than the 1.9 $\mu s$ predicted by Figure 6.2, simply because the release wave moves faster than the speed used in the model and therefore it arrives earlier than the prediction. The free surface velocity is reduced to $50 m\, s^{-1}$ gradually over 0.5 $\mu s$: the strain rate is much lower than for the shock wave front due to the release wave dissociation (in the shock release phenomenon, the wave in high pressure moves faster than the wave travelling in lower pressure, the release wave is broadened as it propagate through the material due to the difference in speed. The material then needs longer time to be unloaded: lower strain rate) [16]. The single crystals have the same thickness as the polycrystalline sample. They should have the same loading duration since the shock waves and the back release waves have the same travelling distance. However, in the HetV profile in Figure 5.1, the pulse duration for the single crystals is around $1 \mu s$ shorter, i.e. the release wave in the single crystal arrives 1 $\mu s$ earlier than in the polycrystal sample. The only explanation is that the diameter of the single crystals is a lot smaller than that of the polycrystalline specimen. The lateral release wave can move to the the HetV measuring point (centre of the back surface) just after the material is loaded to the shock pressure. The diameter of the polycrystalline sample is large enough that the release wave has no time to reach the disc back centre before the $'$tension wave$'$ arrives. Therefore in Figure 5.1 it appears that the polycrystalline Ta profile is not influenced by the lateral release wave and agrees

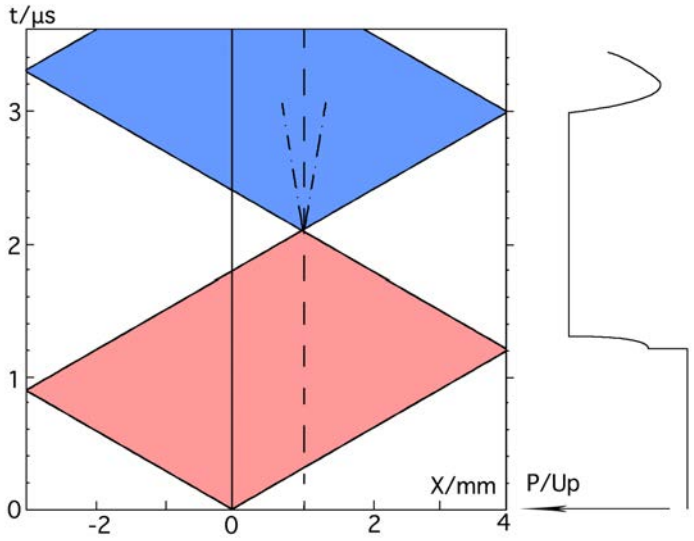


Figure 6.2: The x-t diagram of the wave propagation in the tantalum projectile and specimen. The red area is compressed by the shock waves and the blue area is under tensile stress created by the interaction of the back release waves. See text for detailed explanation.

with the prediction of Figure 6.2.

## 6.3 Simulation of pressure and shear stress in shock loaded specimen

The shock loading experiment on a polycrystalline specimen as the same dimensions with the single crystals (6$mm$ radius, 4$mm$ thickness) was simulated using $ANSYS\,Autodyn$ software by AWE (Atomic Weapons Establishment, UK). Despite the anisotropy of the single crystals, the simulation of the isotropic polycrystalline material should represent reasonably well the shock wave movement inside the sam-

ple. Figures 6.3 and 6.4 show the pressure and maximum shear stress on the centre cross section of the specimen and projectile during the impact. The upper row is the pressure and the bottom row is the shear stress for the same section of the material. Each column represents a different time, from $0.2\,\mu s$ (in graph A) after the collision of the material/projectile surface to $4.6\ \mu s$ (in graph G). The legend of the map changes at each time step to provide a strong contrast. The $X$ and $Y$ axis of each graph are the dimension of the projectile + the shocked specimen. From $-3mm$ to $0mm$, is the projectile. From $0mm$ to $4mm$ is the specimen. The Y axis is the radial distance of the sample disc $0mm$ to $12mm$. The $x = 0$ line is the impact interface of the projectile and the sample. It is kept stationary here as a reference.

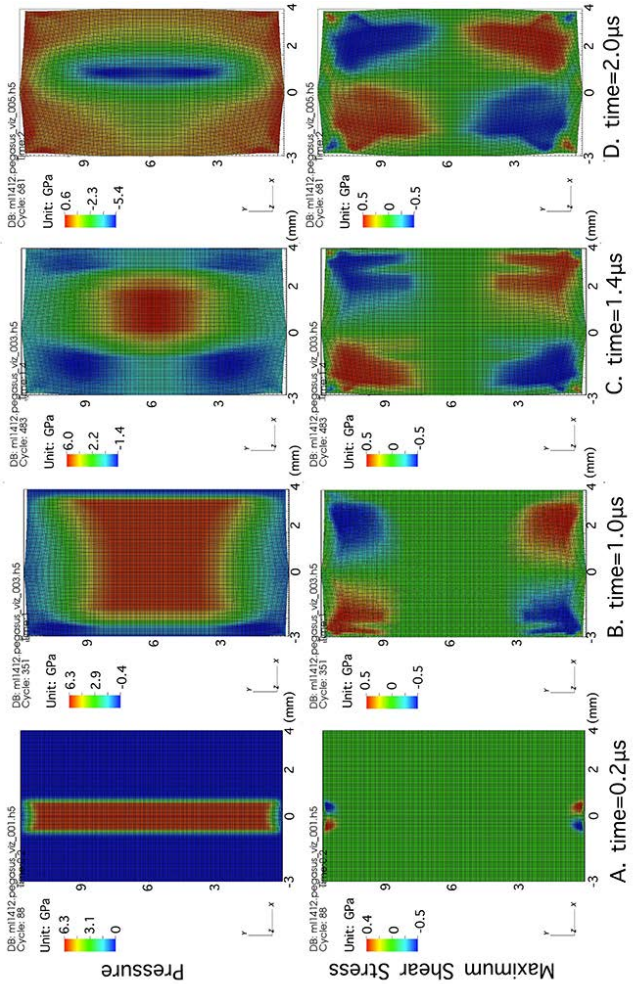


Figure 6.3: Simulation result of the pressure and maximum shear stress in the shock loaded polycrystalline sample over time. The left column is the pressure and the right column is the maximum shear stress.

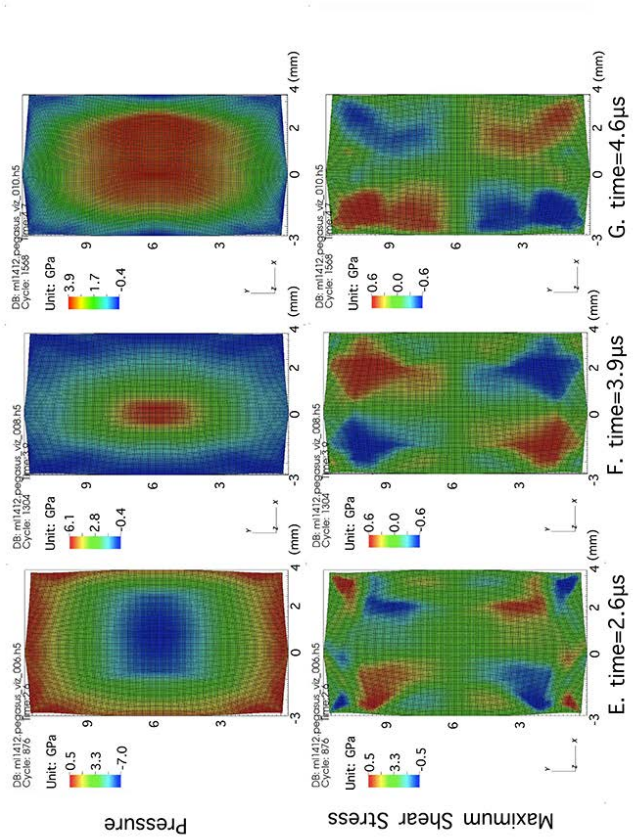


Figure 6.4: Simulation result of the pressure and maximum shear stress in the shock loaded polycrystalline sample over time. The left column is the pressure and the right column is the maximum shear stress.

The projectile and the tantalum specimen meet at $x = 0$ at time 0. At $0.2\,\mu s$ in Figure 6.3-A, two shock wave fronts were generated from the $x = 0$ interface. One of

them moves into the tantalum sample and the other moves into the projectile. The red square zone with high pressure is compressed by the shock wave front. The shock wave in the specimen is at $x = 0.5\,mm$ and in the projectile is at $x = -0.5mm$. Because there is no material at the edge of both objects (the epoxy around the specimen is ignored), there are release waves entering the material from the top and the bottom edges after the shock wave front passes. It can be seen that the material pressure is lowered at the top and bottom of the compressed area. In the shear stress map of A, the zones with high shear stresses (red and blue zones) are caused by the release waves according to the mechanism shown in Figure 2.7. The red shear stress (positive) shears anti-clockwise and the blue one (negative) shears clockwise. In Figure 6.3-B at time $1.0\,\mu s$, the shock wave front in the specimen has almost reached the back surface; meanwhile the shock wave inside the projectile has been reflected from its back surface. The reflected release wave front is at $x = -2\,mm$. It can be seen that the material at the back surface of the projectile has been released to nearly $0\,GPa$. Because the release wave moves faster in the compressed zone than in the material at low pressure, the reflected release wave at the back surface has spread from the area $x = -3\,mm$ to $x = -2\,mm$. The lateral release wave from the edge moves into the material further than in graph A. The green zone close to the edge represents the pressure gradient from $6GPa$ to ambient pressure. In the map of shear stress, the zones visited by the lateral release wave see high shear stresses, but with the same shear direction as those in shear map A. They now move (B) with the shock wave front to the back surface of the specimen. In the projectile, the shape of the high-shear zone has been changed by the reflected release wave from the back

surface of the projectile. The shear zones both have two "arms". The "arm" close to the free surface is caused by the interaction between the reflected back release wave and the area that has been released by the lateral release wave (half of the width at this point): the particle velocities of the area released by the lateral release waves are in the lateral direction; the particle velocity of the material released by the back release wave is in the same direction as the shock wave (in this case towards the left side). The ′obliquity′ of those two velocities is the origin of the high shear stress zone (the "arm" on the left side). It should be noted that the corresponding area in the pressure map B of the left "arm" has a negative pressure. This indicates that the material here is under tensile stress, which is produced by the interaction between the back release wave and the area that have a lateral particle velocity. This point corresponds to time $t = 1.2\,\mu s$ in Figure 6.2 and $111\,\mu s$ in Figure 5.1, when the wave arrives at the specimen back surface and the material starts to be accelerated and its speed detected by the HetV.

At $1.4\,\mu s$ - in Figure 6.3-C - the red area in the centre of the pressure map is the material still under compression. The shock wave in the impacted specimen has bounced back from the free specimen back surface and form a release wave at position $x = 2\,mm$. The blue area (tensile stress) between $x = 2\,mm$ and $x = 3\,mm$ is formed by the interaction between the back release wave and the radial release waves. It can be seen that in the shear map C, the high-shear zone also has two "arms", which suggests the same mechanism as at the back surface of the projectile in B. At the same time, in the projectile the negative pressure zone has expanded with the release wave front to the position of $x = 0$. It can be seen that the high-

shear areas in the shear map still correspond to the tensile stressed area in the pressure map. According to Figure 6.2, the release wave front has now moved to position $x = 2.5mm$ and the material at $x = 4mm$ has been released to zero pressure and has a velocity of $212\, m\, s^{-1}$. This is consistent with the HetV result in Figure 5.1: when the time $t = 111.5\, \mu s$, the free surface velocity is equal to $212\, m\, s^{-1}$.

When the two release waves from the back surface from both the specimen and projectile meet at time $3.0\mu s$ and position $x = 1$, they create an area with very high tensile stress ($-5.4GPa$ pressure). The direction of the tensile stress is along the back release waves propagation direction. At the same time, at the corners of the specimen/projectile combination, as a response to the leaving of the release waves, compression waves of $0.6\, GPa$ enter the material, appearing as red at the edges and the back surfaces. Because of the interaction of the compression wave from the back surface with the radial wave, the corners of the specimen + projectile are shear stressed in opposite senses. This can be seen in the shear map D, where the small regions at the corners have shear stresses with different signs from the large shear zones created by the release waves. This phenomenon corresponds to a time $1.8\, \mu s$ in Figure 6.2, where the release waves are both close to $x = 1$ but have not yet met. This is because the actual movement of the release waves is faster than the shock wave front (which is assumed to be equal to the release wave velocity in the Figure 6.2), and their interaction happens earlier than predicted. Looking back to the HetV in Figure 5.1 at time $112\, \mu s$, the material at the back surface is decelerated by around $50\, m\, s^{-1}$, due to the effect of the lateral release wave. This can be seen from the shear stress map: the lateral release wave has already arrived

at the specimen back centre.

The pressure and shear maps between $2.6\,\mu s$ and $4.6\,\mu s$ are shown in Figure 6.4. At $2.6\,\mu s$ the tensioned area in the middle expands with the release waves to a region between $x = -1.5\,mm$ and $x = 2\,mm$. The re-compression wave at the free surfaces continues to move into the material, and the high shear stresses at the corners start to expand, as shown in the shear map E. As predicted by Figure 6.2, the pull-back release is approaching the specimen back surface at time $2.6\,\mu s$. It can be seen from time $t = 112.6\,\mu s$ in Figure 5.1 that the slope of the free surface velocity undergoes a change, suggesting that the material is influenced by the back release wave instead of by the lateral release wave. This can be confirmed from the polycrystalline Ta profile, at $112.6\mu s$ the polycrystalline sample is starting to be decelerated by the back release wave.

The back release waves keep moving to the free surface, are reflected by them, form two compression waves and meet again at time $3.9\mu s$. From the shear map it can be seen that the shear direction in the specimen has been totally reversed. For example, the top side of the specimen was sheared negatively (clockwise) from $0.2\,\mu s$ to $2.0\,\mu s$ in graph D. It is now sheared positively (anti-clock wise) at $3.9\mu s$.

In the rest of the simulation, the waves circulate inside the specimen and gradually attenuate. In Figure 6.4-G, the maximum pressure inside the material has decreased to $3.9\,GPa$ at the end of the simulated time $4.6\,\mu s$; the sign of the shear stress in the specimen changed again. It could be inferred that the wave pressure continue to attenuate and finally go down to zero. The sign of the shear stress will change a few times more before the waves totally fade away or are absorbed when

the specimen hits the material inside the shock loading chamber.

The simulated pressure of the centre area of the specimen generally agrees with the analysis in Figure 6.2. For the edge area, the region in the range $0 < y < 3mm$ and $9 < y < 12mm$ of the radial distance only experiences once high pressure compression as the shock front passed by. In the rest of the time, this area is mainly stressed by a high shear stress whose sign changes rapidly. The central part of the specimen ($3 < y < 9mm$) experiences a high compression-high tension cycle, without very high shear stresses.

## 6.4 Spallation and voids

It is found that in all the single crystal samples, clusters of voids are created by the shock wave. In the HetV free surface profile, it can be seen that the material is not fully decelerated to zero velocity which suggests that spallation takes place [16] [10] [70]. In a shock loading experiment, voids or fracture are usually created by the interaction of back release waves (from the free back surfaces of the projectile and specimen). The void clusters in the three single crystals are all around $1mm$ beneath the impact interface. Referring to the wave propagation diagram Figure 6.2, $x = 1\,mm$ is where the two release waves interact for the first time (at $t = 2.1\,\mu s$). Therefore the void clusters are generated by the tensile stress formed by the two back release waves:

$$\sigma_{sp} = \frac{1}{2} * \rho_0 C_0 \Delta U \tag{6.1}$$

Because the current experiment is not a standard 1-D shock experiment, the HetV measurement is influenced by the lateral release wave. It is impossible to extract the material spall strength to compare with the literature. However, the ′relative′ spall strength can be calculated according to Equation 6.1 [10]. The result is shown in Table 6.3.

Table 6.3: Relative spall strength of the three tantalum single crystals

| | Relative Spall Strength (GPa) |
|---|---|
| 001 | 5.7 |
| 011 | 4.9 |
| 111 | 5.2 |

It seems that the [001] direction is stronger with respect to the tension created by the release wave interaction. The release suffers a minor energy loss from the plastic deformation for creating the void clusters, i.e. the plastic deformation for the void growth in the sample (001) is smaller than the other two because the total dimension of the cluster in the [001] sample is much smaller than in [011] and [111].

The void clusters generated in the Ta single crystals are a type of ductile fracture. The creation of a ductile fracture often consists of three stages: (1) voids nucleate at second phase particles/ grain boundaries/ twin boundaries, (2) void growth and (3) void coalescence [71] [72] [73]. From Figure 5.10, 5.14 and 5.18 it can be seen that sample 001 is still in phase (2) since coalescence is not yet observed: most of the voids in this specimen have circular or elliptical shape. The voids in the [011] and [111] sample show an elongated morphology, with the long axis parallel to the twinning. Some of the long void cluster consists of bubbles connected together, like the cluster on the very left of Figure 5.14, or the right side of Figure 5.18. This

indicates that samples [111] and [011] is in phase (3): void coalescence. There are 2 possible reasons one can think of why the voids are parallel to the twin. (1) The twin deformation acts as a very important mechanism in the growth of the voids. This will make the voids to grow in the direction of the twins. (2) twins are already generated in the region $1\,mm$ beneath the sample impact surface ($x = 1\,mm$) before the two release waves create a tensile stress here. When the voids are nucleated (possibly at the pre-existing twin boundary), a micro-crack grows along the boundary, causing the final voids to lie in the same direction as the twins. (3) Figure 6.4 shows a third possible model for the void cluster formation. In sketch (a), the voids nucleate on multiple points on the twin boundary. They start to grow and approach each other in sketch (b). When they coalesce, the twins in between are very thin and are broken immediately by the tensile stress, the whole cluster opens up, and forms the void morphology in sketch (c), which seems very similar to the voids in samples [011] and [111] in Figures 5.14 and 5.18.

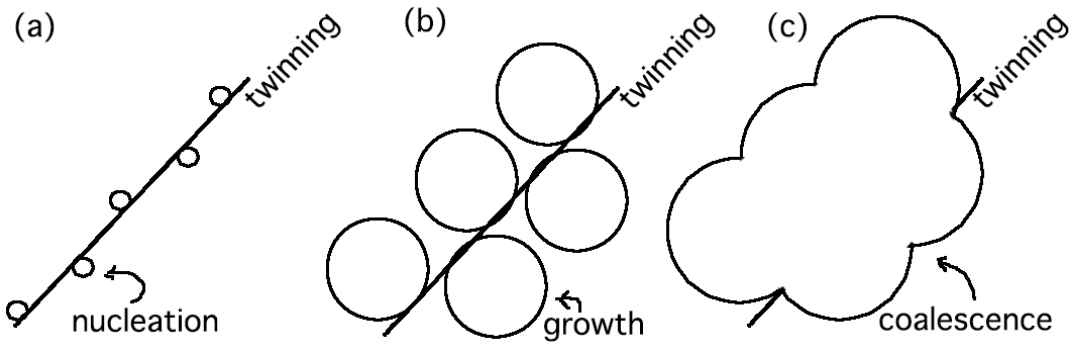


Figure 6.5: The mechanism of the void growing into cluster parallel to twinning direction

Molecular dynamics simulation of void growth in Ta shows that twinning become an active mechanism for void growth only when the tensile strain rate is higher than $10^9 s^{-1}$, which corresponds to a shock pressure of $20GPa$ [74]. This means that twinning should not be active in void growth at $6GPa$. Laser shock experiments on Ta $(10-70GPa)$ by Lubarda [75] indicate that void growth over this pressure range is assisted mainly by dislocation glide. Therefore the (1) hypothesis above should not be the reason for the current void morphology.

The second hypothesis makes the orientation of the void clusters parallel to the twinning plane. However, this mechanism should lead to a crack-like shape of the voids. The edge of the voids would be very straight. This is different from the SEM observations.

Much of the SEM evidence supports model (3). Figure 5.20 shows SEM BSE image of typical void morphology in [111] and [011] sample. Figure 5.20-a shows a

lot of small voids on a deformation twins in the [111] sample. It is found that almost all the small voids are connected to a twin, suggesting that the onset of these voids is at the twinning boundary.

Figure 5.20-b shows a cluster of connected voids lying in the $[\bar{2}11]$ direction. A very long twin penetrates the whole cluster along the long axis. The centre of some voids is connected to a (211) twin. The voids are possibly nucleated at the junctions of the (211) and $(\bar{2}11)$ twins, grow and link together to form an elongated cluster as shown in Figure 5.20-b.

In summary:

- Voids are created by the release wave interaction at $x = 1\,mm$ and time $2.1\mu s$ in all the tantalum single crystals.

- Voids in the [011] and [111] samples nucleate at the twin boundaries, grow and link together to form an elongated cluster parallel to the twins. This is not obvious in sample [001].

- The spall strength of [001] is greater than that of [011] and [111]. The total cluster size in [001] is much smaller than the other two. This will be discussed in section 6.5.2.

- Twinning in the [011] and [111] samples occurs before ductile fracture (i.e. before $2.1\,\mu s$ in Figure 6.2). This will also be discussed in section 6.5.2.

## 6.5 Twinning

### 6.5.1 The relationship between twinning plane and stress

#### Area (2): centre and front part of the specimens

In the last section it was suggested that the twins in area (2) (Figure 5.47) of the [011] and [111] samples are created between $0 - 2.1\mu s$ (see Figure 6.2). This means that the twinning shear in area (2) of the [011] and [111] samples is driven by the uniaxial stress produced by the shock wave front. It would be therefore helpful to calculate the shear stress on the twinning plane to confirm this hypothesis. In the simulation discussed in section 6.3, the centre area of the sample is mainly stressed by high pressure without a very high shear stress. This area largely overlaps with area (2) in the twinning distribution map. Therefore the dominant stress in area (2) is the shock compression stress. To simplify the calculation, these stresses are written as an uniaxial stress with the loading direction along the z axis:

$$\sigma = \begin{pmatrix} 0 & 0 & 0 \\ 0 & 0 & 0 \\ 0 & 0 & \sigma_{zz} \end{pmatrix}$$

In this calculation $\sigma_{(zz)}$ is set to one. When the stress is compressive, $\sigma_{zz} = 1$ and when the stress is tensile $\sigma_{zz} = -1$. This stress is set to be in a coordinate system $A$ with $x$ axis parallel to [100], $y$ parallel to [010] and $z$ parallel to [001]. To calculate the stress on the twinning plane in the twinning shear direction, the stress tensor $\sigma$ in coordinate system $A$ can be related to a coordinate system B which the

$x$, $y$ and $z$ axis parallel to the twin axis, the shear direction and the twinning plane normal, respectively. For example, the $x$, $y$ and $z$ axis of coordinate system B for a $[111](11\bar{2})$ twinning system is $[1\bar{1}0]$, $[111]$ and $[\bar{1}\bar{1}2]$. The stress tensor $\sigma_{twin}$ in coordinate system B can be written as:

$$\sigma_{twins} = M \cdot \sigma \cdot M^T \tag{6.2}$$

where $M$ is the rotation matrix from coordinate $A$ to coordinate $B$. $\sigma_{zy}$ in $\sigma_{twins}$ is the shear stress on the twinning plane in the twinning shear direction. For example, the stress in coordinate system B for the twinning system $(211)[\bar{1}11]$ with a uniaxial stress of 1 in the [011] direction is:

$$\sigma_{twin} = \begin{pmatrix} 0 & 0 & 0 \\ 0 & 0.667 & 0.471 \\ 0 & 0.471 & 0.333 \end{pmatrix}$$

The number 0.471 is the shear stress experienced by this twinning system. This means that with a unit stress in the [011] loading direction, the shear stress on the twinning shear direction for the (211) twin in the [011] sample is 0.471. The positive value means that the shear is in the positive-twinning direction. For a 6.13 $GPa$ shock stress, the shear stress on this (211) twinning would be 2.89 $GPa$. This is obviously much higher than the yield stress of tantalum. But the calculated shear stress can be used to compare the shear stresses experienced by different twinning systems. The system with highest $\sigma_{zy}$ would normally be expected to be activated. $\sigma_{zy}$ for all the twinning systems in the single crystals is shown in Table 6.4.

Table 6.4: The $\sigma_{zy}$ for twinning systems in the tantalum single crystals under shock compression

| 001 | | | 011 | | | 111 | | |
|---|---|---|---|---|---|---|---|---|
| Twinning plane | Shear direction | $\sigma_{zy}$ | Twinning plane | Shear direction | $\sigma_{zy}$ | Twinning plane | Shear direction | $\sigma_{zy}$ |
| 211 | $\bar{1}11$ | 0.236 | 211 | $\bar{1}11$ | 0.471 | 211 | $\bar{1}11$ | 0.314 |
| $21\bar{1}$ | $\bar{1}1\bar{1}$ | 0.236 | $21\bar{1}$ | $\bar{1}1\bar{1}$ | 0 | $21\bar{1}$ | $\bar{1}1\bar{1}$ | -0.157 |
| $2\bar{1}1$ | $\bar{1}\bar{1}1$ | 0.236 | $2\bar{1}1$ | $\bar{1}\bar{1}1$ | 0 | $2\bar{1}1$ | $\bar{1}\bar{1}1$ | -0.157 |
| $1\bar{2}1$ | 111 | 0.236 | $1\bar{2}1$ | 111 | -0.236 | $1\bar{2}1$ | 111 | 0 |
| $12\bar{1}$ | $1\bar{1}\bar{1}$ | 0.236 | $12\bar{1}$ | $1\bar{1}\bar{1}$ | -0.236 | $12\bar{1}$ | $1\bar{1}\bar{1}$ | -0.157 |
| $1\bar{1}\bar{2}$ | $1\bar{1}1$ | -0.471 | $1\bar{1}\bar{2}$ | $1\bar{1}1$ | 0 | $1\bar{1}\bar{2}$ | $1\bar{1}1$ | -0.157 |
| $1\bar{2}\bar{1}$ | $11\bar{1}$ | 0.236 | $1\bar{2}\bar{1}$ | $11\bar{1}$ | 0 | $1\bar{2}\bar{1}$ | $11\bar{1}$ | -0.157 |
| $11\bar{2}$ | 111 | -0.471 | $11\bar{2}$ | 111 | -0.236 | $11\bar{2}$ | 111 | 0 |
| $1\bar{1}2$ | $1\bar{1}\bar{1}$ | -0.471 | $1\bar{1}2$ | $1\bar{1}\bar{1}$ | -0.236 | $1\bar{1}2$ | $1\bar{1}\bar{1}$ | -0.157 |
| 112 | $11\bar{1}$ | -0.471 | 112 | $11\bar{1}$ | 0 | 112 | $11\bar{1}$ | 0.314 |
| 121 | $1\bar{1}1$ | 0.236 | 121 | $1\bar{1}1$ | 0 | 121 | $1\bar{1}1$ | 0.314 |
| $\bar{2}11$ | 111 | 0.236 | $\bar{2}11$ | 111 | 0.471 | $\bar{2}11$ | 111 | 0 |

The twinning planes of the systems with the highest $\sigma_{zy}$ in the [001] sample are $(2\bar{1}1)$, (211), (121), $(\bar{1}21)$, $(2\bar{1}\bar{1})$, $(21\bar{1})$, $(12\bar{1})$ and $(\bar{1}2\bar{1})$, which all have a normalised shear stress of 0.236. These twins are all found in area (2) of the [001] sample, as shown in Table 5.4. When the interaction of the back release waves creates the tensile stress, the positive $\sigma_{zy}$ in Table 6.4 becomes negative and the negative ones become positive. This will favour the twinning on plane $(1\bar{1}\bar{2})$, $(11\bar{2})$, $(1\bar{1}2)$ and (112). However these twins are not found in the [001] sample, which suggests that the ability to produce twins of the tensile wave is weaker than that of the shock wave front. The model proposed by Meyers suggests that the onset of twinning is affected by the sensitivity of the dislocation flow stress to the strain rate [32]. As shown in Figure 2.14, when the dislocation flow stress is raised above the twinning activation stress, the major deformation mechanism of the material transfers from dislocation slip to twinning. Using the Swegle-Gradly relationship for Ta reported by Murr [27], the relationship between the shock pressure and the material strain

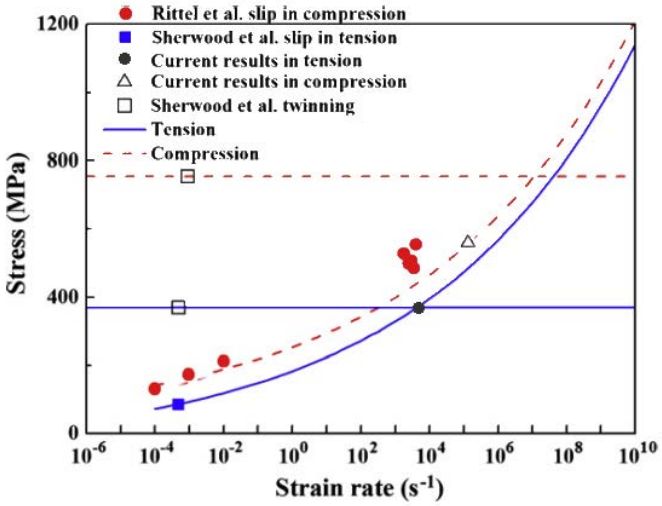


Figure 6.6: Flow stress-strain rate curves for [001] tantalum single crystal in tension (solid lines) and compression (dashed lines) [28]

rate is:

$$\dot{\epsilon} = 27.34 \times 10^{-36} \times P^4 \tag{6.3}$$

where $P$ is the shock loading pressure. The resulting strain rate of the material plastic deformation at the shock front is $2.3 \times 10^5 s^{-1}$. The strain rate of the release wave can be calculated from the HetV profile. The material is released to near ambient pressure in around $1\,\mu s$. This means that the strain rate of the release wave at the back surface is around $3 \times 10^3 s^{-1}$. These strain rates can be put in the dislocation flow stress figure to compare them with the activation shear stress for twinning. Figure 6.6 [37] shows the stress required for activating dislocation/twinning plot against the strain rate of [001] single crystal tantalum with the data from the current study superimposed as solid circles (tension) and empty triangles (compression).

The red circles and blue squares are the experimental results of Rittel [76] and Sherwood [77] respectively. The horizontal lines are the activation shear stress for twinning nucleation. They are from the twinning shear stress results of Sherwood [77]. The activation shear stress of twinning is considered to be independent of the strain rate [32] [28]. The exponential rising curve is the flow stress for the dislocations. It can be seen that Rittel's compression test results are a little higher than the prediction from Sherwood's experiments. This is due to the interstitial element difference of the materials [28]. The calculation of the flow stress in compression shows that the dislocation flow stress in the shock front of the current experiment is around $600\,MPa$, which is lower than the shear stress required for twin activation. However, twinning is created by the shock wave front in the [011] and [111] specimens. For the [001] sample the origin of twinning is not obvious looking from the morphology of the voids fracture, but the $\sigma_{zy}$ of the activated twinning systems occurred in area (2) of this sample fit well with the stress calculations in Table 6.4. Therefore it is highly possible that they are also created by the shock wave front. The reason why the twinning activation stress is higher than the dislocation flow stress calculation is probably the effect of the interstitial elements on the dislocations. If the dislocation flow stress were to increase faster with the strain rate, it might become higher than the twinning activation stress for a strain rate of $2.3 \times 10^5 s^{-1}$ (current experiment). And, therefore, lead to the generation of deformation twinning.

In Table 6.4, the twinning planes with high resolved shear stress $\sigma_{(zy)}$ in 011 are (211) and ($\bar{2}$11). For the [111] sample they are (112), (121) and (211). The twins in area (2) of [011] and [111] sample have by the exact same plane, as shown in Table

5.4. Similar to the [011] specimen, the twins in area (2) of these two samples are both created by the shock wave front.

**Area (3): bottom edge part of the specimens**

Area (3) in Figure 5.4 has a different twin distribution from area (2) in all the three single crystal specimens. The simulation results show that this area suffers mainly high shear stresses (with rapidly changing sign). It is easy to understand that the highest shear stress is created by the obliquity of the shock wave front and the lateral release wave since they have the highest difference in particle velocity in the shock impact phenomenon. To investigate the effect of the release wave obliquity on the twin nucleation, the shear stress of the lateral release wave is simplified to:

$$\sigma_{lateral} = \begin{pmatrix} 0 & 0 & 0 \\ 0 & 0 & 0 \\ 0 & \sigma & 0 \end{pmatrix} \tag{6.4}$$

Using Equation 6.2, the stress on the twinning system in the shear direction of twinning can be calculated. The result is shown in Table 6.5, with $\sigma$ set equal to unity. The positive $\sigma_{zy}$ stress means that the stress applied to the twinning system by the pure shear stress $\sigma_{lateral}$ favours twin nucleation.

The twins in area (3) of the [001], [011] and [111] samples are $(\bar{1}2\bar{1})$, $(\bar{2}11)$ and (121), respectively. The respective $\sigma_{zy}$ are 0, 0.333 and $-0.770$. They are not the twins which experience the highest shear stress. For the $(\bar{1}2\bar{1})$ twin in the [001] sample, the resolved shear stress is 0. This means there is zero stress helping

Table 6.5: The $\sigma_{zy}$ for twinning systems in the area (3) of tantalum single crystals under lateral release wave

| 001 | | | 011 | | | 111 | | |
|---|---|---|---|---|---|---|---|---|
| Twinning plane | Shear direction | $\sigma_{zy}$ | Twinning plane | Shear direction | $\sigma_{zy}$ | Twinning plane | Shear direction | $\sigma_{zy}$ |
| 211 | $\bar{1}11$ | -0.333 | 211 | $\bar{1}11$ | -0.333 | 211 | $\bar{1}11$ | 0 |
| $21\bar{1}$ | $\bar{1}1\bar{1}$ | 0.333 | $21\bar{1}$ | $\bar{1}1\bar{1}$ | 0 | $21\bar{1}$ | $\bar{1}1\bar{1}$ | 0.385 |
| $2\bar{1}1$ | $\bar{1}\bar{1}1$ | 0 | $2\bar{1}1$ | $\bar{1}\bar{1}1$ | 0 | $2\bar{1}1$ | $\bar{1}\bar{1}1$ | -0.385 |
| $1\bar{2}1$ | 111 | 0 | $1\bar{2}1$ | 111 | -0.167 | $1\bar{2}1$ | 111 | 0 |
| $12\bar{1}$ | $1\bar{1}\bar{1}$ | -0.333 | $12\bar{1}$ | $1\bar{1}\bar{1}$ | 0.167 | $12\bar{1}$ | $1\bar{1}\bar{1}$ | 0 |
| $1\bar{1}\bar{2}$ | $1\bar{1}1$ | -0.667 | $1\bar{1}\bar{2}$ | $1\bar{1}1$ | -0.5 | $1\bar{1}\bar{2}$ | $1\bar{1}1$ | 0.385 |
| $1\bar{2}\bar{1}$ | $11\bar{1}$ | 0 | $1\bar{2}\bar{1}$ | $11\bar{1}$ | -0.5 | $1\bar{2}\bar{1}$ | $11\bar{1}$ | -0.385 |
| $11\bar{2}$ | 111 | 0 | $11\bar{2}$ | 111 | -0.167 | $11\bar{2}$ | 111 | 0 |
| $1\bar{1}2$ | $1\bar{1}\bar{1}$ | 0.667 | $1\bar{1}2$ | $1\bar{1}\bar{1}$ | 0.167 | $1\bar{1}2$ | $1\bar{1}\bar{1}$ | 0 |
| 112 | $11\bar{1}$ | 0 | 112 | $11\bar{1}$ | 0.5 | 112 | $11\bar{1}$ | 0.770 |
| 121 | $1\bar{1}1$ | 0.333 | 121 | $1\bar{1}1$ | 0.5 | 121 | $1\bar{1}1$ | -0.770 |
| $\bar{2}11$ | 111 | 0 | $\bar{2}11$ | 111 | 0.333 | $\bar{2}11$ | 111 | 0 |

this type of twin to nucleate. The $(1\bar{1}2)$ twin which experiences the highest shear stress is not, however, generated. Things are similar in area (3) of the [011] and [111] specimens. In the [011] sample the twinning influenced by the lateral release wave have the second highest $\sigma_{zy}$: 0.333, lower than the highest 0.5. In the [111] sample the twins activated in area (3) have negative $\sigma_{zy}$. This violates the law of CRSS. Twinning behaviour in body-centred cubic materials is very sensitive to the orientation of the applied stress [78]. $\sigma_{lateral}$ in Equation 6.4 is only a simplified model of the lateral release wave. The actual stress tensor might be different from this model and give a different preference for the twinning plane activation. From the overview of the specimen cross sections, the twins in area (3) are all activated in the area (2), which is dominated by the compression shock wave front. Thus it can be assumed that the all the twinning systems generated in the area (2) are nucleated in the area (3) by the shock wave front (since they appear in area (2), which is mainly influenced by the shock wave front). But the growth of most systems

is stopped by the lateral release wave, which arrives very soon after the shock wave front (less than 1 $\mu s$). Only one type of twin in each sample is driven by the stress of the lateral release wave.

### 6.5.2 Area fraction of twinning

Besides the difference in twin type between areas (2) and (3), another significant feature of the twinning distribution is that the twin area fraction decreases with distance from the sample front surface. Over the time period of the shock wave compression, the material in area (2) of all the specimens experienced the same compression pressure of 6.13 $GPa$ and according to the simulation results presented in section 6.3, this area is not strongly influenced by the lateral release wave over the time of the twin nucleation. Therefore, there are only two reasons that can possibly cause the differences in twinning area fraction: (1) The difference in the shock loading duration; (2) The elastic precursor decay.

The difference in the shock loading duration is caused by the movement and reflection of the shock wave. Since area (2) is influenced in a minor way only by the lateral release wave, the wave can be represented using Figure 6.2. It can be seen that the material in the $0-1mm$ area is loaded by the shock wave front, and released by the back release wave from the projectile. The material in the $0-1\,mm$ have the same loading duration of 1.9 $\mu s$. The material in the range $1-4\,mm$ is loaded by the shock compression for a different period of time. The material at position $x = 2\,mm$ has a lower loading duration, because the material is unloaded by the back release wave (from the specimen back surface), which arrives earlier than the

projectile back release wave. The material at $4mm$ (specimen back surface) is loaded for $0\,\mu s$ because the pressure is simultaneously released by the free surface once the material is loaded. The effect of shock pulse duration on the deformation twins was first explored by Applenton and Waddington [79]. A study of austentic steel behaviour under different pulse duration shows that there is a significant difference in twin density for different shock loading durations at $10\,GPa$. Numerous twins were found at a pulse duration of $2\,\mu s$ but no twinning was present at $0.065\,\mu s$. Staudhammer and Murr [80] investigated the effect of shock wave duration on the microstructure of A1S1 304 stainless steel. They found that the twinning density increases up to a shock wave duration of $2\,\mu s$. Beyond this the twinning density stays constant. Murr [81] found that the primary effect of longer pulse duration in shock is mainly allowing the dislocations to have time for movement, interaction and equilibrating, therefore increasing the amount of dislocation-assisted twinning nucleation and growth as originally described by Cohen and Weertman [82] [83].

The elastic precursor decay is a phenomenon whereby when a shock wave travels through a material, the Hugoniot elastic limit (HEL) will decrease with the travel distance of the shock wave front [17]. The calculation of the elastic precursor decay in tantalum was developed by Gillis [67], following the dynamic yielding theory of dislocations [84] [85]. The differential equation of the HEL can be written as:

$$\frac{d\sigma}{dx} = -2G\frac{\dot{\epsilon}^p}{c} \tag{6.5}$$

Here $\frac{d\sigma}{dx}$ is the differential form of the dynamic yield point (HEL). $G$ is the material shear strength, $\dot{\epsilon}^p$ is the material plastic deformation rate at yield and $c$ is

the longitudinal acoustic wave velocity. $\dot{\epsilon}^p$ is:

$$\dot{\epsilon}^p = \Phi b(\rho_0 + \alpha\epsilon^p)v^\star exp(-D^\star/\tau) \tag{6.6}$$

where $\Phi$ is an orientation factor. For a single crystal with different orientation, $\Phi$ is the sine of the angle between the Burgers vector and the loading direction [86]. $b$ is the Burgers vector. $\rho_0$ is the initial dislocation density in the material. $\alpha$ is the dislocation multiplication coefficient. $v^\star$ is the maximum dislocation velocity. $D^\star$ is the characteristic drag stress. $\tau$ is the maximum shear stress. The values of the parameters of the dislocation ($\alpha$, $D^\star$, $\tau$) are taken from the work on annealed tantalum by Hoge [87]. The elastic parameters ($E$, $G$, $c$) are calculated from the data measured on single crystal Ta by Hartley [88]. The calculated result of the HEL decay is shown in Figure 6.7.

It can be seen that the HELs of the wave in the three orientations all start from 6.1 $GPa$ at the sample front surface. This is because when the sample is impacted by the projectile, there is no time or space for the wave to travel at the shock interface. Therefore the material yields at the shock wave pressure [16] [67]. When the travelling distance of the shock wave front increases, the HELs of the three orientation single crystals all decrease rapidly over the first 0.5 $mm$. Then they reduce with distance more slowly. At the specimen back surface, the calculated HELs of the [001], [011] and [111] samples are 2.47 $GPa$, 3.25 $GPa$ and 3.64 $GPa$, respectively. These are quite different from the HELs measured experimentally using HetV (3.37$GPa$, 2.23$GPa$, 3.08$GPa$ for [001], [011] and [111] specimen). However, it should be noted that Gillis's model for the elastic precursor decay does not consider

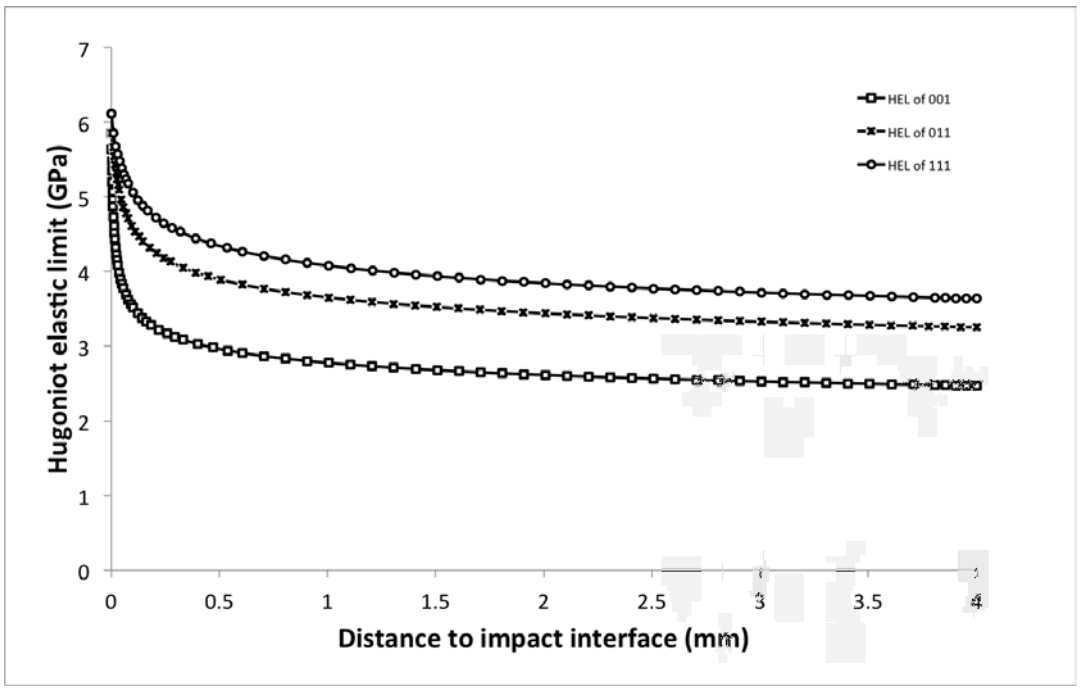


Figure 6.7: The calculation of the elastic precursor decay of tantalum single crystals under a 6.1 $GPa$ shock loading

the twinning as a deformation mechanism. This could change the characteristic drag stress of the material ($D^\star$) in total. Therefore it would be convenient to add a factor to $D^\star$ to adjust the value of the HEL to the experimental measurement. Thus the revised $D^\star$ can be written as:

$$D_r^\star = k\, D^\star \tag{6.7}$$

where $k$ is a correction factor related to the effect of twinning on the HEL. It is found that the drag factor for [001], [011] and [111] samples is 1.32, 0.67 and 0.85, respectively. The Hugoniot elastic limits of the single crystal specimens are

plotted in Figure 6.8 as a function of the distance to the shock impact interface. The profile of the area fraction of the twinning in the area (2) of every sample is also plotted in the same figure, against distance. The bottom figure shows the shock loading duration as a function of distance. It should be noted that in the twinning area fraction plot, the data in the range $0.5\,mm$ to $1.5\,mm$ is not used; because the image contrast is strongly influenced by the voids, the twinning cannot be identified.

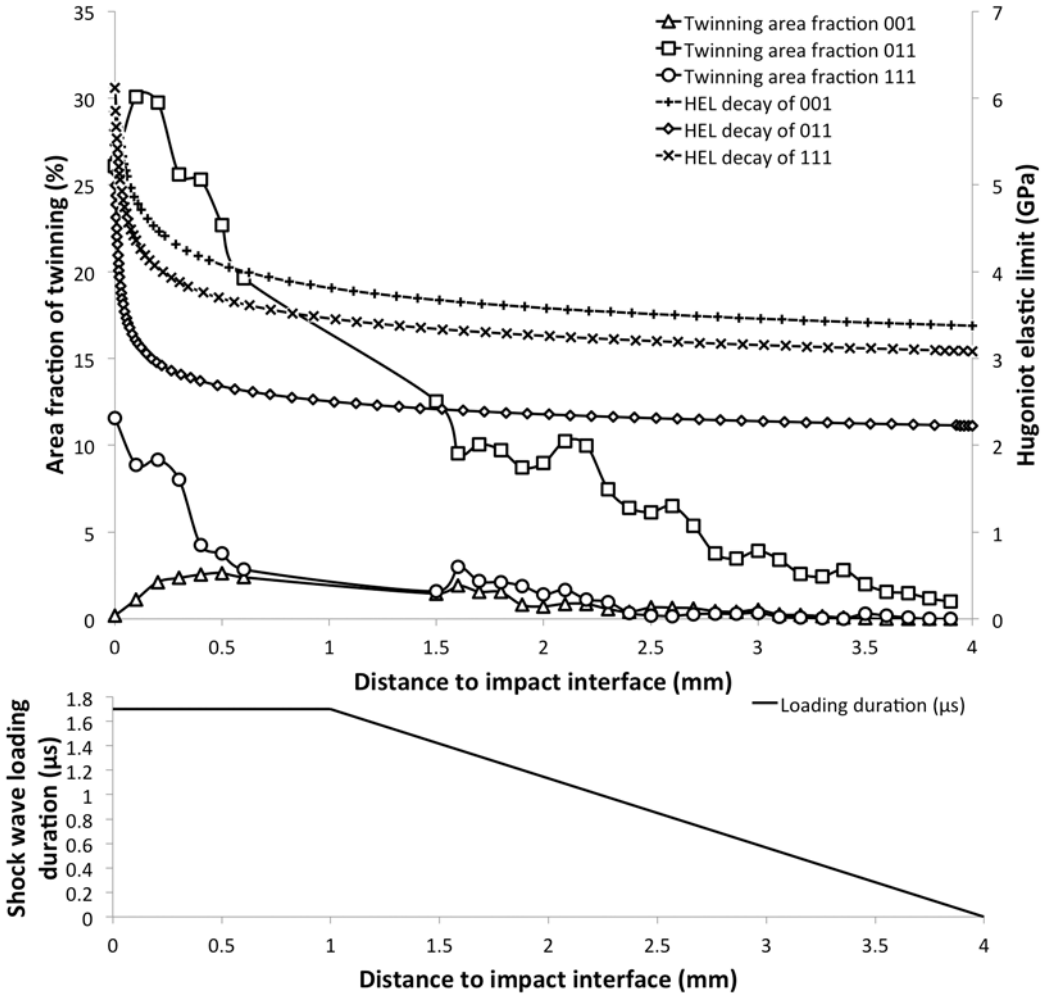


Figure 6.8: The relationship between the reformulated elastic precursor decay, twinning area fraction and the shock loading duration of the tantalum single crystals

The twinning area fraction in the [011] sample is generally higher than in the other two. This can be explained by the molecular dynamic study performed by Ravelo [68], showing that the twinning is more pronounced in shock along the [011]

direction compared to [001] and [111]. This is also reported by Florando [26]. The twinning area fraction decrease rapidly from the shock impact interface for $0.5mm$ in the [011] and [111] samples. This is probably due to the strong decay of the elastic precursor in this area. When the Hugoniot elastic limit decreases, the flow stress of the dislocations is reduced and the material slips more easily than twins. Therefore fewer twins are produced in the region with lower HEL. In the range from $1.5\,mm$ to $4\,mm$, even though the reduction in the HEL is small, the twinning area fraction in the [011] sample still decreases quickly. This is due to the effect of the reduction of the loading duration.

The twinning in the [001] sample shows a very different distribution. The area fraction at the shock interface is close to zero. It slowly increases to around 2.5% at $0.5\,mm$ and then decreases with distance. No theory seems able to explain this phenomenon. The very low density of twinning in the shock impact interface indicates that the shock front does not find it easy to create twins in the [001] sample. The peak of the twinning area fraction at $0.5\,mm$ shows that there is a concentration of twinning nucleation/growth at this depth. However, over the time period of the first compression loading cycle ($0 - 2.1\,\mu s$ in Figure 6.2), there is no difference in loading between $x = 0\,mm$ and $x = 0.5\,mm$, except via the reduction of the HEL.

To summarise the discussion of the twinning in the [001] specimen: (1) The reduction in the HEL can only allow the material to slip more and twin less. That the twinning area fraction rise from $0mm$ to $0.5mm$ in the [001] sample is not related to the elastic precursor decay. (2) The resolved shear stress analysis in section 6.5.1

shows that the twinning can only be produced by the shock wave front, not by the back release wave. (3) When we refer back to the void morphology, unlike in the other two specimens, the voids in the [001] sample do not nucleate/grow along the twinning direction. One possibility is that the twinning in this sample is produced after the voids. However, the compression wave after the first shock wave cycle is not as strong as the shock wave front. It should not be as powerful as the shock front in the creation of deformation twinning. The other possibility is that the twinning is created at the shock front. But because there are too many twinning systems activated at the same time (8 different planes), they cannot grow too much in length over the first compression cycle (before the void nucleation). Therefore the void clusters cannot grow in a specific orientation (as they do in [011] and [111]). This can also explain why the spall strength of the [001] sample is stronger than for the other two specimens, because voids have fewer sites (twin boundaries) to nucleate on and fewer voids lead to a higher spall strength. After the creation of the voids, the twins may grow again under the combined effect of the back release wave and the lateral release wave. From the simulation pressure/shear map in Figure 6.3 and Figure 6.4 it can be seen that the region close to the impact interface has never been highly shear stressed during the time of the first few wave propagation cycles. Therefore it would be reasonable to conclude that the peak in the twinning area fraction at a depth of $0.5\,mm$ in the [001] sample is caused by the twinning growth driven by the shear stress from the lateral release wave.

## 6.6 Dislocations

### 6.6.1 Stability of dislocation microstructure

As discussed in sections 6.2 and 6.3, the single crystal samples are not ′purely′ loaded by the shock wave front. After the shock wave passes, the specimen experiences the lateral/back release wave and the subsequent reflections. These waves can deform the material plastically. Compared with twinning, dislocation structures are much easier to move and can be changed by these waves. Therefore it is not known that whether the dislocation structure observed in the TEM/ECCI is produced mainly by the shock wave front, or is changed subsequently by the lateral/back release waves.

The stability of the dislocation structure generated in shock loading has been reviewed by Meyers [13]. He suggested that the loose dislocation cell structure often created by the shock compression is not stable: it usually collapses into better defined dislocation cells after the loading. The repeat loading experiment on nickel performed by Murr [81] shows that the repeated shock loading causes more twinning and dislocations in nickel and steel. Although the plastic deformation by the release wave and the tension waves (in the current experiment) have much lower strain rate than the shock front, they still experience similar amplitude. In the simulation result in Figure 6.3, the region being tensile stressed has $-5.4\,GPa$ pressure. The reloading in Figure 6.4-G have a pressure of $3.9\,GPa$. These stresses may strongly alter the dislocation substructure in the specimen.

The operating slip systems inside the material can also be influenced by the back/lateral release waves, or the waves produced from their interaction. A TEM

study on aluminium by Gray [89] shows that the dislocations produced by a series of repeated shock waves all operate on the same $\{111\}$ planes. This is because the orientation of the stress and strain for all the waves is the same, the deformation by the repeated shock waves can be accomplished using the previously activated slip resulting from the previous shock. The back release waves or the tensile/re-compression waves in the current experiment have the same loading direction as the shock compression wave. Therefore they will not change the slip systems activated by the unaxial strain at the shock wave front. However, the lateral release waves can induce shear loading that requires different slip systems used by the shock wave front. The residual dislocation substructure may be affected by them.

### 6.6.2 Dislocation morphology

The dislocation morphology in the three single crystals depends markedly on position. In the area close to the centre, the dislocations are loosely tangled with long straight screw dislocations, and curly dislocation loops/debris in between. A TEM study on $7 - 20\,GPa$ loaded polycrystalline tantalum reported by Gray [36] shows a very similar dislocation substructure. His TEM micrographs are shown in Figure 2.16. The loose dislocation tangle in area (5) of the three single crystals in the current study has the same characteristics as the $20\,GPa$ tantalum shocked by Gray. The density of the tangle and the dislocations in current study is higher than Gray's $7\,GPa$ shocked sample. Because Gray's specimen is protected by the momentum rings/disks, they are free from the influence of the release waves. Therefore the higher dislocation/tangle density in area (5) of the $6.13\,GPa$ shocked single crystals

of this research is induced by the lateral/back release waves.

The elongated dislocation cells (parallel walls) in area (4) of the single crystal specimens shows further microstructural development as compared with area (5). In qusi-static deformation, the dislocation cells (walls) often develop from the dislocation tangles, as shown in Figure 2.1. In the shock deformation of tantalum, dislocation walls are only found at much higher pressure. As shown in Table 2.2, only in $35\,GPa$ laser shock experiments, and $45\,GPa$ plate impact on single crystal tantalum are dislocation walls observed. In high stacking fault energy materials, such as Al, Ni, Fe, etc, the formation of dislocation walls is usually a sign of shear localisation and they will develop into geometrically necessary boundaries (GNBs) when the strain is high enough [90] [91] [92] [93]. The orientation of the dislocation walls is reported to be parallel to the $< 011 >$, $< 112 >$ and $< 123 >$ crystallographic directions after deformation in tension [94]. In cold rolled tantalum, the dislocation walls were observed to form on the highly activated slip planes 011 [93].

In the current study the dislocation walls are formed by the lateral release waves, after the shock wave front passes. Since the dislocation substructure in area (5) is strongly influenced by the shock wave front (the lateral stress is weak here), the dislocation cells/walls in area (4) can be seen as having developed from a earlier stage of the substructure in area (5): less dislocation tangles, just like the micrograph shown in Figure 2.16 ($7\,GPa$ 1-D shocked, without lateral release). The dislocation tangles of area (4), shown in Figure 5.23, 5.26 and 5.29, have no preferred orientation. Therefore the orientations of the dislocation walls at the edge of the samples are introduced by the lateral release waves.

Looking at the slip systems operating in area (4), the [111] specimen have all four Burgers vectors presented and the dislocation density does not showing significant change when different reflection conditions are employed, which means that all four slip systems are equally activated. Therefore the Burgers vector analysis in this specimen cannot be used to suggest a primary slip system. The dislocation walls in the [111] sample are found to be parallel to the [121], [111] and [101] directions, suggesting that due to the complex loading conditions in the non-protected shock loading, several different slip systems are operating to form the dislocation cells/walls.

Slip systems operating in the area (4) of the [011] and [001] samples seem unable to form a dislocation wall which is parallel to the shock loading direction and appear as thin and straight in the TEM image in the current observation. For instance, in the [011] specimen, the observed dislocations have Burgers vector $\frac{1}{2}[\bar{1}11]$ or $\frac{1}{2}[111]$. The only possible common slip plane for them is $(01\bar{1})$. However, the $(01\bar{1})$ plane is the TEM foil section plane. If the dislocation wall were parallel to $(01\bar{1})$, it would not appear as a straight line in the TEM. Loretto [95] has suggested that these dislocation walls may be caused by the interaction of two slip systems. When the $[\bar{1}11]$ and [111] dislocations are equally activated on the (101) and $(\bar{1}10)$ planes, they will meet at the (100) plane which is parallel to the shock loading direction [011]. The dislocation walls observed in the [001] specimen can also be explained via this mechanism. It would be helpful to use focused ion beam (FIB) to prepare a series of TEM specimens from the specimen centre to the edge, to observe the microstructure evolution from area (4) to area (5), and analyse the influence of the lateral release

wave amplitude on the dislocation wall formation. However, the high density of the tantalum makes the ion beam milling rather difficult. In the current study there are no effective tools that can remove the amorphous layer created by the ion beam on the surface of the FIB cut foil. Several attempts have been done using low energy ion beam and plasma, but the results were unsatisfactory.

### 6.6.3 Slip systems

As discussed in section 2.3, previous studies of dislocation slip in shock loaded material indicate that the dislocations produced behind the shock wave front resolve the stress/pressure at the wave front from 1-D to 3-D [22] [24]. The dislocation network behind the shock wave front proposed by Meyers [24] obeys the CRSS law. Therefore presumably the dislocations produced by the shock wave front follow the law that the slip systems (slip direction, slip plane) which have the highest Schmid factor are produced. Therefore, if the three single crystals are 1-dimensionally shock loaded (without any disturbance from lateral release waves), the dislocation Burgers vector left inside the specimen should be:

- [001] sample: [111], [$\bar{1}$11], [1$\bar{1}$1], [11$\bar{1}$]
- [011] sample: [111], [$\bar{1}$11]
- [111] sample: [$\bar{1}$11], [1$\bar{1}$1], [11$\bar{1}$]

Comparing with the results from TEM Burgers vector analysis in Table 5.2, it is found that except for the area (5) of the [011] sample, the Burgers vectors are

all different from the predictions of the model. In this case, the slip in the material is influenced by the combination of the back release wave and the lateral release wave. Their interaction makes the stress in the specimen complicated to analyse. To investigate the effect of the lateral release wave and back release wave on the slip behaviour, it would be helpful to do another set of shock loading experiments on the same tantalum single crystals (1) either with a spall plate to prevent the influence of the back release wave, hence the slip will only affected by the lateral release waves; or (2) with a momentum trap to prevent the influence of the lateral release wave, only allowing the back release wave to enter the material, to study the effect of pure back release wave. Then finally, with both spall plates and momentum trap to investigate the dislocation behaviour purely under 1-dimensional shock loading.

### 6.6.4 Dislocation density

Although the dislocation substructure is changed by the release waves, the dislocation density measured using ECCI still decreases from the sample front surface to the back surface. Usually in plastic deformation, the material experiencing more plastic strain/stress will have a higher dislocation density, because the plastic strain is accomplished by dislocation multiplication and movement [66]. If the dislocation movement velocity is the same (under the same pressure/stress), the plastic strain of the material depends on dislocation multiplication. For example, cold worked tantalum with 50% reduction has a much higher dislocation density than a sample with 20% reduction [93]. Repeated shock wave loading introduces more dislocations and results in a smaller dislocation cell size in tantalum [81]. In the tantalum single

crystals of the current study, the dislocation density at the impact surface is higher than it is at the back surface. Referring to the simulation results in section 6.3, in the shock impact phenomenon, the area close to the shock front surface is always being high pressure compressed/tensioned. The pressure in the region close to the back surface is usually lower. This is because this region is close to a free surface, i.e. no stress is applied. Therefore the total strain/stress at the sample front surface is generally higher than at the back and the dislocation density is higher.

The dislocation density rises at the edge of the sample front surface is due to the lateral plastic strain caused by the lateral release wave. Figure 2.7 shows that the lateral release wave induces lateral movement of material. This means that the specimen will strain in the radial direction when released by the lateral release wave. This phenomenon can be seen in the simulation in Figure 6.3. When the shock wave is just entering the material at time $0.2\,\mu s$, the lateral surfaces of the specimen and the projectile are perfectly parallel. When the lateral release waves keep moving into the sample, the material of both sample and projectile close to the shock interface starts to pop out. This lateral strain then stops and this specimen keeps its shape until the finish of the simulation. The material at the back surface is also loaded by the lateral release wave, but did not see a lot of lateral strain. This is because the shock wave reflects at the sample back surface and transfers to a back release wave, which interacts with the lateral one and cancels the radial velocity. The material at the back surface moves mainly along the shock wave direction, therefore has a lower lateral strain than the front surface. This strain can be seen in the filtered twinning image in Figure 5.18 where the upper right corner has popped out for around $0.2mm$.

This extra strain is the reason why the dislocation density is particularly high at the edge of the shock loading interface.

## 6.7 Electron channelling contrast image

The calculations suggest that dislocations in tantalum should indeed be visible using the backscattered electron signal. The background change with the deviation parameter $w$ is essentially due to the change of the backscattering coefficient $p'$. The background intensity is $I_B(0)$ without the term related to the sum of the Bloch waves, i.e. $\frac{p't}{1+p't}$ [48]. The backscattering coefficients $p'$ is a function of the Fourier coefficient $C_g^{(i)}$ and hence is related to the deviation parameter $w$. From the electron-material interaction point of view, for an incident direction close to the Bragg condition, the electron wave $\psi^{(1)}$ is close to the 'channel' between the crystal planes and therefore it is backscattered less. It can be seen from Figure 3.1 that the BSE intensity is lower at the Bragg condition compared with $w > 0$, when neither of the Bloch waves is channelled. The width of the dislocation image is around 2 times the extinction distance, which is in good agreement with previous simulation results [48] [57] [58]. The 'oscillatory' shape of the profile comes from the $\underline{g} \cdot \underline{R}$ component. When the sample column is on either side of the dislocation the $\underline{g} \cdot \underline{R}$ component will have a different sign. This will give a positive/negative gain to the Bloch wave intensity and hence have a different influence on the backscattered electron intensity.

The dislocation depth has a strong effect on the image contrast. The contrast falls exponentially with dislocation depth. In addition to this exponential attenua-

tion, the contrast will also oscillate with depth, with a periodicity of $\xi_g$ [48]. (This phenomenon can also be found in the dislocation profiles in Figure 5.33). The contrast of the dislocation ($I_{max} - I_{min}$) is reduced as the depth of the dislocation in the material increases. In Equation 3.5, the contrast of the dislocation in the ECCI comes from the sum of the integration of the Bloch waves intensities with depth. The Bloch waves attenuate quickly with crystal depth due to absorption. When the dislocation is close to the surface, the Bloch waves are still strong as they are altered by the strain field of the dislocation core, hence altering significantly the backscattered electron intensity. When the dislocation is deep inside the crystal, the Bloch waves are influenced by the dislocation core when they are weak and thus barely change the total $\int I_j dz$ term. Therefore the dislocation contrast is much smaller than when the dislocation is close to the surface. The dislocation image disappears totally at a dislocation depth of $10\xi_g$, because the Bloch waves are very close to 0 at this depth and cannot contribute to the backscattered electron contrast.

The ECCIs of the dislocations were taken in an SEM with a normal configuration (low angle tilt). The same area was re-examined by TEM and compared with ECCI. At first glance, the dislocation micrographs from ECCI look completely different from the TEM bright field images. The dislocations in ECCI are not as dense or clear. However, those dislocations which do appear in ECCI show good agreement with the bright-field images. Some dislocations may be missing because their depth is greater than the imaging depth of the backscattered electrons. The simulation shown in Figure 5.33 indicates that the contrast of the defect gradually decreases with dislocation depth and disappears totally before a depth of $10\xi_g$. In

this case - tantalum with a (211) reflection and a $30kV$ electron beam - the extinction distance is $21nm$ (i.e. $10\xi_g = 210nm$). The effective limiting imaging depth of the dislocations in this experiment is $120nm$. In practical observation, the imaging depth can be influenced by the surface condition of the specimen, the condition of the detector and the signal noise. On the right side of the dislocation channelling contrast image (in Figure 5.35b) the contrast is much weaker than on the left side, which is close to the sample surface. This shows strong evidence that the contrast decreases with the depth of the dislocation.

Unlike the simulated profile, the dislocation profile in ECCI seems to be only a peak on a dark background, without the $'$valley$'$ part (labelled $B$ in Figure 5.32). This again is probably due to the noise in the BSE image. From Figure 5.32 it can be seen that at the minimum point of the dislocation profile at the Bragg condition, the BSE intensity is almost zero and could therefore easily be dominated by the noise from the environment. Another example of a dislocation channelling contrast image shown in Figure 6.9, with a higher deviation parameter, provides evidence for the $'$valley$'$, which is here probably not totally dominated by the background noise because of the higher background BSE intensity. This behaviour is very common in ECCI [56] [62]. For example, in an ECCI study of dislocations in Si, for an image with dark background ($w \approx 0$), the dislocation appears only as a simple bright line. On the dislocation images with brighter background ($w > 0$), the dislocation image is brighter on one side and darker on the other [62].

A previous study by Ahmed and Simkin suggested that the dislocation contrast is optimised at the Bragg condition. The influence of the deviation parameter $w$ on

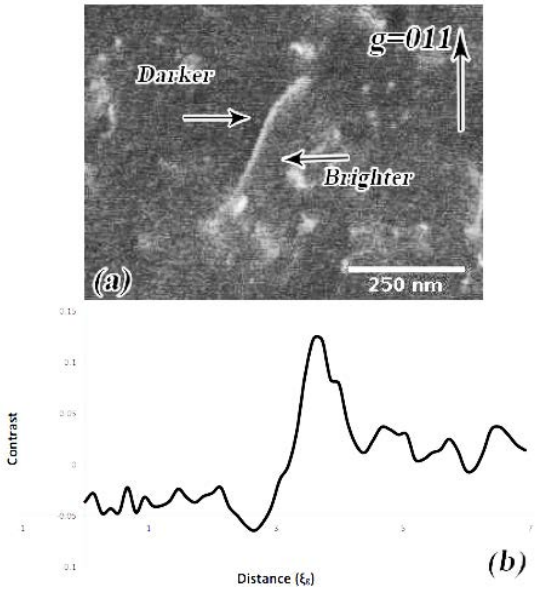


Figure 6.9: An example of dislocation image contrast in ECCI (captured from tantalum single crystal with loading direction [011]). (a) dislocation micrograph; (b) intensity profile across dislocation

the contrast profile is shown in Figure 5.32. The total range of acceptable contrast is around 0.5°. This angle corresponds to quite a large deviation parameter ($w \approx 10$). Theoretically the dislocation should not show any contrast in ECCI since in the simulation, the contrast decreases rapidly when $w$ is higher than 1. But even when the electron beam is tilted 0.5° away from the Bragg condition, part of the beam in the range will still stay close to the Bragg condition and give rise to the dislocation contrast. This is probably the reason why the imaging range for the dislocations in ECCI appears larger than the theoretical value.

The dislocation density measured by ECCI is accurate when compared with the TEM measurement. In the preparation of the TEM foil, dislocations can escape out of the specimen from the thin area. These ′escapes′ would certainly reduce the dislocation density measured by TEM, but are less likely in the ECCI measurement, because the strain is more difficult to release from a bulk sample than from a thin foil.

As an example, a dislocation density measurement was made on a shocked tantalum single crystals. The example of the density profile for a tantalum [011] single crystal shown in Figure 5.43 indicates that the average dislocation density is higher close to the shock interface and becomes lower away from the interface. The dislocation densities at the sample edge are always higher than those in the central region, except for the region close to the sample front surface. Because the release wave from the back surface moves more quickly than the shock wave front, the shock duration at the back surface is shorter than at the front surface (shock interface). The strain rate of the back release wave is also lower at the back surface. This

is probably the reason why the dislocation density at the front surface is higher than at the back. The tantalum single crystal was mounted in epoxy. After the shock wave front passed, the release wave would enter the material from the edge of the sample front surface. The obliquity of the lateral release wave will introduce a high shear stress/strain into the single crystal. This high shear stress/strain would produce more dislocations in the material and with the attenuation of the lateral release wave the dislocation density is lower at the sample centre.

# Chapter 7

# Conclusion

## 7.1 Shock induced defects

The plate impact shock experiment used here generated a $6.1 GPa$ shock wave front. The material experienced loading from shock wave, lateral release wave, back release wave and their interactions/reflections.

The shock wave front created profuse deformation twinning and dislocations in the three single crystals. The spatial distribution of the defects were characterised using SEM and TEM.

In the [011] and [111] samples, twinning acts as a major deformation mechanism at the shock wave front. In the [001] sample, twinning is nucleated at the shock wave front but grows with the influence of the wave-wave interaction stresses.

The area fraction of twinning decreases with the travelling distance of the shock wave front. The deformation twinning influenced the HEL of the material. The

HetV measured HEL for the [001], [011] and [111] samples was 3.17 $GPa$, 2.23 $GPa$ and 3.08 $GPa$. The calculated dislocation flow drag factor shows that the effect of deformation twinning on the [001] sample is hardening, but softening on the other two.

The twinning produced in area (2) of all the three samples followed the CRSS law. However, in area (3) their behaviour is rather complex under the combination of back and lateral release waves. The interaction of the back release waves created voids in the tantalum single crystals. The voids in sample [111] and [011] nucleate and grow along the twinning boundaries. In the [001] sample, fewer voids are created due to lack of pre-existing nucleation sites (twinning) created by the shock wave front. This gives the [001] sample a higher spall strength than the [011] and [111] specimens.

The dislocation structure, density and slip systems are heavily influenced by wave reflection and interaction. ECCI dislocation density measurements show that more dislocations are created by the back release wave interaction in the region close to the shock interface and that the lateral release wave induced extra lateral strain.

## 7.2 Electron channelling contrast image

The contrast profile of a dislocation in an electron channelling contrast image has been calculated. The results indicate that in an SEM with an untilted sample, dislocations in a tantalum specimen should be visible in the backscattered electron image near the Bragg condition. Experiments on tantalum in an SEM confirm

the visibility of dislocations in ECCI. The effects of the deviation parameter $w$ and dislocation depth have been studied both by simulation and experiment. The results show that the best imaging condition is achieved when the crystal is at the exact Bragg condition. However, due to the convergence angle of the electron beam in the SEM, a relatively large range of beam directions (0.5°) is allowed in practical imaging. The imaging depth of the ECCI is calculated to be less than $10\xi_g$. This was then verified experimentally to be around $5\xi_g$ in practice due to the extra noise introduced by the environment. In practical measurements of the dislocation density, $5\xi_g$ should be used as the effective imaging depth of ECCI. The method for measuring the dislocation density using ECCI can then be summarised to be: use a small working distance to maximise the collection angle of backscattered electrons, use the exact Bragg condition to optimise the dislocation contrast and use an imaging depth of $5\xi_g$ as the $'$sample thickness$'$ to calculate the dislocation density. This methodology has been applied to the shocked tantalum single crystals. The dislocation density results well represent the loading experienced by the specimen.

# Chapter 8

# Future work

There are several issues that have yet to be resolved in this study. (1) The origin of the deformation twinning in the area (4) of the single crystals is still not clear, due to the complex loading stress produced by the interaction of the back and lateral release waves. (2) The dislocation substructure evolution from the dislocation tangle to the parallel dislocation walls needs a better understanding. (3) The interaction of the lateral and back release wave has a significant effect on the microstructure of the tantalum single crystals. It would be helpful to see the influence of the lateral or back release wave alone, on the defect evolution of the tantalum single crystals.

For the origin of the deformation twinning at the edge of the specimen, the difficult issue is that the stress produced by the waves in area (4) of the specimen is complicated. It cannot be solved with pencil and paper. Hydrocode simulation should be used in the future to analyse the shear stress and strain on every twinning plane to decide if the twins are the most stressed system, and how much stress is

applied on each system.

The dislocation substructure changes from loose tangle in the specimen centre to parallel dislocation walls at the edge should be studied to see how the effect of the lateral release wave decreases with the travelling distance. To achieve this, a series of TEM foils could be made from the edge of the specimen to the centre using focused ion beam. Then the evolution of the dislocation wall structure can be observed using a TEM.

Since the conventional method to prevent lateral and back release waves are momentum rings and spall plates, these two waves can be easily divided into two experiments, to study their effects separately. To investigate the effect of the back release wave, the material needs to be mounted into a fixture with only momentum rings; to study the effect of the lateral release wave, the material should be mounted in epoxy with spall plates fixed at the back surface. After these study, a much better understanding of tantalum behaviour under complex loading conditions will be achieved.

# References


[1] A. L. Stevens and O. E. Jones. Radial Stress Release Phenomena in Plate Impact Experiments: Compression-Release. *Journal of Applied Mechanics*, 39(2):359–366, 1972.

[2] S. M. Cardonne, P. Kumar, C. A. Michaluk, and H. D. Schwartz. Tantalum and Its Alloys. *International Journal of Refractory Metals and Hard Materials*, 13(4):187–194, 1995.

[3] V. F. Nesterenko, M. A. Meyers, J. C. LaSalvia, M. P. Bondar, Y. J. Chen, and Y. L. Lukyanov. Shear Localization and Recrystallization in High-Strain, High-Strain-Rate Deformation of Tantalum. *Materials Science and Engineering: A*, 229(1-2):23–41, 1997.

[4] T. E. Mitchell and W. A. Spitzig. Three-Stage Hardening in Tantalum Single Crystals. *Acta Metallurgica*, 13(11):1169–1179, 1965.

[5] J. F. Byron. Plastic Deformation of Tantalum Single Crystals. *Journal of the Less Common Metals*, 14(2):201–210, 1968.

[6] S. Takeughi, E. Kuramoto, and T. Suzuki. Orientation Dependence of Slip in Tantalum Single Crystals. *Acta Metallurgica*, 20(7):909–915, 1972.

[7] J. A. Shields, S. H. Goods, R. Gibala, and T. E. Mitchell. Deformation of High Purity Tantalum Single Crystals at 4.2 K. *Materials Science and Engineering*, 20:71–81, 1975.

[8] W. A. Spitzig and T. E. Mitchell. Dislocation Arrangements in Tantalum Single Crystals Deformed in Tension at 373 K. *Acta metallurgica*, 14(10):1311, 1966.

[9] W. J. M. Rankine. On the Thermodynamic Theory of Waves of Finite Longitudinal Disturbance. *Philosophical Transactions of the Royal Society of London*, 160:277–288, 1870.

[10] D. Grady. Shock Equation of State Properties of Concrete. *International conference on structures under shock and impact*, 1:1–9, 1996.

[11] M. H. Rice, R. G. McQueen, and J. M. Walsh. Compression of Solids by Strong Shock Waves. *Solid State Physics - Advances in Research and Applications*, 6(C):1–63, 1958.

[12] J. M. Walsh and R. H. Christian. Equation of State of Metals from Shock Wave Measurements. *Physical Review*, 97(6):1544–1556, 1955.

[13] M. A. Meyers and H. Jarmakani. Dislocations in Shock Compression and Release. *Dislocations in Solids*, 15(09):91–197, 2009.

[14] J. C. F. Millett, N. K. Bourne, G. T. Gray, and I. P. Jones. The Response of TiAl Based Alloys to One-Dimensional Shock Loading. *Acta Materialia*, 50(19):4801–4811, 2002.

[15] F. Cao, I. J. Beyerlein, F. L. Addessio, B. H. Sencer, C. P. Trujillo, E. K. Cerreta, and G. T. Gray. Orientation Dependence of Shock-induced Twinning and Substructures in a Copper Bicrystal. *Acta Materialia*, 58(2):549–559, 2010.

[16] M. A. Meyers, editor. *Dynamic Behavior of Materials*. John Wiley & Sons, Inc., Hoboken, NJ, USA., 1994.

[17] J. R. Asay and M. Shahinpoor, editors. *High-Pressure Shock Compression of Solids*. Springer, New York, USA., 1993.

[18] G. T. Gray, L. M. Hull, J. R. Faulkner, M. E. Briggs, E. K. Cerreta, F. L. Addessio, and N. K. Bourne. The Effects of Shockwave Profile Shape and Shock Obliquity on Spallation: Kinetic and Stress-State Effects on Damage Evolution. *AIP Conference Proceedings*, 1195:1097–1102, 2009.

[19] G. T. Gray, N. K. Bourne, and J. C. F. Millett. Shock Response of Tantalum: Lateral Stress and Shear Strength Through the Front. *Journal of Applied Physics*, 94(10):6430–6436, 2003.

[20] J. O. Erkman. Explosively Induced Nonuniform Oblique Shocks. *Physics of Fluids*, 1(6):535, 1958.

[21] G. T. Gray, P. S. Follansbee, and C. E. Frantz. Effect of Residual Strain on the

Substructure Development and Mechanical Response of Shock-Loaded Copper. *Materials Science and Engineering: A*, 111:9–16, 1989.

[22] C. S. Smith. Metallographic Studies of Metals after Explosive Shock. *Trans. Met. Soc. A.I.M.E.*, 212:574–585, 1958.

[23] E. Hornbogen. Shock-Induced Dislocations. *Acta Metallurgica*, 10(10):978–980, 1962.

[24] M. A. Meyers. A Mechanism for Dislocation Generation in Shock-Wave Deformation. *Scripta Metallurgica*, 12(1):21–26, 1978.

[25] R. E. Rudd, A. J. Comley, J. Hawreliak, B. R. Maddox, H. S. Park, and B. A. Remington. Theory and Simulation of 1D TO 3D Plastic Relaxation in Tantalum. *AIP Conference Proceedings*, 1426:1379–1382, 2012.

[26] J. N. Florando and N. R. Barton. Analysis of Deformation Twinning in Tantalum Single Crystals Under Shock Loading Conditions. *Journal of Applied Physics*, 083522:1–8, 2013.

[27] L. E. Murr, M. A. Meyers, C. S. Niou, Y. J. Chen, S. Pappu, and C. Kennedy. Shock-Induced Deformation Twinning in Tantalum. *Acta Materialia*, 45(1):157–175, 1997.

[28] C. H. Lu, B. A. Remington, B. R. Maddox, B. Kad, H. S. Park, M. Kawasaki, T. G. Langdon, and M. A. Meyers. Laser Compression of Nanocrystalline Tantalum. *Acta Materialia*, 61(20):7767–7780, 2013.

[29] L. M. Hsiung and D. H. Lassila. Shock-Induced Deformation Twinning and Omega Transformation in Tantalum and Tantalum–Tungsten Alloys. *Acta Materialia*, 48(20):4851–4865, 2000.

[30] L. M. Hsiung and D. H. Lassila. Shock-Induced Omega Phase in Tantalum. *Scripta Materialia*, 38(9):1371–1376, 1998.

[31] S. V. Razorenov, G. Garkushin, G. I. Kanel, and O. N. Ignatova. The Spall Strength and Hugoniot Elastic Limit of Tantalum with Various Grain Size. *AIP Conference Proceedings*, 1426:991–994, 2012.

[32] M. A. Meyers, O. Vöhringer, and V. A. Lubarda. The Onset of Twinning in Metals: A Constitutive Description. *Acta Materialia*, 49(19):4025–4039, 2001.

[33] M. D. Furnish, L. C. Chhabildas, and D. J. Steinberg. Dynamical Behavior of Tantalum. *AIP Conference Proceedings*, 309:1099–1102, 1994.

[34] M. D. Furnish, D. H. Lassila, L. C. Chhabildas, and D. J. Steinberg. Dynamic Material Properties of Refractory Metals: Tantalum and Tantalum/Tungsten Alloys. *AIP Conference Proceedings*, 370:527–530, 1996.

[35] Q. An, R. Ravelo, T. C. Germann, W. Z. Han, S. N. Luo, D. L. Tonks, and W. A. Goddard. Shock Compression and Spallation of Single Crystal Tantalum. *AIP Conference Proceedings*, 1426:1259–1262, 2012.

[36] George T. Gray and Kenneth S. Vecchio. Influence of Peak Pressure and Temperature on the Structure/Property Response of Shock-Loaded Ta and Ta-10W. *Metallurgical and Materials Transactions A*, 26(10):2555–2563, 1995.

[37] C. H. Lu, B. A. Remington, B. R. Maddox, B. Kad, H. S. Park, S. T. Prisbrey, and M. A. Meyers. Laser Compression of Monocrystalline Tantalum. *Acta Materialia*, 60(19):6601–6620, 2012.

[38] L. L Hsiung. Shock-induced phase transformation in tantalum. *Journal of physics: Condensed matter*, 22(38):385702, 2010.

[39] L. L Hsiung. On the Micromechanisms of Shock-Induced Martensitic Transformation in Tantalum. *AIP Conference Proceedings*, 845:228–231, 2006.

[40] V. Livescu, J. F. Bingert, and T. A. Mason. Deformation Twinning in Explosively-Driven Tantalum. *Materials Science and Engineering: A*, 556:155–163, 2012.

[41] G.T. (Rusty) Gray III, V. Livescu, E. K. Cerreta, T. A. Mason, P. J. Maudlin, and J. F. Bingert. Influence of Shockwave Obliquity on Deformation Twin Formation in Ta. *9th International Conferences on the Mechanical and Physical Behaviour of Materials under Dynamic Loading*, 2:963–969, 2009.

[42] D. E. Newbury, D. C. Joy, P. Echlin, C. E. Fiori, and J. I. Goldstein. *Electron Channeling Contrast in the SEM*. Springer US, 1986.

[43] F. L. Vogel, W. G. Pfann, H. E. Corey, and E. E. Thomas. Observations of Dislocations in Lineage Boundaries in Germanium. *Physical Review*, 90(3):489–490, 1953.

[44] J. W. Menter. The Direct Study by Electron Microscopy of Crystal Lattices

and their Imperfections. *Proceedings of the Royal Society of London A: Mathematical, Physical and Engineering Sciences*, 236(1204):119–135, 1956.

[45] A. Howie and M. J. Whelan. Diffraction Contrast of Electron Microscope Images of Crystal Lattice Defects. III. Results and Experimental Confirmation of the Dynamical Theory of Dislocation Image Contrast. *Proceedings of the Royal Society of London A: Mathematical, Physical and Engineering Sciences*, 267(1329):206–230, 1962.

[46] M .J. Whelan and P. B. Hirsch. Electron Diffraction from Crystals Containing Stacking Faults: I. *Philosophical Magazine*, 2(21):1121–1142, 1957.

[47] P. B. Hirsch, A. Howie, and M. J. Whelan. A Kinematical Theory of Diffraction Contrast of Electron Transmission Microscope Images of Dislocations and other Defects. *Philosophical Transactions of the Royal Society of London A: Mathematical, Physical and Engineering Sciences*, 252(1017):499–529, 1960.

[48] J. P. Spencer, C. J. Humphreys, and P. B. Hirsch. A Dynamical Theory for the Contrast of Perfect and Imperfect Crystals in the Scanning Electron Microscope Using Backscattered Electrons. *Philosophical Magazine*, 26(1):193–213, 1972.

[49] B. C. Ng, B. A. Simkin, and M. A. Crimp. Application of the Electron Channeling Contrast Imaging Technique to the Study of Dislocations Associated with Cracks in Bulk Specimens. *Ultramicroscopy*, 75(3):137–145, 1998.

[50] H. Mansour, J. Guyon, M. A. Crimp, N. Gey, B. Beausir, and N. Maloufi. Ac-

curate Electron Channeling Contrast Analysis of Dislocations in Fine Grained Bulk Materials. *Scripta Materialia*, 84-85:11–14, 2014.

[51] Y. N. Picard, M. E. Twigg, J. D. Caldwell, C. R. Eddy, M. A. Mastro, and R. T. Holm. Resolving the Burgers vector for individual GaN dislocations by electron channeling contrast imaging. *Scripta Materialia*, 61(8):773–776, 2009.

[52] P. B. Hirsch, A. Howie, and M. J. Whelan. On the Production of X-Rays in Thin Metal Foils. *Philosophical Magazine*, 7(84):2095–2100, 1962.

[53] D. G. Coates. Kikuchi-Like Reflection Patterns Obtained with the Scanning Electron Microscope. *Philosophical Magazine*, 16(144):1179–1184, 1967.

[54] P. B. Hirsch and C. J. Humphreys. The Dynamical Theory of Scanning Electron Microscope Channelling Patterns. *Proceedings of Third Annual Scanning Electron Microscope Symposium, Chicago*, pages 449–455, 1970.

[55] P. Morin, M. Pitaval, D. Besnard, and G. Fontaine. Electron Channelling Imaging in Scanning Electron Microscopy. *Philosophical Magazine A*, 40(4):511–524, 1979.

[56] J. T. Czernuszka, N. J. Long, E. D. Boyes, and P. B. Hirsch. Imaging of Dislocations Using Backscattered Electrons in a Scanning Electron Microscope. *Philosophical Magazine Letters*, 62(4):227–232, 1990.

[57] A. J. Wilkinson, G. R. Anstis, J. T. Czernuszka, N. J. Long, and P. B. Hirsch. Electron Channelling Contrast Imaging of Interfacial Defects in Strained

Silicon-Germanium Layers on Silicon. *Philosophical Magazine A*, 68(1):59–80, 1993.

[58] A. J. Wilkinson and P. B. Hirsch. The Effects of Surface Stress Relaxation on Electron Channelling Contrast Images of Dislocations. *Philosophical Magazine A*, 72(1):81–103, 1995.

[59] M. A. Crimp, B. A. Simkin, and B. C. Ng. Demonstration of the g · b x u = 0 Edge Dislocation Invisibility Criterion for Electron Channelling Contrast Imaging. *Philosophical Magazine Letters*, 81(12):833–837, 2001.

[60] B. A. Simkin and M. A. Crimp. An Experimentally Convenient Configuration for Electron Channeling Contrast Imaging. *Ultramicroscopy*, 77:65–75, 1999.

[61] J. Ahmed, A. J. Wilkinson, and S. G. Roberts. Characterizing Dislocation Structures in Bulk Fatigued Copper Single Crystals Using Electron Channelling Contrast Imaging (ECCI). *Philosophical Magazine Letters*, 76(4):237–246, 1997.

[62] M. A. Crimp. Scanning Electron Microscopy Imaging of Dislocations in Bulk Materials, Using Electron Channeling Contrast. *Microscopy Research and Technique*, 69(5):374–381, 2006.

[63] I. Gutierrez-Urrutia and D. Raabe. Dislocation Density Measurement by Electron Channeling Contrast Imaging in a Scanning Electron Microscope. *Scripta Materialia*, 66(6):343–346, 2012.

[64] P. B. Hirsch, A. Howie, R. B. Nicholson, D. W. Pashley, M. J. Whelan, and

L. Marton. *Electron Microscopy of Thin Crystals*. Butterworths, London, UK., 1977.

[65] M H Loretto and R E Smallman. *Defect Analysis in Electron Microscopy*. Science paperbacks. Chapman and Hall, UK, 1975.

[66] D. Hull and D. J. Bacon. *Introduction to Dislocations*. Elsevier Science, USA., 2001.

[67] P. P. Gillis. Elastic Precursor Decay in Tantalum. *Journal of Applied Physics*, 42(5):2145, 1971.

[68] R. Ravelo, T. C. Germann, O. Guerrero, Q. An, and B. L. Holian. Shock-Induced Plasticity in Tantalum Single Crystals: Interatomic Potentials and Large-Scale Molecular-Dynamics Simulations. *Physical Review B*, 88(13):134101, 2013.

[69] D. L. Preston, D. L. Tonks, and D. C. Wallace. Model of Plastic Deformation for Extreme Loading Conditions. *Journal of Applied Physics*, 93(1):211–220, 2003.

[70] T. Antoun, L. Seaman, D. R. Curran, G. I. Kanel, S. V. Razorenov, and A. V. Utkin. *Spall Fracture*. Shock Wave and High Pressure Phenomena. Springer New York, 2006.

[71] F. A. McClintock, editor. *Ductility: Papers Presented at a Seminar of the American Society for Metals*. American Society for Metals, USA., 1968.

[72] P. F. Thomason. A Theory for Ductile Fracture by Internal Necking of Cavities. *Journal of the Institute of Metals*, 98:360–365, 1968.

[73] L. M. Brown and J. D. Embury. The Initiation and Growth of Voids at Second Phase Particles. *Proceedings 3rd International Conference on Strength of Metals and Alloys*, pages 571–582, 1973.

[74] Y. Tang, E. M. Bringa, B. A. Remington, and M. A. Meyers. Growth and Collapse of Nanovoids in Tantalum Monocrystals Loaded at High Strain Rate. *AIP Conference Proceedings*, 1426(4):1255–1258, 2012.

[75] V. A. Lubarda, M. S. Schneider, D. H. Kalantar, B. A. Remington, and M. A. Meyers. Void Growth by Dislocation Emission. *Acta Materialia*, 52(6):1397–1408, 2004.

[76] D. Rittel, M. L. Silva, B. Poon, and G. Ravichandran. Thermomechanical Behavior of Single Crystalline Tantalum in the Static and Dynamic Regime. *Mechanics of Materials*, 41(12):1323–1329, 2009.

[77] P. J. Sherwood, F. Guiu, H. C. Kim, and P. L. Pratt. Plastic Anisotropy of Tantalum, Nibium, and Molybdenum. *Canadian Journal of Physics*, 45(2):1075–1089, 1967.

[78] J. W. Christian and S. Mahajan. Deformation Twinning. *Progress in Materials Science*, 39:1–157, 1995.

[79] Appleton A. S. and J. S. Waddington. The Importance of Shock Wave Profile in Explosive Loading Experiments. *Acta Metallurgica*, 12(8):956–957, 1964.

[80] L. E. Murr and J. Y. Huang. Effect of Shock-Stress Duration on the Residual Structure and Hardness of Nickel, Chromel and Inconel. *Materials Science and Engineering*, 19(1):115–122, 1975.

[81] L. E. Murr. Effects of Peak Pressure, Pulse Duration, and Repeated Loading on the Residual Structure and Properties of Shock Deformed Metals and Alloys. *Shock Waves and High-Strain-Rate Phenomena in Metals*, 1:753–777, 1981.

[82] J. B. Cohen and J. Weertman. A Dislocation Model for Twinning in f.c.c. Metals. *Acta Metallurgica*, 11(8):996–998, 1963.

[83] A. H. Cottrell and B. A. Bilby. A Mechanism for the Growth of Deformation Twins in Crystals. *The London, Edinburgh, and Dublin Philosophical Magazine and Journal of Science*, 42(329):573–581, 1951.

[84] J.W. Taylor. Dislocation Dynamics and Dynamic Yielding. *Journal of Applied Physics*, 36(10):3146–3149, 1965.

[85] R. W. Rohde, editor. *Metallurgical Effects at High Strain Rates*. Springer US, 1973.

[86] P. Gillis and J. Gilman. Dynamical Dislocation Theory of Crystal Plasticity. I. The Yield Stress. *Journal of Applied Physics*, 36(11):3370–3380, 1965.

[87] K. G. Hoge and P. P. Gillis. The Rheological Properties of Annealed Tantalum. *Metallurgical Transactions*, 2(1):261–264, 1971.

[88] C. S. Hartley. Elasticity of Tantalum Single Crystals. *Journal of the Less Common Metals*, 6:245–248, 1964.

[89] G. T. Gray and J. C. Huang. Influence of Repeated Shock Loading on the Substructure Evolution of 99.99 wt.% Aluminum. *Materials Science and Engineering: A*, 145(1):21–35, 1991.

[90] M. Z. Quadir and B. J. Duggan. A Microstructural Study of the Origins of Gamma Recrystallization Textures in 75% Warm Rolled IF Steel. *Acta Materialia*, 54(16):4337–4350, 2006.

[91] Q. Z. Chen and B. J. Duggan. On Cells and Microbands Formed in an Interstitial-Free Steel During Cold Rolling at Low to Medium Reductions. *Metallurgical and Materials Transactions A*, 35(11):3423–3430, 2004.

[92] N. Hansen, X. Huang, and G. Winther. Grain Orientation, Deformation Microstructure and Flow Stress. *Materials Science and Engineering A*, 494(1-2):61–67, 2008.

[93] C. Chen, M. P. Wang, S. Wang, Y. L. Jia, R. S. Lei, F. Z. Xia, B. Zuo, and H. C. Yu. The Evolution of Cold-Rolled Deformation Microstructure of {001}[110] Grains in Ta–7.5wt%W Alloy Foils. *Journal of Alloys and Compounds*, 513:208–212, 2012.

[94] T. W. Barbee and R. A. Huggins. Dislocation structures in deformed and recovered tantalum. *Journal of the Less Common Metals*, 8(5):306–319, 1965.

[95] M. H. Loretto. Private Communication, 2015.